# Composition-tuned magnetic order and excitations in $Nb_{1-x}Fe_{2+x}$ and pressure-induced changes in structural and optical properties of $Cu_2OSeO_3$

**James Nicholas Poulten**

A thesis submitted to the

University of London

for the degree of Doctor of Philosophy


Department of Physics

Royal Holloway University of London

June 30, 2018

## Declaration of Authorship

I, James Nicholas Poulten, hereby declare that this thesis and the work presented in it, is entirely my own. Where I have consulted the work of others, I have clearly stated as such.

Sign: .....

Date: .....

# Abstract

Understanding the magnetic properties of matter is of paramount interest from a principal and technological point of view. For example, transition-metal compounds tuned to a magnetic quantum phase transition often form unconventional superconductivity and exhibit non-Fermi liquid behaviour. The discovery of novel magnetic states such as the skyrmion lattices might lead to new magnetic storage technologies if a full understanding of the magnetic, electronic, and structural material properties is obtained. This thesis presents results on composition and pressure-tuned magnetic compounds: the itinerant ferromagnet $Nb_{1-x}Fe_{2+x}$ and the insulating helimagnet $Cu_2OSeO_3$.

The continuous ferromagnetic transition in Fe-rich $Nb_{1-x}Fe_{2+x}$ can be suppressed and a ferromagnetic quantum phase transition can be reached by replacing Fe with Nb. $Nb_{1-x}Fe_{2+x}$ follows a trend that nature tends to avoid ferromagnetic quantum critical points. They are typically either replaced by a first order transition or masked by unconventional superconductivity. $Nb_{1-x}Fe_{2+x}$ offers a predicted third scenario: masking by a spin density wave phase. With neutron diffraction, the extension of the spin density wave phase in the field-temperature phase diagram has been determined. Additionally, cold neutron spectroscopy revealed low-energy magnetic excitations at zero field including soft quasi-elastic scattering in an extended region in reciprocal space, which reflects the proximity of the tuned system to different types of magnetic order.

The recently discovered skyrmion lattice in $Cu_2OSeO_3$ has created particular interest in this compound as its insulating properties allow the skyrmion lattice to be moved by an electrical field. Moreover, its magnetic ordering temperature increases with pressure, in contrast to the metallic helimagnets. In order to obtain information on the microscopic changes that might be responsible for the strengthening of the magnetic interactions, the structural properties of $Cu_2OSeO_3$ have been examined by X-ray diffraction. These studies reveal unusual changes in some Cu-O distances in the low pressure phase that undergoes an irreversible structural transformation to a yet unsolved high-pressure phase

at 9.7 GPa. Complementary Raman scattering and infrared absorption measurements confirm subtle changes in the low pressure phase and a marked change in optical properties accompanies the structural phase transition.

# Acknowledgements

Before we begin, I must first offer thanks to those who have guided me along the way. To Dr Philipp Niklowitz and Dr Heribert Wilhelm, thank you for your tireless supervision, for the opportunities you have afforded me and the knowledge you have shared. It has been truly invaluable and I would not be where I am today without either of you.

Thank you to the scientists and support staff of the I15 beamline, in particular, Dr D. Daisenberger, for his mentoring in all things high pressure, and Dr A. Kleppe for her advice and insight. To those students who preceded me, Dr C. Harrison and Dr T. Giles, with whom I spent many tireless hours in the lab. Although this was often to no avail, it was always a great pleasure. I consider myself extremely lucky to have worked with such a talented group of people.

To Dr T. Willis thank you for being a fantastic flatmate and an even better friend. To Dr D. Voneshen, thank you for your endless advice, expert scientific insight and inspirational dance moves. To my fellow students, Dan, Connor, Chris, Jim, Eron, Rupert, Alex, Tim, Jacob, Saeed, Harriet, Tom and Pardis, a PhD is an eclectic education that encompasses all aspects of life. I consider it a great privilege that I was able to experience mine in such fine company.

To Katie and David, you have become two of my closest friends. Thank you for putting up with my complaining and all our SCR lunches. Dave, I look forward to you leading the revolution. Thank you for letting me sleep on your sofa and our nightly Newsnight sessions. Katie, I can't wait to see you become a K-pop dance sensation. Thank you for always being around to listen.

Thank you to my parents and brother, for standing with me throughout my extended education. It has been a long road, thank you for always believing in me. I know you are glad it is finally over.

Finally, I offer thanks to my long-suffering partner Kimberley. I do not know how I would have made it through this process without her love and support. I know I can count on here to always be there for me and I am truly lucky to have her in my life.

# Contents

# List of Figures

# List of Tables

# Chapter 1

# Introduction

## 1.1 Physics of Magnetic Quantum Criticality

Understanding the new physics emerging from quantum phase transitions and quantum criticality remains one of the central goals in contemporary studies of correlated electron physics. The combination of the correlations found in the vicinity of continuous phase transitions, and quantum effects observed at low temperatures, combine to form the genesis of a large variety of exotic behaviour. This is most evident at the boundaries of magnetic order. Because of this, many compounds with magnetic phase transitions have been tuned in a way which suppresses their magnetic phase transitions to low temperatures. As a system is tuned towards a quantum critical point (QCP) a number of novel phases may emerge, such as non-Fermi liquids, which cannot be described in terms of independent fermionic quasiparticles and magnetically mediated unconventional superconductivity. Examples of this evolution of states may be found in heavy fermion systems [1], organic metals [2], alkali metal fullerides [3] and the high $T_C$ cuperates and iron pnictides [4][5].

## 1.2 Ferromagnetic Quantum Phase Transitions

With ferromagnetism (FM) being the simplest example of magnetic order, the switch from a paramagnetic (PM) to FM state is considered the archetypal magnetic phase transition. As such, a FM transition seen to be continuously suppressed to zero temperature (0 K) may be thought of as the archetypal FM quantum critical point (QCP). However, in real materials such a point is rarely observed, the system instead utilising one of a number of alternative scenarios in order to avoid quantum criticality. Figure 1.1 show a schematic representation of these various scenarios. There are numerous examples in which a system instead

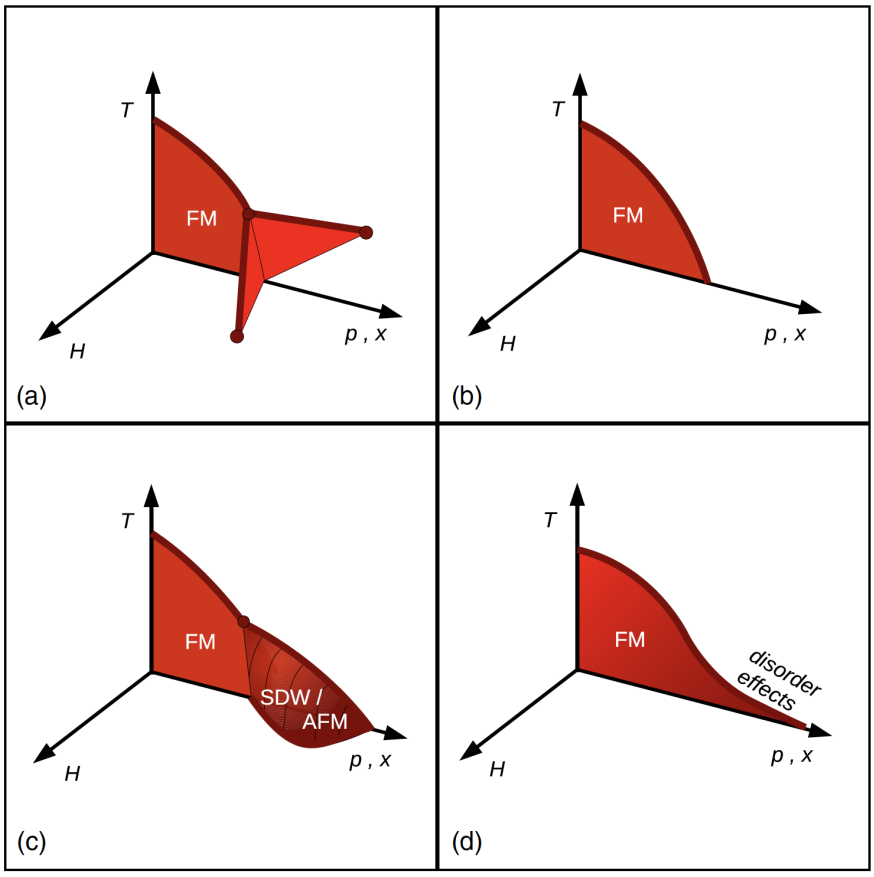


**Figure 1.1:** Schematic phase diagrams of transitions observed in ferromagnetic systems. $(a)$ a discontinuous transition and tricritical wings in a magnetic field, $(b)$ a continuous transition, $(c)$ a transition to an antiferromagnetic or spin density wave state and $(d)$ a continuous transition to a strongly disordered system, accompanied by a spin-glass freezing in the transition tail. Figure taken from [6]

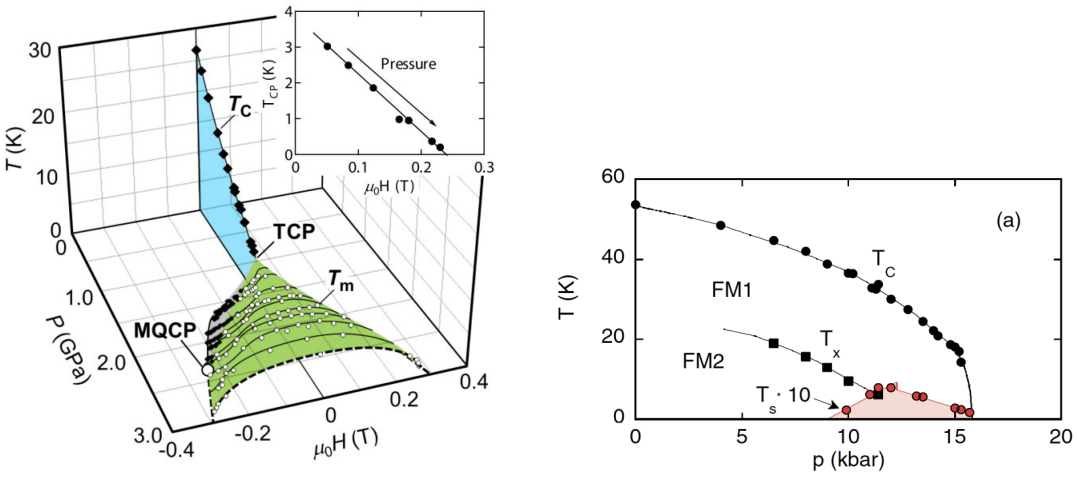


**Figure 1.2:** Phase diagrams of $ZnZr_2$ (*left*) [7] and $UGe_2$ (*right*) [8].

undergoes a first order transition, such the transition metals $ZrZn_2$ [7] and $Ni_3Al$ [9], transitioning at critical pressures of 1.6 GPa and 8 GPa respectively. There are then the ferromagnetic superconductors $UGe_2$ [8] and URhGe [10], these materials preferring to enter a superconducting state, demonstrating the intimate relation between magnetic order and superconductivity. Sum systems, such as $U_{1-x}Th_xNiSi_2$ [11] present a continuous transition accompanied by a spin-glass freezing in the transition tail, simply never reaching a QCP.

A fourth option is presented by the itinerant ferromagnet $Nb_{1-x}Fe_{2+x}$ during composition tuning, see figure 1.3. Here, replacement of Fe atoms by Nb atoms suppresses the continuous FM transition however, before the QCP is reached, a spin density wave (SDW) order emerges between the PM and FM phase masking the FM QCP. Other examples of this response are the PrPtAl system which orders into complex spirals at the PM-FM boundary [13] and ultra-pure samples of $Sr_3Ru_2O_7$ in which a quantum critical end point at finite magnetic field is avoided via the appearance of a nematic phase, featuring a spin-density wave order [14]. With the aim of further understanding this escape method, we probe the evolution of the low-energy excitation spectra through the PM, SDW and FM phases, as well as map the response of the SDW order to the application of an external magnetic field

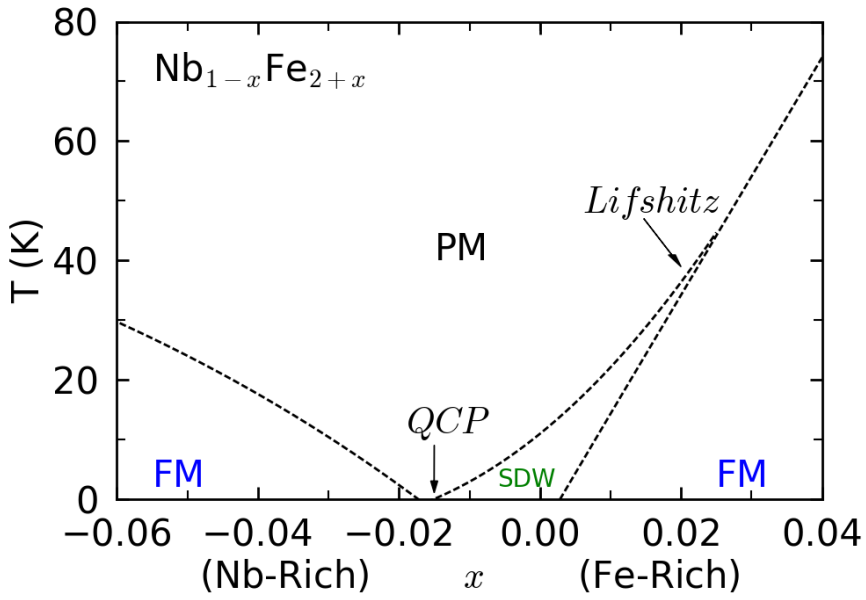


**Figure 1.3:** Temperature vs doping phase diagram of $Nb_{1-x}Fe_{2+x}$, showing quantum critical point (QCP) and Lifshitz point, adapted from [12].

## 1.3 Helimagnetism

The rich physics already associated with ferromagnetism motivates the study of systems displaying far more complex magnetic order. Helimagnetic alloys with B20 structure, such as MnSi, have been found to demonstrate field-induced magnetic phases with interesting topological properties, such as the so-called skyrmion phase, while pressure tuning these systems has revealed extended regions of non-Fermi liquid behaviour [15].

A skyrmion is a vortex like configuration of spins which forms a topologically stable, magnetic, particle-like object, between 10 and 100 nm in size. These quasiparticles can then be manipulated through the application of an external electrical field, creating the potential for use in high density magnetic storage and spintronic devises. In order to utilise this however, material problems, such as a low crystallisation temperature and low stability, must be overcome.

The formation of an ordered skyrmion lattice phase (SkX), until recently, has only ever been experimentally detected in specific metallic alloys with B20 structure, noted examples being MnSi [15], FeCoSi [17] and FeGe [18]. Each of

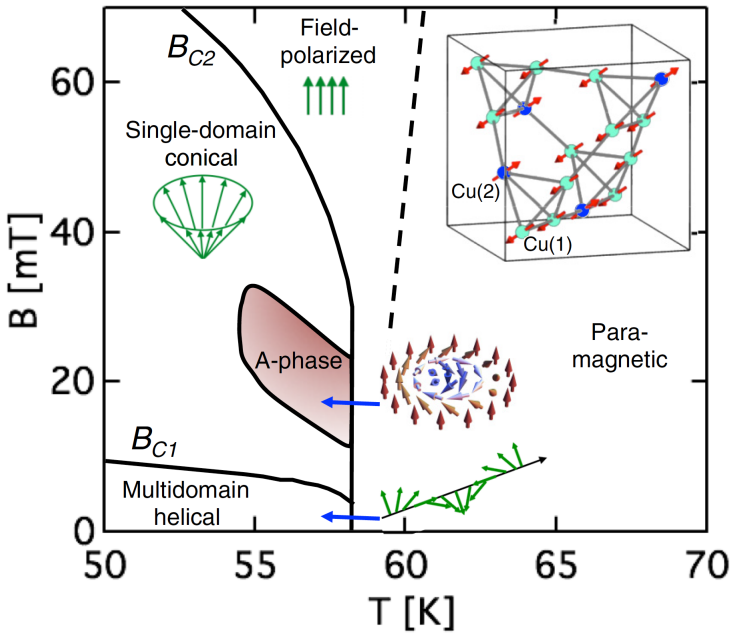


**Figure 1.4:** Schematic representation of the field-temperature phase diagram of $Cu_2OSeO_3$ , illustrating spin alignments of various phases. The inset shows the crystal structure with the two different $Cu^{2+}$ ion sites [16].

these systems orders in the chiral $P2_13$ space group and possesses a well defined helimagnetic ground state, linked intrinsically to the structure of the system. The application of pressure has been documented to induce both magnetic and electronic phase transitions [19], despite the structure of the systems remaining stable up to 30 GPa [20]. The distortion of the crystal lattice at higher pressures in hence likely linked to these phenomena.

In this thesis we will explore the $Cu_2OSeO_3$ system, the first insulator known to house a skyrmion lattice phase. $Cu_2OSeO_3$ crystallises in the $P2_13$ phase and displays a high level of structural stability down to low temperatures [21, 22]. Like in the intermetallic B20 compounds, field tuning induces then suppresses a Skyrmionic order, labelled as the A-phase in figure 1.4. Here, we perform an extensive investigation into the pressure response of the crystal structure of $Cu_2OSeO_3$ with the idea that even slight structural changes could result in significant changes to the magnetic phase of the system.

## 1.4 Synopsis

The remainder of this thesis is organised as follows: Chapter 2 contains a review of the basic concepts of solid-state crystal lattices along with diffraction from a crystal. It expands upon the concepts of phase transitions, quantum phase transitions and quantum criticality, with a focus on magnetic order. This includes a simple outline of spin fluctuation theory for low-energy excitations near magnetic quantum criticality. Chapter 3 then details the tools and techniques utilised in the measurement process, including a review of high pressure techniques, Raman and Infrared Spectroscopy and the practical set-up of X-ray and Neutron diffraction. Chapter 4 focuses on $NbFe_2$, discussing the evolution of the spin density wave order as a function of both temperature and applied magnetic field. The low-energy magnetic excitations in zero field, found through the paramagnetic, spin-density-wave and ferromagnetic phases are then probed and discussed. Chapter 5 presents measurement performed on the $Cu_2OSeO_3$ system, with an emphasis on the structural evolution of the system under pressure. Finally, in Chapter 6, the work is summarised and some avenues for future investigation suggested.

# Chapter 2

# Theoretical Basis

The majority of work presented in this thesis uses the elastic and inelastic scattering of X-rays and Neutrons to probe the lattice dynamics of crystalline systems. This chapter aims to provide the theoretical base, on which the practical investigations are performed; building first the picture of a crystal at the atomic level, before expanding to how the structural composition of a substance affects the fundamental behaviours of that system.

## 2.1 Description of a Crystal

The symmetries governing atomic positions observed within a crystal possess an intrinsic influence over the properties of the system. The ability, therefore, to accurately describe and categorise crystallographic structures is integral to the pursuit of understanding the physical properties shaping condensed matter.

A crystal may be described as the convolution of a "crystal lattice" with a "basis" of atoms or molecules. Hence, an idealised crystal lattice is an infinite array of discrete points positioned in three dimensional space [23], each described by a set of translational vectors:

$$\mathbf{R}_n = n_1\mathbf{a} + n_2\mathbf{b} + n_3\mathbf{c} \tag{2.1}$$

where $n = (n_1, n_2 \text{ and } n_3)$ are integers, $\mathbf{R}$ is the resulting position vector and $\mathbf{a}$, $\mathbf{b}$ and $\mathbf{c}$ are primitive vectors describing three non-coplanar axes. The vectors $\mathbf{a}$,

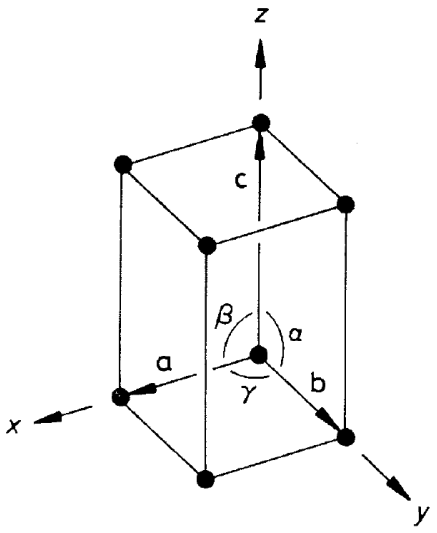


**Figure 2.1:** Crystallographic axes a, b and c of a unit cell of a primitive tetragonal crystal lattice [23].

**b** and **c** must be closed under vector addition and subtraction and for any chosen $\mathbf{R}_n$ the lattice must look identical in all respects.

These lattice vectors then define the unit cell, the simplest repeating unit within the structure of the crystal. This is a polyhedron constructed of edges with lengths **a**, **b** and **c** and separated by angles $\alpha$, $\beta$ and $\gamma$, as depicted in figure 2.1. The size of the unit cell is defined by the minimum lengths of **a**, **b** and **c** required for the cell to still fulfil the translational symmetry of the crystal lattice.

An atomic basis is then applied, anchoring singular or groups of atoms at the corners of the domain and creating a primitive cell [23]. Building on this, we also find face centred, body centred and base centred unit cells, each containing additional basis sights. Face centred describing a primitive cell with additional basis positions at the centre of each face, body centred an additional basis at the centre of the cell body and a base centred with additional positions found at the centre of two opposing faces [24].

In 1850, Bravais deduced that any three dimensional lattice may be classified as one of fourteen "types" dictated by the symmetry that it possessed, these are described in table 2.1 [24]. Each "symmetry" describes an operation which brings

**Table 2.1:** The 14 Bravais lattices [25]. Descriptions of the lattice arrangements are provided in the text of this section.

| | Crystal System | Unit Cell and angles | Bravais lattices |
|---|---|---|---|
| 1 | Cubic | $a = b = c$<br>$\alpha = \beta = \gamma = 90°$ | Primitive<br>Face Centered<br>Body centred |
| 2 | Orthorhombic | $a \neq b \neq c$<br>$\alpha = \beta = \gamma = 90°$ | Primitive<br>Face Centered<br>Body centred<br>Base Centered |
| 3 | Tetragonal | $a = b \neq c$<br>$\alpha = \beta = \gamma = 90°$ | Primitive<br>Body centred |
| 4 | Monoclinic | $a \neq b \neq c$<br>$\alpha = \gamma = 90°$ $\beta \neq 90°$ | Primitive<br>Base Centered |
| 5 | Rhombohedral | $a \neq b \neq c$<br>$\alpha = \beta = \gamma \neq 90°$ | Primitive |
| 6 | Triclinic | $a \neq b \neq c$<br>$\alpha \neq \beta \neq \gamma \neq 90°$ | Primitive |
| 7 | Hexagonal | $a = b \neq c$<br>$\alpha = \beta = 90°$ $\gamma = 120°$ | Primitive |

the crystal to a position indistinguishable from its original position. There are several types of symmetry, namely; rotational, reflection, inversion and rotation-reflection.

Taking the symmetry of the lattice as well as that of the basis allows the crystal to be classified as one of 32 possible point symmetry groups and, from here, one of 230 possible space symmetry groups. A space group is an array of symmetry elements within a space lattice [25]. Each symmetry element has a specific orientation and location within a unit cell and each cell contains an

identical array of symmetry elements, repeated throughout the crystal. Each element is positioned such that each symmetry operation will bring all elements into self-coincidence. Many space groups simply describe a rotational, reflection, inversion or rotation-reflection symmetry possessed by point groups located at lattice sites, some however go further, taking into account glide planes and screw axes; glide planes describing a reflection followed by a translation and screw axes describe a rotation followed by a translation. Determining the space group of a crystallographic system is, in many cases, the ultimate goal of a crystallographer.

Once the lattice parameters and unit cell are determined, in order to complete the description of the crystal it is necessary to specify the atoms contained within the unit cell, along with their position relative to the origin [23]. The atomic positions is therefore defined such that the position of atom $j$ is given by the basis vector $\mathbf{r}_j$, defined as:

$$\mathbf{r}_j = x\mathbf{a} + y\mathbf{b} + z\mathbf{c} \tag{2.2}$$

where $x$, $y$ and $z$ are fractional coordinates. Combining this with equation 2.1, it becomes possible to describe the position of any atom within a crystal through the combination of position vector and basis vector, $\mathbf{R} = \mathbf{R}_n + \mathbf{r}_j$.

### 2.1.1 Scattering from a Crystal

Now we are able to describe accurately the positions and symmetries found within a crystal, we can work on developing a picture of how photons and neutrons interact with a crystalline systems. In 1913 Bragg laid out the first formulation for the condition of constructive interference:

$$2d\sin(\theta) = n\lambda \tag{2.3}$$

In which $d$ is the inter-atomic spacing, $\theta$ is the incident angle of radiation and $n$ is an integer. The formula dictates that constructive interference will occur when the spacing between the scattering planes, $d$, is an integer multiple of the wavelength of incident light, $\lambda$. When scattered from a three dimensional crystal, this constructive interference manifests as an array of diffraction peaks,

known as Bragg peaks, each corresponding to a specific set of atomic planes. Although Braggs law is sufficient to provide information on inter-atomic distances, it provides no information regarding diffraction intensities, hence, a more detailed approach is required. For simplicity we will consider the elastic case.

Let us begin with a plane wave of the form $A_0 e^{i\mathbf{k}}$, with amplitude $A_0$ and wave vector $\mathbf{k} = 2\pi/\lambda$. We next assume it is incident on some atom, within our crystal, at position $\mathbf{R}$. If the scattering is weak, then the contribution of that atom to the scattering intensity at the detector may be written as:

$$A_R = A_0 e^{i\mathbf{k}.\mathbf{R}} \times f \times \frac{e^{i\mathbf{k}(\mathbf{D}-\mathbf{R})}}{|\mathbf{D}-\mathbf{R}|} \tag{2.4}$$

where $\mathbf{D}$ is the distance between the detector and the crystallographic origin and $f$ is the atomic "form" or "scattering" factor. Given the very small distance between the origin and our atom, $\mathbf{D}$ and $\mathbf{D}-\mathbf{R}$ may be taken as being parallel to the scattering vector $\mathbf{q}$ and we can therefore reduce equation 2.4 to:

$$A_{\mathbf{R}} \approx A_0 \frac{e^{i\mathbf{k}.\mathbf{R}}}{D} f e^{-i\mathbf{q}.\mathbf{R}} \tag{2.5}$$

where $\mathbf{q} = \mathbf{k}_i - \mathbf{k}_r$, with $\mathbf{k}_i$ and $\mathbf{k}_r$ being the incident and reflected wave vectors respectively. From here, $A_0 e^{i\mathbf{k}}/\mathbf{D}$ can be factorized out, given it is the same for all the atoms in the crystal, leaving an expression that describe the scattering amplitude of the $n^{th}$ atom:

$$F(\mathbf{q}) = \sum_{\mathbf{R}\ n} e^{i\mathbf{q}.\mathbf{R}_n} \tag{2.6}$$

If we now expand $\mathbf{R}$, in equation 2.6, it becomes clear that the total scattering amplitude is the product of a lattice term, containing $\mathbf{R}_n$, and an atomic basis term, $\mathbf{r}_j$:

$$F(\mathbf{q}) = \sum_{\mathbf{R}_n} e^{i\mathbf{q}.\mathbf{R}_n} \times \sum_{\mathbf{r}_j} f(\mathbf{q})_j e^{\mathbf{q}.\mathbf{r}_j} \tag{2.7}$$

where, $\mathbf{q}$ dictates the direction of scatter and $f(\mathbf{q})_j$ the scattering length.

Breaking this down further, the first factor in equation 2.7, the lattice sum contribution, is non-zero only for $\mathbf{q}.\mathbf{R}_n = 2\pi n$, where $n$ is an integer. In order to find a solution, reciprocal space basis vectors $\mathbf{a}^*$, $\mathbf{b}^*$, and $\mathbf{c}^*$ are introduced:

$$\mathbf{a}^* = \frac{2\pi \mathbf{b} \times \mathbf{c}}{\mathbf{a} \cdot (\mathbf{b} \times \mathbf{c})} \qquad \mathbf{b}^* = \frac{2\pi \mathbf{c} \times \mathbf{a}}{\mathbf{a} \cdot (\mathbf{b} \times \mathbf{c})} \qquad \mathbf{c}^* = \frac{2\pi \mathbf{a} \times \mathbf{b}}{\mathbf{a} \cdot (\mathbf{b} \times \mathbf{c})}$$

From these definitions the following conditions are fulfilled:

$$\begin{aligned} \mathbf{a} \cdot \mathbf{a^*} &= 2\pi \\ \mathbf{b} \cdot \mathbf{b^*} &= 2\pi \\ \mathbf{c} \cdot \mathbf{c^*} &= 2\pi \end{aligned} \tag{2.8}$$

From these basis vectors, any point in the reciprocal lattice can be specified using the reciprocal lattice vector:

$$\mathbf{G}_{hk\ell} = \mathbf{q} = h\mathbf{a^*} + k\mathbf{b^*} + \ell\mathbf{c^*} \tag{2.9}$$

where $(h, k, \ell)$ are the Miller indices. This shows that scattered intensity is only observed when $\mathbf{q} = \mathbf{G}$, i.e. the Laue condition is fulfilled. When this condition is satisfied, the lattice sum is then simply proportional to the number of unit cells within the crystal [23].

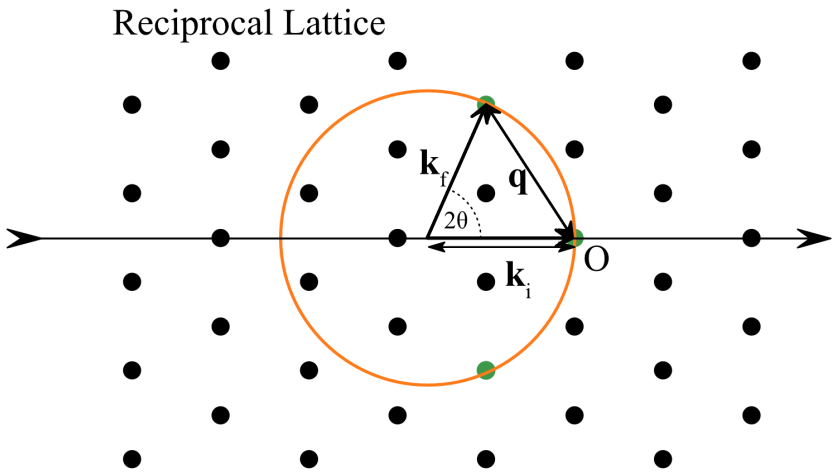


**Figure 2.2:** Ewald sphere construction.

The Bragg equation remains consistent, following readily from the Laue condition (eq.2.9). From figure 2.2 it can be inferred that the scattering triangle yields:

$$\frac{\mathbf{q}}{2} = \mathbf{k}\sin(\theta) \tag{2.10}$$

With $\mathbf{q} = 2\pi/d_{hk\ell}$ and $\mathbf{k} = 2\pi/\lambda$ one obtains the Bragg equation:

$$2d_{hk\ell}\sin(\theta_{hk\ell}) = \lambda \tag{2.11}$$

The second term in equation 2.7 represents a sum over all the atoms contained within the basis. If, therefore, the basis consists of a single atom, $\mathbf{r}_j = 0$, then:

$$F(\mathbf{q}) = f(\mathbf{q}) \tag{2.12}$$

where $f(\mathbf{q})$ is the atomic form factor of the atom under consideration. The physical implication of this is then that any variation of diffraction peak intensities is due only to the atomic form factor $f(\mathbf{q})$ [23].

In the case of a diatomic basis, for example the hexagonal close-packed structure, in which atoms are located at $\mathbf{r}_1 = 0$ and $\mathbf{r}_2 = \frac{1}{3}\mathbf{a} + \frac{2}{3}\mathbf{b} + \frac{1}{2}\mathbf{c}$, one obtains:

$$F(\mathbf{q}) = f(e^{i0} + e^{i2\pi(\frac{h}{3}+\frac{2k}{3}+\frac{\ell}{2})}) \tag{2.13}$$

For some combinations of $(h, k, \ell)$, the expected intensities will be zero (all (0 0 $\ell$) with $\ell$ = odd), due to the destructive interference of the scattering. However, it is important to remember that this is an idealised case, and assumes chemically identical atoms, in idealised crystallographic environments. In reality, slight variations and imperfections in the chemical make-up of a system result in deviations in $f$ and generate very weak diffractions peaks arising in these forbidden directions.

The atomic form factor is a measure of the scattering amplitude of a wave by an isolated atom [23]. It is also dependent on the nature of the incident radiation, be it X-ray, neutron or electron. X-rays are scattered by the electron cloud of the atom, hence the scattering amplitude is proportional to the atomic numbers $Z$ of the atoms in the sample [26]. Neutrons, no the other hand, are scattered by two distinct interactions, nuclear and magnetic [27]. Nuclear scattering sees the neutron scattered from the nucleus of the atom, which then acts as a point source, radiating scattered neutrons as a spherical wave. This interaction is mediated by the strong nuclear force, with each isotope possessing a different scattering amplitude. Magnetic scattering refers to the interaction between the neutrons magnetic moment and that of the unpaired electrons in outer shell orbits, and is therefore independent from the specific atomic isotope.

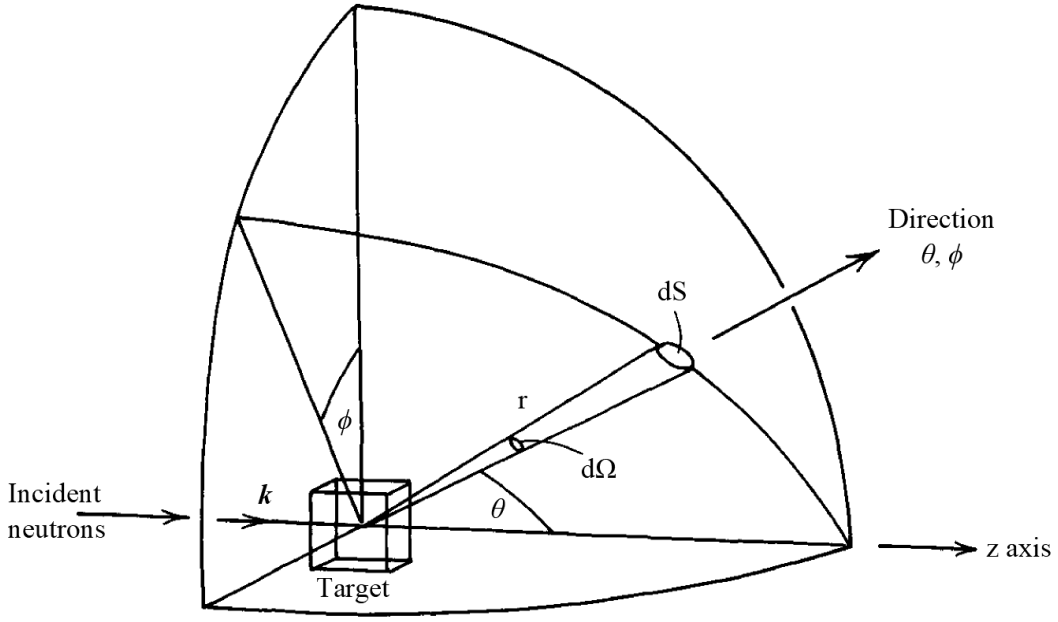


**Figure 2.3:** Geometry of neutron scattering [27].

When scattering via the strong nuclear force, the direction of scatter is described via the polar coordinates $\theta$ and $\phi$, see figure 2.3. The total scattering cross section describes the total number of neutrons scattered, per second, in all directions divided by the initial flux [27]. From this, the partial differential cross-section is defined as the number of neutrons scattered per second into a small solid angle $d\Omega$ in the direction $\theta$, $\phi$ and with a final energy between $E'$ and $E' + dE'$. This is expressed as:

$$\frac{d^2\sigma}{d\Omega dE'} \tag{2.14}$$

Let us now take a neutron, of the form $\psi_{\mathbf{k}} = e^{i\mathbf{k}.\mathbf{r}}$ and with wavevector $\mathbf{k}$. This neutron is incident on a scattering system, $\chi$, in state $\lambda$, expressed $\chi_\lambda$, and interacts with that system via a potential $V$. This scattering event is described via the probability, $|\langle \mathbf{k}'\lambda'|V|\mathbf{k}\lambda\rangle|^2$, and leads to an expression for the partial differential cross section:

$$\left(\frac{d^2\sigma}{d\Omega dE'}\right)_{\lambda\to\lambda'} = \frac{\mathbf{k}'}{\mathbf{k}}\left(\frac{m}{2\pi\hbar^2}\right)^2 |\langle \mathbf{k}'\lambda'|\hat{V}|\mathbf{k}\lambda\rangle|^2 \delta(E_\lambda - E_{\lambda'} + E - E') \tag{2.15}$$

describing a scattering event in which the system goes from state $\lambda$ to $\lambda'$. Conservation of energy is accounted for by the Dirac delta term, with $E$ and $E'$ being

initial and final energies of the neutron and $E_\lambda$ and $E_{\lambda'}$ being the initial and final energy of the scattering system. Here $\mathbf{k}'$ represents the dependence of the infinitesimal phase space volume on $E'$ and $1/\mathbf{k}$ normalising by the flux.

Equation 2.15 describes the nuclear scattering of unpolarised neutrons, however, the spin states of the incoming and outgoing neutron, $\sigma$ and $\sigma'$, respectively, may also be specified. Thus leading becoming:

$$\left(\frac{d^2\sigma}{d\Omega dE'}\right)_{\sigma\lambda\to\sigma'\lambda'} = \frac{\mathbf{k}'}{\mathbf{k}}\left(\frac{m}{2\pi\hbar^2}\right)^2 |\,\langle \mathbf{k}'\sigma'\lambda'|\hat{V}_m|\mathbf{k}\sigma\lambda\rangle\,|^2\delta(E_\lambda - E_{\lambda'} + \hbar\omega) \quad (2.16)$$

We now have an expression that details the system changing from state $\lambda$ to $\lambda'$, while the neutron changes from $\mathbf{k}\sigma$ to $\mathbf{k}'\sigma'$, through a magnetic potential interaction, $V_m = -\mu_n \cdot \mathbf{B}$ where $\mathbf{B}$ is the total magnetic field due to an orbiting electron, $\mu_n$ is the magnetic moment of the neutron and $\hbar\omega$ is the neutron energy change.

Assuming unpolarised neutrons allows us to take the probability for each spin orientation of incoming neutrons to be equal [28]. This leads us to a scattering probability of:

$$\langle\lambda'|\hat{\mathbf{Q}}|\lambda\rangle = \sum_{ld} e^{i\boldsymbol{\kappa}\cdot\mathbf{R}_{\ell d}} F_d(\boldsymbol{\kappa})\,\langle\lambda'|\hat{\mathbf{S}}_{ld}|\lambda\rangle \quad (2.17)$$

where $\hat{\mathbf{Q}} = (1/2\mu_B)\mathbf{M}(\boldsymbol{\kappa})$ is the Fourier transform of the total magnetisation operator, $\hat{\mathbf{S}}_{\ell d}$ is the total spin operator, which delivers the total angular momentum (including orbital angular momentum and spin) of the outer shell electrons of magnetic ion $d$ in unit cell $\ell$ and $F_d(\boldsymbol{\kappa})$ is the form factor of the scattering vector $\boldsymbol{\kappa} = \mathbf{k} - \mathbf{k}'$ from ion $d$, the form factor being the Fourier transform of the spacial spin distributions of the magnetic ions. Finally, $\mathbf{R}_{\ell d}$ is the position vector of the unit cell, within the lattice. Using this equation as the scattering probability leads to:

$$\begin{aligned}\frac{d^2\sigma}{d\Omega dE'} = \left(\frac{m}{2\pi\hbar^2}\right)^2 (2\gamma\mu_n\mu_B)^2(4\pi)^2\frac{k'}{k}\sum_{\lambda\lambda'\sigma\sigma'} p_\lambda p_\sigma \\ \times\,\langle\lambda\sigma|(\hat{\boldsymbol{\sigma}}\cdot\hat{\mathbf{Q}}_\perp)^\dagger|\lambda'\sigma'\rangle\,\langle\lambda'\sigma'|\hat{\boldsymbol{\sigma}}\cdot\hat{\mathbf{Q}}_\perp|\lambda\sigma\rangle\,\delta(\hbar\omega E_\lambda - E_{\lambda'})\end{aligned} \quad (2.18)$$

where $\hat{\mathbf{Q}}_\perp$ is the total magnetic moment, combining spin and momentum contributions and $\gamma = -1.91$ is the gyromagnetic ratio. This equation, in turn, leads to

an expression for the partial differential cross-section for the magnetic scattering by ions:

$$\begin{aligned}\frac{d^2\sigma}{d\Omega dE'} =& r_0^2 \frac{k'}{k} \sum_{\alpha\beta} (\delta_{\alpha\beta} - \tilde{\boldsymbol{\kappa}}_\alpha \tilde{\boldsymbol{\kappa}}_\beta) \sum_{\lambda\lambda'} p_\lambda \sum_{ld} \sum_{l'd'} F_d^*(\boldsymbol{\kappa}) F_{d'}(\boldsymbol{\kappa}) e^{i\boldsymbol{\kappa}\cdot(\mathbf{R}_{l'd'} - \mathbf{R}_{ld})} \\ & \times \langle \lambda | \hat{\mathbf{S}}_{ld}^\alpha | \lambda' \rangle \langle \lambda' | \hat{\mathbf{S}}_{l'd'}^\beta | \lambda \rangle \, \delta(\hbar\omega + E_\lambda - E_{\lambda'})\end{aligned} \tag{2.19}$$

here, $F_d^*(\boldsymbol{\kappa})$ and $F_{d'}(\boldsymbol{\kappa})$ are form factors, $\alpha$ and $\beta$ are Cartesian components of scattering, $p_\lambda$ expresses the probability of the system being in the initial state $\lambda$ and $\langle \lambda | \hat{\mathbf{S}}_{ld}^\alpha | \lambda' \rangle$ and $\langle \lambda' | \hat{\mathbf{S}}_{l'd'}^\beta | \lambda \rangle$ are overlap integrals, from which the scattering probability can be determined. In this equation, the neutron selection rule is expressed via the term $\sum_{\alpha\beta} (\delta_{\alpha\beta} - \tilde{\boldsymbol{\kappa}}_\alpha \tilde{\boldsymbol{\kappa}}_\beta)$.

Next, using the identity:

$$\hat{A}(t) = e^{\frac{i\hat{\mathcal{H}}t}{\hbar}} \hat{A} e^{-\frac{i\hat{\mathcal{H}}t}{\hbar}} \tag{2.20}$$

and assuming only a Bravais lattice or a non-Bravais lattice with only one magnetic ion per unit cell, it is possible to reduce equation 2.19 to:

$$\frac{d^2\sigma}{d\Omega dE'} = r_0^2 \frac{k'}{k} \left\{ \frac{g}{2} F(\boldsymbol{\kappa}) \right\}^2 e^{-2W(\boldsymbol{\kappa})} \times \sum_{\alpha\beta} (\delta_{\alpha\beta} - \tilde{\boldsymbol{\kappa}}_\alpha \tilde{\boldsymbol{\kappa}}_\beta) \frac{1}{2\pi\hbar} \int_{-\infty}^{\infty} dt e^{-i\omega t} \langle \hat{S}_{\boldsymbol{\kappa}}^\alpha \hat{S}_{-\boldsymbol{\kappa}}^\beta(t) \rangle \tag{2.21}$$

in which $r_0^2$ is a scaling constant, $g$ is the Landé splitting factor for the ion, $F(\boldsymbol{\kappa})$ the ion form factor and $e^{-2W(\boldsymbol{\kappa})}$ is the Debye-Waller temperature dependence of the scattering process, previously contained within the set of state probabilities $p_\lambda$. Finally, $\langle \hat{S}_{\boldsymbol{\kappa}}^\alpha \hat{S}_{-\boldsymbol{\kappa}}^\beta(t) \rangle$ defines the thermal averaging for the system.

Evaluation of the thermal average leads to the expression:

$$\begin{aligned}\frac{d^2\sigma}{d\Omega dE'} =& r_0^2 \frac{k'}{k} \left\{ \frac{g}{2} F(\boldsymbol{\kappa}) \right\}^2 e^{-2W(\boldsymbol{\kappa})} \sum_{\alpha\beta} (\delta_{\alpha\beta} - \tilde{\boldsymbol{\kappa}}_\alpha \tilde{\boldsymbol{\kappa}}_\beta) \\ & \times \left[ \underbrace{(1 + n(\omega)) \left( \frac{-N}{\pi g \mu_\beta} \right) Im\chi_{\boldsymbol{\kappa}}^{\alpha\beta}(-\omega)}_{\text{Inelastic scattering}} + \underbrace{\delta(\hbar\omega) \langle \hat{S}_{\boldsymbol{\kappa}}^\alpha \rangle \langle \hat{S}_{-\boldsymbol{\kappa}}^\beta \rangle}_{\text{Elastic scattering}} \right]\end{aligned} \tag{2.22}$$

which contains the elastic and inelastic components of the scattering signal. The inelastic component includes the detailed balance factor, $(1 - n(\omega))$, and the Imaginary part of the dynamical susceptibility, $Im\chi_{\boldsymbol{\kappa}}^{\alpha\beta}$.

## 2.2 Phase Transitions

As a material undergoes a finite temperature phase transition, the low temperature phase is typically characterised by a higher degree of order corresponding to a lower total entropy of the system [29]. This low-temperature ordered phase is described by an order parameter and characterised by a decrease in the overall symmetry, the archetypal example being an isotropic paramagnet transitioning to a non-isotropic ferromagnet. At zero magnetic field, the symmetry of the system is lowered due to the magnetic spins no longer being randomly aligned, meanwhile the order parameter, in this case magnetisation $M$, increases from zero to some nonzero value, see figure 2.4.

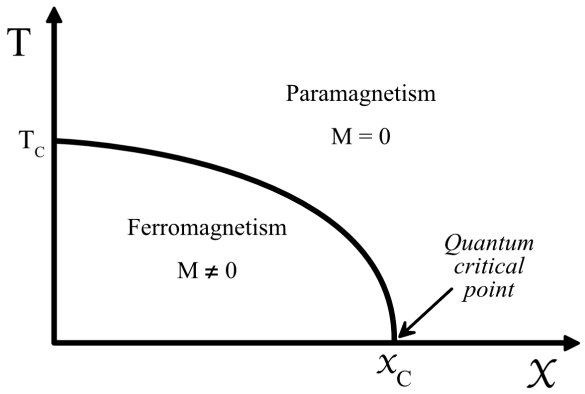


**Figure 2.4:** Second order phase transition between ferromagnetic and paramagnetic states, driven by temperature and a tuning parameter $x$. While in the PM phase, the magnetic moments are misaligned producing no net magnetisation, $M = 0$. As the system transitions to the FM phase, moments align and a net magnetisation arises, $M \neq 0$. Accompanying the magnetisation, the symmetry of a previously isotropic PM system is lowered by the formation of FM with an associated direction of net magnetisation.

To expand this, let us consider the first law of thermodynamics applied to the case of a magnet at fixed volume [30]. The change in internal energy $dU$ is simply given by:

$$dU = TdS - MdH \tag{2.23}$$

where $T$ is temperature, $dS$ is the change in entropy, $M$ is magnetisation and $dH$

is the change in applied field. The thermodynamic definition of free energy $\mathcal{F}$ is:

$$\mathcal{F} = U - TS \tag{2.24}$$

with $\mathcal{F}$ dependent on field and temperature: $\mathcal{F} \equiv \mathcal{F}(H, T)$. Next, taking the partial derivative with respect to field, one obtains the magnetisation:

$$\left(\frac{\partial \mathcal{F}}{\partial H}\right) \propto M \tag{2.25}$$

If a discontinuity is observed in the order parameter of a system, in this scenario $M$, the transition is considered to be of the first order. If we then take the second partial derivative of the free energy with respect to external field we arrive at:

$$\left(\frac{\partial^2 \mathcal{F}}{\partial H^2}\right) \propto \left(\frac{\partial M}{\partial H}\right) = \chi \tag{2.26}$$

A second order transition then presents a discontinuity (typically a divergence) in the second derivative of the order parameter. In the FM-PM transition, this manifests as a divergence in the susceptibility and is hence characterised by thermally excited critical spin fluctuations.

The study of phase transition, and the physical processes governing the behaviour of the system as they are approached, can in many ways can be considered a central tenet of condensed matter physics. At the core of this, lies ferromagnetism. In the early 1900s, the study of these transitions by Weiss lead to the formation of the first iteration of mean-field theory [31]. This was then built upon in 1938, by Stoner, who established the mechanisms by which a nonzero magnetization may arise through the spontaneous splitting of conduction bands [32].

The Landau theory of ferromagnetism is able to apply mean field theory to build a model of a FM-PM transition, without the need for microscopic calculations. Instead, the system's free energy is assumed to be a power expansion of the order parameter, magnetisation $M$:

$$\mathcal{F} = a(T)^2 + bM^4 + c \tag{2.27}$$

where $b$ and $c$ are constants, with $b$ assumed to be greater than 0, and $a(T)$ is dependent on the temperature of the system. Due to the symmetry of the system ($M = -M$), odd terms are excluded.

A ferromagnetic phase transition at $T = T_C$ is modelled with $a(T)$ of the form $a(T) = a0(T - T_C)$, where $a_0$ is a positive constant. The partial derivative, with respect to $M$ yields the equation:

$$\left(\frac{\partial \mathcal{F}}{\partial M}\right) = 2aM + 4bM^3 = 0 \tag{2.28}$$

and the minimum of $\mathcal{F}$ is located at:

$$\begin{gathered} M = 0 \text{ for } \mathrm{T} > \mathrm{T}_C \\ \textit{or} \\ M = \pm\left(\frac{a}{2b}\right)^{1/2} = \pm\left(\frac{a_0(T - T_C)}{2b}\right)^{1/2} \text{ for } \mathrm{T} < \mathrm{T}_C \end{gathered} \tag{2.29}$$

which includes the square root temperature dependence of the magnetic order parameter. As studies continue and measurement techniques improved however, it becomes clear that mean-filed theory is not sufficient to fully describe the behaviour of FM in the vicinity of phase transitions [33], many materials critical exponents deviating from this power 1/2 value. Thus ferromagnetism became the testing grounds for the theory of critical phenomena [34].

Phase transitions can be suppressed by non-thermal tuning parameters, such as chemical composition, pressure, magnetic or electric fields, to zero temperature [29], this is called a quantum phase transition. When such a transition is of second order it may also be referred to as a quantum critical point (QCP). The classical free-energy functions used in Landau-Ginzburg-Wilson interpretations can no longer accurately describe the system . Hertz generalised this approach by introducing imaginary time [35]. Millis determined the range in which the electrons can be integrated out and the system can be described by an effective bosonic theory [36], which describes the system's spin fluctuations.

Closer inspection of these points finds that the critical spin fluctuations are no longer classical in nature but instead modified by quantum statistics. These

quantum fluctuations strongly influence the physics near a QCP [37, 35]. More recently, focus has been drawn to metallic ferromagnets displaying low Curie temperatures ($< 100$ K). In some heavy fermion systems it has been observed that selective Mott transitions, i.e., the exclusive localisation of $f$-electrons at the magnetic quantum critical point, might be observed and influence the physics near the QCP [38]. In other cases, these strong correlations near quantum criticality can lead to new emergent phases such as unconventional superconductivity, seen in $UGe_2$ [8], or a modulated magnetic order, such as is present in the weak metallic $d$-metal ferromagnet $NbFe_2$ [39]. This thesis continues the investigation of $NbFe_2$ with the aim to explore the itinerant limit of quantum criticality, where selective Mott localisation is not expected.

## 2.3 Spin Fluctuation Theory

As one might expect, spin plays a vital role in determining the order of the system and, when combined with electron-electron interactions, often lead to unconventional phenomena. In the case of conducting materials, the Coulomb interaction leads to strong local, non static, spin alignment. In such a state the electrons are still able to move rapidly, but the spin density they produce is seen instead to undergo slow, large-amplitude spontaneous fluctuations. In the case of a typical ferromagnet, these fluctuations are found to possess specific wave vectors with a finite amplitude. Increasing the temperature of the system then "melts" the frozen-in magnetic structure, increasing the entropy of the system and reducing the overall order [40].

However, when this transitions occurs isothermally, driven instead by some alternate parameter such as field or pressure, this change in entropy is not longer present. Hence, the system cannot be viewed as moving from an ordered to disordered state, but rather from a conventional order to a hidden order. In such a transition, the conventional order parameter undergoes spontaneous quantum fluctuation.

To understand this, let us consider first the effects of the electron-electron interaction under an applied magnetic field $H$, producing a magnetisation $M$ of:

$$M = \chi_0(H + \lambda M) \tag{2.30}$$

where $\lambda M$ is the exchange field, $\lambda$ is a coupling constant and $\chi_0$ is the magnetic susceptibility when $\lambda \to 0$. Solved for $M$, we obtain a final susceptibility of:

$$\chi = \chi_0/(1 - \lambda\chi) \tag{2.31}$$

From this, we can then see than while $\lambda\chi_0 \geq 1$, magnetic polarisation can occur spontaneously in the absence of the applied field, with the feedback produced by the exchange field being critical or over-critical in nature. This is similar to a self-oscillating feedback amplifier, the amplitude of the spontaneous polarisation governed by the anharmonicities of the system [40].

We shall next expand on this, in order to build a space and time dependent picture of the average magnetisation $M(\mathbf{r}, t)$ in the presence of an applied magnetic field $H(\mathbf{r}, t)$. This is achieved using the Ginzburg-Landau postulate of the field equation. In order to simplify the model only fluctuations with frequencies, $\omega$, and wavevectors, $\mathbf{q}$, far smaller than the Fermi energy and Brillouin zone are considered, giving rise to relatively slow, large amplitude fluctuations.

To begin we recall the case of a uniform static field $H$, stabilising a magnetisation $M$ via some relation $H = H(M)$. This function must be odd in $M$ for an isotropic system, hence, through Taylor expansion, we arrive at the expression:

$$H = a_0 M + b_0 M^3 \tag{2.32}$$

where $a_0$ is the inverse Pauli susceptibility and $b_0$ is the anharmonicity parameter. Including the effects of the exchange field, $\lambda M$, we come to:

$$H(M) = aM + bM^3 \tag{2.33}$$

with $a = a_0 - \lambda$, and $b = b_0$ if the exchange field is assumed to be linear in $M$. Given ours is the non linear case, we may assume $b = 0$. With this initial condition, we then consider the spatial variation of the magnetisation, introducing

a parameter dependant on the systems resistance to the magnetic modulation, $c$, bringing us to the equation:

$$H = H[M] = aM - c\nabla^2 M \tag{2.34}$$

The square brackets indicating a mapping of one function of $\mathbf{r}$ to another.

It is useful at this point to introduce an effective field:

$$H_{eff} = H - H[M] \tag{2.35}$$

where $H$ is the applied field and $H[M]$ is equal to equation 2.34, and vanishes when the system is in equilibrium (equation 2.34 is satisfied).

A time dependence is next applied to this model through the introduction of a linear restoring term:

$$\dot{M} = \gamma * H_{eff} \tag{2.36}$$

here, $\dot{M}$ indicating the time derivative and $*$ a spatial convolution, and $\gamma$ is a relaxation function.

If one then performs a Fourier transform on this model, as described in [40], we find the dynamical susceptibility $\chi(\mathbf{q}, E)$ is defined by the following set of expressions:

$$H(\mathbf{q}, E) = \chi^{-1}(\mathbf{q}, E)M(\mathbf{q}, E) \tag{2.37}$$

where:

$$\chi^{-1}(\mathbf{q}, E) = \chi_{\mathbf{q}}^{-1}(1 - i\frac{E}{\Gamma_{\mathbf{q}}}) \tag{2.38}$$

$$\chi_{\mathbf{q}}^{-1} = \chi^{-1} + c\mathbf{q}^2 \tag{2.39}$$

and:

$$\Gamma_{\mathbf{q}} = \gamma_{\mathbf{q}}\chi_{\mathbf{q}}^{-1} \tag{2.40}$$

With this, $\chi(\mathbf{q}, E)$ is the generalised linear susceptibility, equal to $M(\mathbf{q}, E)/H(\mathbf{q}, E)$, analogues to the uniform case. The spectrum $\Gamma_{\mathbf{q}}$ is interpreted as the rate at which a component magnetisation, $M_{\mathbf{q}}(t)$, will relax to the equilibrium $H = 0$, while $\gamma_{\mathbf{q}} = \gamma\mathbf{q}^n$ and is the Fourier component of $\gamma$.

Considering the implications of this in a physical system, we are able to build a picture of how a disturbance will relax in the absence of an external field.

If the system is a homogeneous non-interacting Fermi system then relaxation occurs purely via the ballistic motion of the fermions, typically moving at the Fermi velocity. Hence, so long as the wavelength remains in the low $\mathbf{q}$ limit, the relaxation time is proportional to the wavelength of the disturbance, $\Gamma \propto \mathbf{q}$, implying $n = 1$. This is seen in the case of ferro and paramagnetism.

This linearity, known as Landau damping, survives in a Fermi liquid, however breaks down as a critical point is approached where upon the critical fluctuations tend to freeze. The slowing down of the fluctuations is naturally indicative of a second order transition. Once frozen, the relaxation of fluctuations is instead

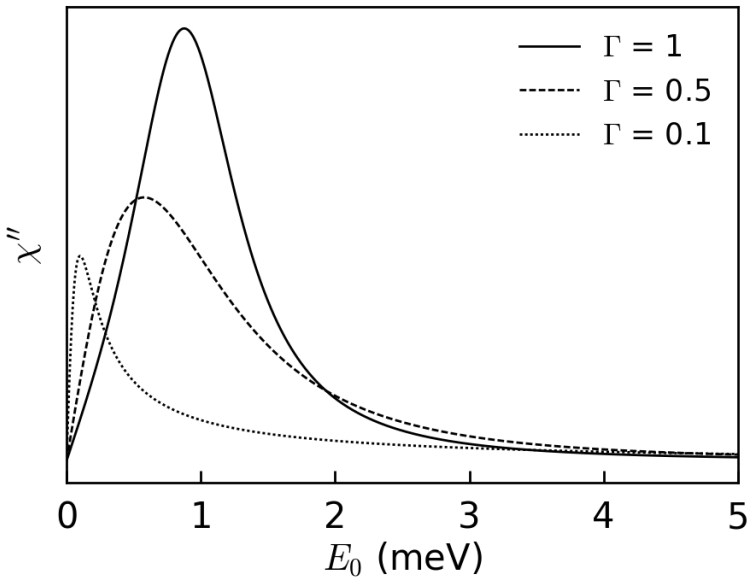


**Figure 2.5:** This plot demonstrates the effect of increased damping $\Gamma$, with fixed $\chi$ and $E$ values.

governed by diffusive rather than ballistic motion and hence the relaxation time becomes proportional to the the wavelength squared, $\Gamma \propto \mathbf{q}^2$, $n = 2$.

Turning next to susceptibility of the excitation, this represents the energy dependent response of each magnetic mode. In the case of the ferromagnetic phase transition, the imaginary part of the dynamic susceptibility is well described by the over-damped harmonic oscillator function [41]:

$$\chi''(\mathbf{q}, E) = \chi(\mathbf{q}, 0) \frac{E\Gamma_{\mathbf{q}}}{E^2 + \Gamma_{\mathbf{q}}^2} \tag{2.41}$$

This can be derived from equation 2.38:

$$\begin{aligned}
\chi^{-1}(\mathbf{q}, E) &= \chi_{\mathbf{q}}^{-1}(1 - i\frac{E}{\Gamma_{\mathbf{q}}}) \\
\Rightarrow \chi(\mathbf{q}, E) &= \frac{\chi_{\mathbf{q}}}{1 - i\frac{E}{\Gamma_{\mathbf{q}}}} = \frac{\chi_{\mathbf{q}(1+i\frac{E}{\Gamma_{\mathbf{q}}})}}{1 + \frac{E^2}{\Gamma_{\mathbf{q}}^2}} \\
\Rightarrow \chi'' &= \frac{\chi_q \frac{E}{\Gamma_{\mathbf{q}}}}{1 + \frac{E^2}{\Gamma_{\mathbf{q}}^2}} \\
&= \frac{\chi_{\mathbf{q}} \Gamma_{\mathbf{q}} E}{\Gamma_{\mathbf{q}}^2 + E^2}
\end{aligned} \tag{2.42}$$

It is using this model that we look to interpret our findings near the magnetic phase transitions found in $NbFe_2$.

## 2.4 Thermodynamic description of pressure

Experimentally, quantum phase transitions can be reached by tuning a system with a finite temperature phase transition to the point that the transition temperature is suppressed to zero. A common tuning parameter, used extensively in this work, is the application of external pressure. The structural response of a system to pressure is described by an Equation of State (EoS), which details the relations between volume, pressure and temperature. Isothermal EoSs give the pressure-volume ($p$-$V$) relationship at constant temperature. From thermodynamic principles, we know that the energy of a system is proportional to $pV$ [29], and when maintaining a constant temperature, we arrive at the relation:

$$p = -\left(\frac{\partial \mathcal{F}}{\partial V}\right)_T \tag{2.43}$$

where $\mathcal{F}$ represents the Helmholtz free energy. We see here that a change in the volume of the system may be viewed as a change in the total available energy of the system. The general expression for the total free energy of a crystal is expressed in terms of three functions [42]:

$$\mathcal{F}(V, T) = E(V) + E_{el}(V, T) + E_{vib}(\omega, T) \tag{2.44}$$

The first term ($E(V)$) is the static contribution to the internal energy at volume $V$ at 0 K and, in most cases, is considered the dominant term [42]. The second

term, $E_{el}$, corresponds to the electronic excitation energy contribution, this is generally considered negligible when away from the melting point of the material under consideration. The final term, $E_{vib}$, represents the energy contributed by the thermal vibrations and are therefore used primarily in high temperature corrections.

The internal energy of a system may be thought of as the sum of an attractive potential, holding the atoms together, and a repulsive potential, forcing the atoms apart [42]. At $p = 0$ and $V = V_0$ these forces are in equilibrium. A system's compressibility is defined by the reduction in volume due the application of external pressure, with stiffness being the inverse of this. When presented at a constant temperature, this quality is referred to as the isothermal bulk modulus $K_T$ and is given by the expression:

$$K_T = -V\left(\frac{\partial p}{\partial V}\right) \tag{2.45}$$

If we assume $K$ to remain constant with increasing pressure this would predict a linear relation between pressure and volume. However, the elastic nature of solids and liquids means that as the volume is reduced, the strength of the inter atomic forces opposing any further compression increases. This manifests as an increase in the bulk modulus and therefore the Murnaghan EoS assumes a linear increase in $K$ with applied pressure [43]:

$$K = K_0 + pK_0' \tag{2.46}$$

in which $K_0$ represents the bulk modulus at zero pressure and $K_0'$ its first pressure derivative [44]. Integration of this linear dependence yields the Murnaghan EoS:

$$p(V) = \frac{K_0}{K_0'}\left[\left(\frac{V_0}{V}\right)^{K_0'} - 1\right] \tag{2.47}$$

where $V_0$ is the zero pressure volume. This can then be rearranged as a function of $V(P)$, generating the inverse-Murnaghan EoS:

$$V(P) = V_0\left[1 + \frac{K_0'P}{K_0}\right]^{\frac{-1}{K_0'}} \tag{2.48}$$

The Murnaghan EoS is able to reliably reproduce the bulk modulus, $K_0$, of a compound for compression of less than 10% of the $V_0$ ($V/V_0 > 0.9$) [45]. Beyond this the system requires the use of more complex models such as the Birch-Murnaghan equations of state, which utilises a truncated Taylor expansion of finite Eulerian strain to calculate higher order derivatives of $K_0$ [44]. However, given the work presented in this thesis does not exceed this limit, the simple Murnaghan EoS will suffice.

When studying a system under pressure, a common practice is to use Raman spectroscopy to identify phonon modes via their resonant frequencies. The evolution of these modes is then used to highlight pressures of interest. The Grüneisen ratio $\gamma$ is a thermodynamic parameter used to quantify the relationship between the thermal and elastic properties of a solid [46]. It is therefore often considered the measure of the change of pressure resulting from an increase in the energy density at a constant $V$:

$$\gamma = V \left( \frac{\partial P}{\partial E} \right)_V \tag{2.49}$$

More specifically, it can be used to describes the effect the volume of a system has on the internal vibrations of that system. The Grüneisen parameter of an individual vibrational mode $i$ is hence defined as the (negative) logarithmic derivative of that modes frequency $\omega_i$:

$$\gamma_i = -\frac{V}{\omega_i} \frac{\partial \omega_i}{\partial V} \tag{2.50}$$

Tracking phonon modes and calculating their Grüneisen parameters allows one to build a picture of which bonds are changing in length at the fastest rate, offering an indication to how the atomic positions are shifting and, in turn, developing an understanding of the inter atomic forces in play.

# Chapter 3

# Experimental Techniques

The ability to tune a materials physical properties is, in many ways, the central focus of all condensed matter physics. The work presented in this thesis utilises temperature, pressure and chemical composition to drive the systems into novel phases, through a verity of means. These phases are then explored using a range of spectroscopy, scattering and diffraction techniques, employing thermal neutron and photons, ranging in energy from the far infra red in to the X-ray spectrum. This chapters focus will be the specificities of the techniques used in generating the phases under investigation, as well as the methods used to measure them and the processes used in the analysis of the resulting data.

## 3.1 The Diamond Anvil Cell

The first diamond anvil cell (DAC) was engineered in 1905, its development driven by Bridgman, with the aim of producing a more stable high pressure environment in which to conduct bulk property measurements [47]. Years later (1950s) two separate research groups, studying high pressure X-ray diffraction and infra-red absorption, adapted the cells to include diamond anvils, acting as windows into the sample chamber [48] [49]. Since then, little has changed in the design of the basic cell.

Conceptually a simple device, a DAC contains two opposing diamonds, aligned

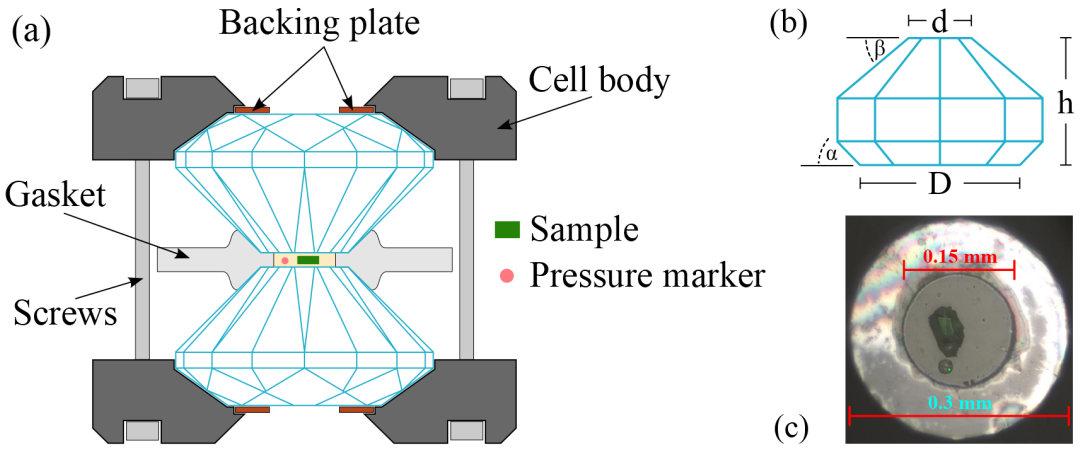


**Figure 3.1:** (a) Schematic of a diamond anvil cell depicting its fundamental elements; diamonds, gasket, backing plate, cell body, pressure marker and sample. (b) Modified Drukker Dubbledee cut diamond. Angles $\alpha$ and $\beta$ are used to define the overall height $h$, as well as the culet diameter $d$. The culet size then dictates the maximum pressure attainable by the cell, ranging between $d = 0.05$ mm for pressures of several hundred GPa to $d = 0.9$ mm and pressures less than 5 GPa. (c) A single crystal sample ($Cu_2OSeO_3$) loaded alongside a ruby sphere pressure marker and KBr as the pressure transmitting medium inside a diamond anvil cell. The sample dimension is $\approx 50{\times}75{\times}30$ $\mu m^3$ in size and the sample chamber about 45 $\mu$m deep.

point to point, separated by a thin metallic sheet and held within a mechanical vice, shown in figure 3.1a. The sample is placed between the diamonds, suspended in a pressure transmitting medium, held within a small chamber drilled into the gasket. Tightening the vice then drives the diamonds together, generating pressure and compressing the sample. Given that pressure is defined as force $F$ per area $A$, a relatively small amount of force is required to generate very large pressures. Considering diamonds with 300 $\mu$m culets, $d$ as shown in figure 3.1.b, around 2 kN of force will generate ~30 GPa of pressure.

Diamond is chosen as the anvil material because it possesses a number of qualities that make it ideally suited for the job. Diamond is naturally one of the hardest materials on earth, with a bulk modulus of 443 GPa, exhibits excellent transparency to the electromagnetic spectrum, is highly stable over a wide range of temperatures and also chemically inert below 300 K [50]. Initially, researchers

used standard brilliant cut diamonds purchased directly from jewellers, however, as the field grew the Drukker Dubbledee cut was developed [51], see figure 3.1.b. This design maximises the belt and table section, increasing stability and providing a better table to culet ratio. The diamonds for use in spectroscopy and diffraction measurements are chosen to be of the highest quality; any inclusions within the gem may alter results or become stress points under extreme pressures. Scientific diamonds are also classified according to their nitrogen content, as nitrogen absorbs in the IR region and may obscure results. Diamonds of type Ia contain up to 0.3% nitrogen, type Ib up to 0.05% nitrogen, while type IIa contain so little nitrogen it becomes no longer detectable in IR or UV absorption spectra. becoming a $p$-type semiconductor [50].

When assembling the DAC, it is vital that the diamonds are correctly aligned. The opposing culets must sit as close to parallel as is physically achievable and coincide exactly. Any misalignment will create stress points when the cell is pressurised and risks damaging or destroying the diamonds. In order to check alignment, the diamond anvils are very gradually brought together, without a gasket. If the culets are not parallel, a rainbow pattern (Newtons rings) emanating from the culet edges in contact will appear. When observed through a microscope, this phenomenon is easily observable. The diamonds are then separated, their tilt adjusted and alignment checked again. Once the anvils are positioned correctly, the mechanical stability of the alignment is checked through a series of pressure tests. For this, a blank gasket (a 300 $\mu$m thin metallic foil, typically made of steel, Rhenium (Re) or Tungsten (W)) is placed between the diamonds and the pressure is increased, released and the culet alignment checked. This is repeated several times and, so long as the alignment remains stable, the preparation of the cell may progress.

A hydrostatic pressure environment is highly desirable, as this ensures that all stresses are applied to the sample uniformly. Non-hydrostatic environments may cause changes to the system due to sheering or torsion forces acting on the atomic bonds, rather than purely pressure. In order to create a hydrostatic

pressure environment the sample is placed into a chamber drilled into the gasket, along with a pressure transmitting medium (PTM) and pressure marker.

The sample chamber is created by loading a blank gasket between the diamonds and indenting to a thickness of $\sim$45 $\mu$m. The chamber is then drilled in the centre of this indent, usually with spark erosion but also through laser ablation or via a micro drill depending on the size of the hole required. Care must be taken that no burrs or blemishes are left on the walls of the chamber, as at high pressure these become stress points that may lead to cell failure. As well as housing the sample chamber the gasket serves to improve the safety of the diamonds, preventing them from coming into direct contact with one another and providing a stabilising ring of excess material around the edge of the indent, see 3.1.a.

The sample chamber is then loaded with the PTM, that serves to transform the uniaxial pressure created by the diamonds into a hydrostatic pressure, compressing the sample uniformly in every direction. There are many different PTMs used in the high pressure community, existing as solids, liquids or gasses at ambient conditions and each operating with specific working limits. As such, the choice of PTM often depends on the maximum pressure intentions of the experiment and any interference that may be caused by the PTM e.g. overlapping Raman bands, absorption regions, additional diffraction peaks or increased background signal, see table 3.1.

The most hydrostatic pressure environments are created using gaseous PTMs (He, Ne), however require the use of specialist gas loading systems. To perform such loading, a partially open DAC is mounted into a pressure vessel, which is then filled with the chosen gas via a number of automated hydraulic pistons. Once at the desired pressure, typically around 1.5 kbar, the DAC is closed. Throughout this process, the sample chamber is observed via an in-line camera system, situated behind a sapphire window located in the base of the vessel. At lower pressures, gaseous PTMs are still highly compressible, the implication of this being that the sample chamber may shrink by up to 75% as the pressure is increased.

**Table 3.1:** Various pressure transmitting media used in this thesis. $P_f$ indicates freezing pressure and $P_h$ indicates the hydrostatic limit.

| Medium | $P_f$ (GPa) | $P_h$ (GPa) |
|---|---|---|
| Meth:Eth[a] (4:1) | 10.4 | ∼20 |
| He[b] | 11.8 | >60 |
| Ne[b] | 4.7 | 16 |
| KBr | | 2 |

[a]Mixture of Methanol and Ethanol in a ratio of 4:1.

[b]Cryogenic or gas loading, requiring specialist equipment.

It is therefore important that the sample chamber is large enough initially that even with this reduction in volume, the sample dose not bridge the chamber walls.

Once a cell is closed there must still be a means of accurately determining the pressure within the sample space. When DACs were first developed, pressure was established via measuring the specific volume of a metallic marker (usually Cu, Mo, Pd or Ag) placed in the sample chamber and calculating the absolute pressure through the isothermal EoS for these metals [52]. This method, however, is extremely prohibitive, given the requirement of a dedicated X-ray diffraction measurement at each pressure. This subsequently lead to the development of the ruby florescence technique. When excited by laser light, ruby ($Al_2O_3$ doped with 0.5% Cr) exhibits two very strong luminescence doublets ($R_1$ and $R_2$ lines). As pressure is increased, the wavelength $\lambda$ of this luminescence shift, as seen in figure 3.2. The pressure dependence of this shift was calibrated against the compression of NaCl up to a pressure of 195 kbar [53], establishing the following dependence:

$$P = \frac{A}{B}\left[\left(1 + \frac{\Delta\lambda}{\lambda_0}\right)^B - 1\right] \tag{3.1}$$

Here $A = 1904$ GPa and $B$ represents an empirically determined constant taken as 7.665 in the quasi-hydrostatic case and 5 for the non-hydrostatic case. The sift of the ruby line $\Delta\lambda$ is with respect to its position $\lambda_0 = 694.33$ nm at ambient pressure. The pressure dependence of the $R_1$ line in ruby is now well established

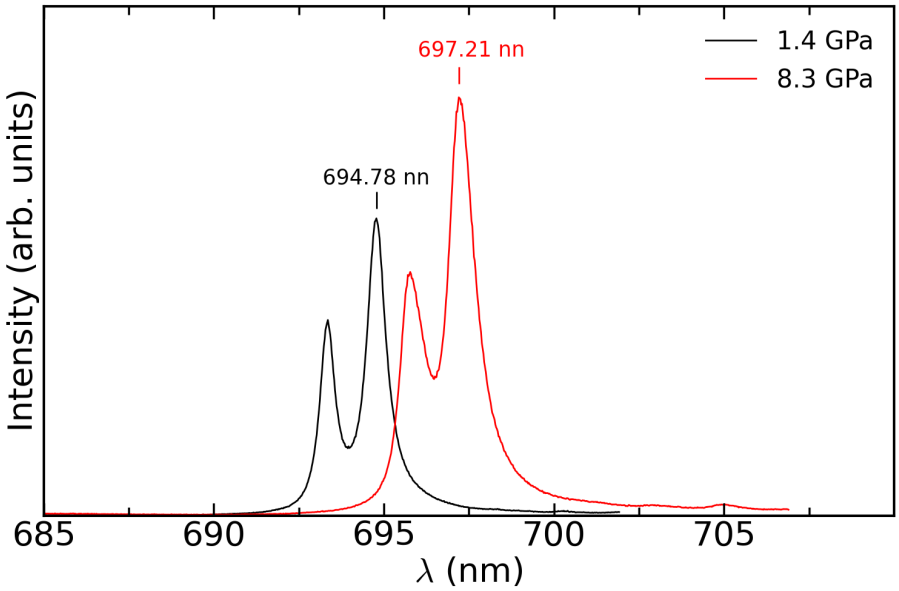


**Figure 3.2:** Ruby fluorescence lines $R_1$ and $R_2$ at two different pressures. Using the shift of the $R_1$ line with respect to its ambient pressure value the pressure can be estimated via eq.3.1.

up to 150 GPa [54][55].

The diamonds, gasket, PTM and pressure marker are all housed within the cell body. Through the years, various different DACs have been developed and adapted, each to match specific experimental needs [56]. The plate DAC, shown in figure 3.3.a, is the simplest form of a DAC; comprising two opposing steel plates, separated by three precisely machined pillars and held together by three screws. To drive the diamonds together, these screws are tightened using a gearbox that ensures each screw is turned by the same amount, generating pressure while maintaining alignment. Plate cells are often used when the experiment requires the use of a microscope, given their minimal height. Their simplicity also results in a relatively easy sample loading process, given excellent access to both diamonds.

A DAC that utilises a lever arm system to drive the diamonds together [58] is depicted in figure 3.3.b. One diamond is aligned in the centre of a piston which is gently pushed into the cell body. The two arms are placed over the piston, using a specialised gearbox attached to two lead screws, both arms are then drawn outwards, leading to them pushing the piston into the cell body, generating

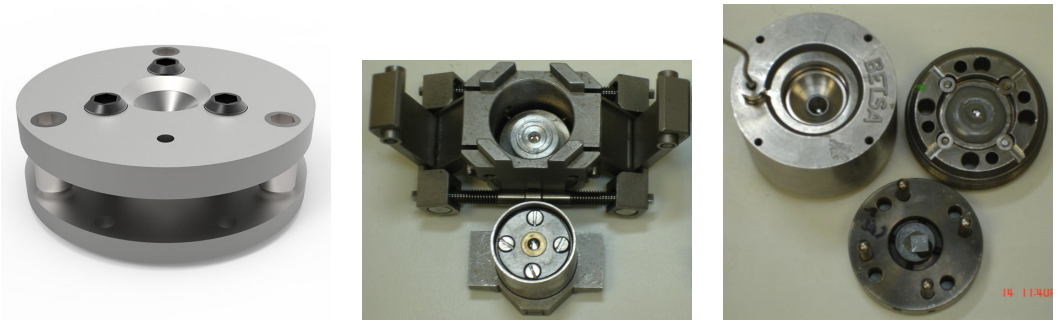

(a) (b) (c)

**Figure 3.3:** (a) For the plate DAC pressure is generated via tightening three screw using a separate gearbox [57]. (b) A leaver-arm DAC uses a lever mechanism driven by a gearbox attached to two lead screws; this design minimises the mechanical stress on the lead screws as the applied force is amplified by the lever mechanism [58]. (c) The membrane DAC uses gas pressure inside a membrane to exert force on he anvils [57].

pressure between the two diamonds. This design minimises the mechanical stress on the lead screws as the applied force is amplified by the lever mechanism. The cell is often used in low temperature or Raman experiments given its relatively compact size. The piston-cylinder design however limits access to the diamond in the cylinder which can impede the loading process.

The membrane DAC, figure 3.3.c, utilises an expandable metallic ring membrane. The membrane is inflated with gas (with pressures up to 300 bar), driving the diamonds together. This DAC requires additional specialist equipment to operate, but allows for highly accurate adjustments in pressure given the pressure in the membrane may be adjusted very precisely. The loading of a membrane cell is similar to that of a plate cell, however, given the extra equipment required to operate (capillaries attached to a gas cylinder and pressure controller), it is best suited to experiments where the cell need not be moved.

## 3.2 X-ray Sources

X-rays serve a wide range of scientific, medical and industrial needs, making the ability to produce them in a stable and reliable fashion a necessity. All

X-ray sources operate on the same principle: a charged particle accelerating or decelerating through a magnetic field will emit electromagnetic radiation [59], this is known as Bremsstrahlung. When that charged particle has sufficient energy, the spectrum of electromagnetic radiation emitted reaches into the X-ray region. In order to achieve this on a laboratory scale, electrons are produced via thermal emission from a cathode, accelerated by a high voltage and collided with an anode made of a heavy metal material (with high atomic number $Z$) [24]. When these high energy electrons collide with the atoms in the anode, their trajectories are altered via the fields created by the atomic electron cloud, resulting in a loss of kinetic energy and leading to the emission of Bremsstrahlung. The majority of electrons colliding with the target will lose their energy over a number of collisions, producing a continuous spectrum of X-rays, shown in figure 3.4.a. The maximum energy of an X-ray created in this fashion is given by:

$$E_{max} = h\nu_{max} = hc/\lambda_{min} = eV_{max} \tag{3.2}$$

$$V_{max} = \frac{12.398}{\lambda_{min}} \tag{3.3}$$

where $h$ is Planck's constant, $\nu_{max}$ is the photon frequency, $e$ is the charge of the electron, $\lambda_{min}$ (Å) the wavelength of the photon and $V_{max}$ (kV) the accelerating potential. The minimum X-ray wavelength obtainable via this process is thus limited by the initial accelerating voltage. With each collision, the probability of the electron converting all its remaining energy into radiation is very low. As a result of this the emission spectrum produces maximum intensity at $\lambda \approx 1.5 \times \lambda_{min}$, see figure 3.4.b.

When the energy of the electron striking the target exceeds certain thresholds, discontinuous sharp lines appear on top of the Bremsstrahlung spectrum. These correspond directly to ionisation energies of the target material. Upon collision, electrons with high enough energy are capable of ejecting electrons from the inner atomic shells of the anode material. This allows electrons sitting at higher energy levels to drop down and fill the vacancy, emitting a characteristic X-ray photon in the process. These emissions are labelled the K, L and M lines, referring to

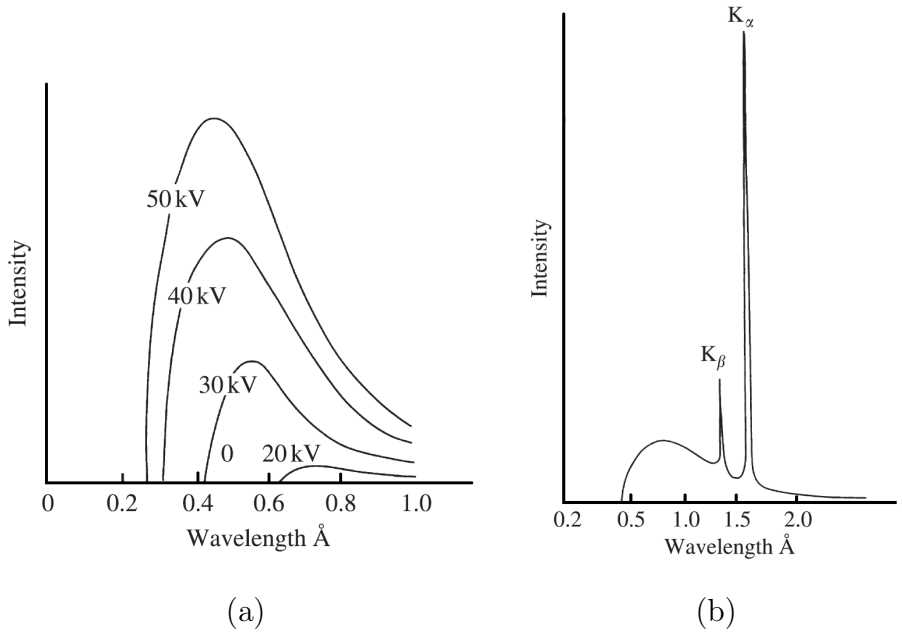


**Figure 3.4:** *(a)* X-ray radiation spectrum as a function of the accelerating voltage. *(b)* Characteristic emission spectrum of Cu [24].

the process of higher-energy electrons relaxing to fill vacancies in the K, L and M orbitals [24]. When the two orbitals involved in the emission are adjacent to one another the line is called an $\alpha$ line, while if they are separated by another shell they are called $\beta$ lines. Although all elements have characteristic emission lines, the two most frequently used by standard laboratory sources are the copper $K_\alpha$ line, $\lambda = 1.5418$ Å, and the molybdenum $K_\alpha$ line, $\lambda = 0.7107$ Å.

An alternative method for the generation of X-rays is employed at synchrotron facilities. These dedicated research sites accelerate charged particles to relativistic speeds, before utilising a combination of bending magnets and insertion devices to decelerate the particles and produce X-rays. The "zeroth" generation of synchrotrons were originally built for high energy physics research, taking the form of particle colliders. Before long, researchers at these facilities found that the light generated as a by-product of the particle acceleration could be utilised in separate experiments. Following this they quickly developed secondary projects, operating simultaneously to their main research.

Eventually, first generation synchrotron facilities were upgraded to include a

high energy storage ring, designed to provided a continuous, stable source of high energy radiation. The growth in demand for synchrotron radiation (SR), following this upgrade, prompted the building of second generation sources, facilities dedicated solely to SR research [60]. These were followed shortly by third generation facilities, such as Diamond light source, which use a series of insertion devices (wigglers and undulators), built into straight segments of their storage ring, to generate X-rays $\sim 10^{13}$ times brighter than previously possible. Looking forward, fourth generation facilities such as the 'ultimate diffraction-limited storage-ring X-ray source' are seeking to exceed even this.

Figure 3.5 shows the basic elements of the synchrotron storage ring at Diamond Light Source (DLS). Electron "packages" are first produced via thermal emission from a cathode. An electron gun then delivers them to a linear accelerator (linac), where they are accelerated and injected into a "booster" synchrotron ring. Here they reach relativistic speeds with their precise energy dependent on the facility; Diamond Light Source operates at 3 GeV. Once at the appropriate speed, the electron packages are passed into the storage ring, where series of bending magnets keeps them on track. These storage rings are kept under extremely high vacuum in order to minimise degradation of the electron current (typically 300 mA at DLS) through collision with residual molecules. Even then, this is not a perfect system, DLS for example has a current degradation of around 2% over 10 minutes and hence additional electrons are injected every 10 minutes. Operating in this "top-up" mode, synchrotrons are able to constantly generate X-rays for extended periods of time, with a beam cycle typically lasting several days.

Beginning with second and third generation facilities, insertion devices (IDs), known as wigglers and undulators, were introduced to produce radiation with characteristics different to bending magnets. These IDs consist of a series of periodically spaced magnets with alternating polarity and are built into straight sections of the storage ring. As electrons travel through such devises, the magnetic field exerted on them (Lorentz force) forces them to "wiggle" in the plane

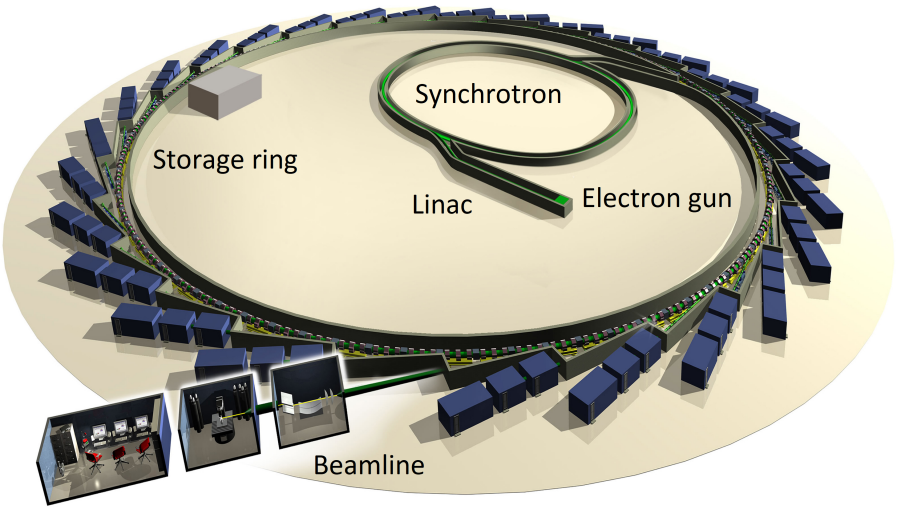


**Figure 3.5:** Schematic of Diamond Light Source, showing the key components of a synchrotron facility [61].

of their orbit. This accelerated motion leads to the emission of X-rays. Wigglers and undulators serve distinct purposes. Wigglers have an emission spectrum qualitatively very similar to Bremsstrahlung, however show an intensity increase proportional to the number of magnets in the array. Undulators on the other hand utilise interference between emissions from the same electron at different points along its sinusoidal path, to create a series of sharp emission peaks. Insertion devices are therefore used by beamlines to tailor the radiation produced, increasing flux and optimising specific spectral ranges as required.

## 3.3 X-ray Diffraction Beamlines

Once generated, X-rays must be guided to the sample and the diffracted X-rays collected for analysis. This all takes place in the instrumentation comprising a beamline. The results presented in this thesis were taken on the I15, I19 and B22 beamlines at Diamond Light Source, as well as the laboratory based Xcalibur diffractometer at Royal Holloway. Given my affiliation with I15, I will use this beamline to exemplify the beam conditioning and diffraction process.

Before reaching the sample, X-rays are first passed into the optics hutch where the beam is conditioned for use. I15 uses a wiggler to produce its X-rays, meaning

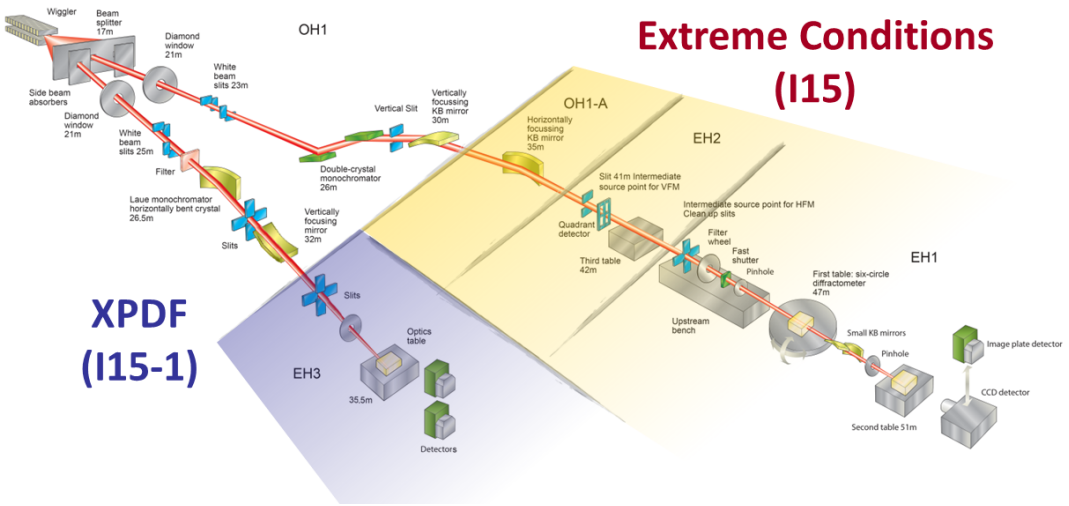


**Figure 3.6:** I15, depicted schematically, specialises in exposing samples to extream conditions whilst performing diffraction measuements, namely; cryo-cooling, laser heating and very high pressures. I15 primarilly performs powder diffraction measuremnts, but is capable of single crystal diffraction if required by the user [58].

initially it receives a wide spectrum of polychromatic radiation. For both powder and single crystal diffraction the incident beam should be as monochromatic as possible. I15 achieves this through the use of a double crystal monochromator (DCM), made up of two cryogenically cooled Si single crystals [58]. The desired wavelength is then selected by setting the angle of the Si(111) crystal according to Bragg's equation. Double-crystal monochromators diffract the incident beam twice, using two similar crystals, and are hence able to yield extremely narrow bandwidths (on the order of $\Delta\lambda/\lambda \approx 10^{-4}$). When monochromators are incorporated into conventional laboratory based generators, they are even capable of resolving $K_\alpha$ characteristic emissions into their constituent $K_{\alpha 1}$ and $K_{\alpha 2}$ doublets.

From here, the now monochromatic beam is focused on the sample position via a pair of 1 m long horizontal and vertical bendable mirrors, each made of single crystal Si. Keeping the angle of tilt below a critical angle (of the order of one milli-radian) allows for total external reflection of the beam. This critical angle is proportional to the wavelength of the X-rays and also depends on $Z/A$, the

ratio of atomic number and atomic weight of the reflecting material. By bending the mirrors to an elliptical shape, the image of the X-rays leaving the wiggler is focussed (de-magnified) at the sample position, achieving a typical spot size of 120×80 $\mu$m (horizontal × vertical). Any smaller sizes are produced by collimating the X-rays via a pinhole, collimation also serves to reduce angular divergence of the beam. The pinhole itself is an assembly of tungsten disks, each 200 $\mu$m thick, with a 20 - 80 $\mu$m hole drilled in their centres, these may be changed so as to accommodate various sized samples.

### 3.3.1 X-ray Powder Diffraction Set-up at I15

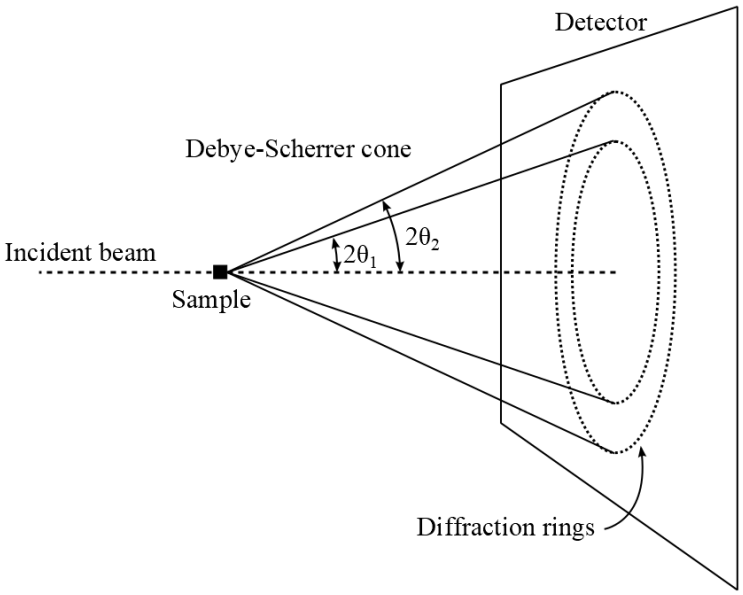


**Figure 3.7:** Schematic illustration of Debye-Scherrer cones created by powder diffraction. Each ring represents many crystals orientated so as to satisfy Braggs law for a particular $hk\ell$ plane. The intensity at each $2\theta_{hk\ell}$ is distributed over the entire ring. Integrating the intensity along the azimuth angle gives the total intensity of the peak representing that $hk\ell$ plane.

Diffraction of a powder sample may be thought of as the simultaneous diffraction of many thousands of single crystal samples, each one orientated at random with respect to the incoming beam. If every orientation is assumed to be equally

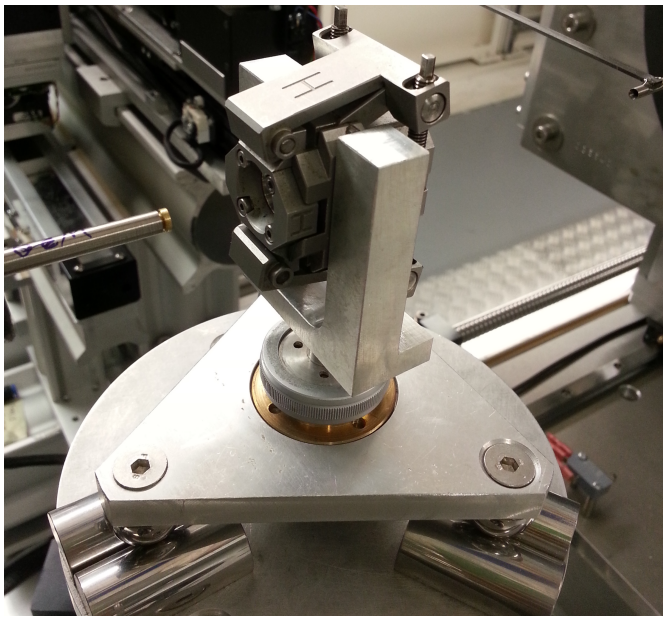

**Figure 3.8:** The sample space on the I15 beamline at Diamond Light Source. Here a leaver-arm DAC, containing the sample, is fixed in a kinematic mount, ready for exposure. The sample is often rocked around the vertical axis to ensure a good averaging of the scattered signal. A collimating pinhole and the direct beamstop in front of the detector are seen to the right and left side of the DAC, respectively.

likely, then all orientations may be considered to be present within the powder. In an ideal powder, for each $hkl$ plane, there should be present a statistically significant number of crystals orientated such that the Bragg condition is satisfied for that plane.

The projection of the diffracted beam manifests as series of diffraction cones known as Debye-Scherrer cones, see figure 3.7. On an area detector, these cones form a series of consecutive rings, centred around the axis of the beam, an example of this is shown in figure 3.7. The intensity of each $hk\ell$ plane is distributed over the entire ring, such that integrating along the azimuth angle provides the total intensity of the diffracted plane. These rings sit at a distance of $D\tan(2\theta_{hk\ell})$ from the beam centre, where $D$ is the distance between the detector and the sample and $2\theta_{hk\ell}$ is the scattering angle.

The DAC is mounted at the sample stage via a kinematic mount, designed to allow the DAC to be removed and replaced at the same position to a high level of

accuracy (several 10 $\mu$m), see figure 3.8. The stage itself is capable of rotating the sample around a vertical axis and translating it along the directions perpendicular and parallel to the incoming beam. To centre the sample in the beam, the DAC is scanned in both directions perpendicular to the beam. A diode, downstream of the DAC, is used to record the transmitted X-rays as a function of the DACs position. Once the sample is centred with respect to the X-ray beam it is rotated about the vertical axis, to check if it is located at the centre of rotation. If this is not the case a routine is used to correct for any mismatch.

I15 has a number of detectors, although only two area detectors were used in this thesis: a MAR345 image plate, and a Perkin Elmer flat panel detector.

**The MAR345** is capable of absorbing X-rays from a large energy range, 5 keV to 100 keV [62]. The detector has a pixel size of 100×100 $\mu$m, with a diameter of 345 mm and a total cycle time of around 80 seconds, depending on the scan type. Image plate scanner are virtually noiseless, meaning they are still able to detect very weak X-ray signals. The image plate itself contains a photo-stimulated phosphor, typically BaF(Br,I):$Eu^{2+}$. This compound is able to store X-rays by pumping electrons from the valence into the conduction band, where they can stay over longer periods of time. Later, when stimulated by laser light ($\lambda$ = 630 nm), the trapped electrons return to their ground state, emitting a photon of $\lambda$ = 390 nm. These photons are counted by a photomultiplier and have an intensity proportional to the previously absorbed X-rays.

**The Perkin Elmer - XRD 1621** is a flat panel detector based on an amorphous silicon sensor operating as a two-dimensional photodiode array [63]. The detector is designed to capture X-rays with energies above 40 keV, with a 2048×2048 square array of 200×200 $\mu$m pixels, capable of capturing up to 15 frames per second. X-rays are converted into visible light using a CsI scintillator. The light is then absorbed via the photodiodes and converted into an electrical current. The resulting current produces an electrical pulse which is then analysed and interpreted [64].

Before a diffraction experiment is started, the detector geometry must first

be calibrated. For this purpose a well defined sample, typically Si, $LaB_6$ or $CeO_2$ from the National Institute of Standards and Technology [65], is exposed and the diffraction pattern captured, see figure 3.10. The result is then analysed using the Fit2D software package [66] (although more recently I15 has moved to the DAWN package [67]). Fit2D uses the shape, spacing and intensities of the resulting diffraction rings to determine parameters such as detector tilt (rotation), beam centring and sample-detector distance. The software then reduces the 2D diffraction patterns into 1D diffraction, by integrating over the entire azimuth angle as a function of $2\theta$. It is important to mask any single crystal peaks observed in the diffraction patterns, often arising from the diamonds but also as a result of poorly ground powder and other impurities in the beam.

### 3.3.2 I19 at Diamond Light Source

I19 uses an undulator to generate X-rays, with energies ranging between 5 keV and 25 keV ($\lambda$ = 2.5 Åto 0.5 Å) [68]. The desired wavelength is selected using a cryo-cooled double-crystal monochromator (DCM) which is currently equipped with a Si-111 crystal. The beam is then focused, via a pair of bimorph mirrors, to a 2 mm diameter at the sample position. Results presented in this thesis used an energy corresponding to the Zr K-edge ($E$ = 17.998 keV, $\lambda$ = 0.6889 Å). I19 uses a Rigaku Saturn 724 CCD detector [68] in combination with a 4-axis goniometer capable of rotating through nearly every possible angle. The sample was mounted into a plate DAC, see figure 3.3, designed specifically to maximise the apertures of the cell and increase access to available diffraction angles, although some positions are still masked by the cell body.

### 3.3.3 Xcalibur X-ray Diffraction system

A number of single-crystal diffraction experiments were performed at Royal Holloway, all at ambient pressure. The Royal Holloway physics department is in possession of an Xcalibur X-ray Diffraction system, pictured in figure 3.9. X-rays are generated using a molybdenum source, these are then monochromated and

**Figure 3.9:** Xcalibur single crystal diffractometer at Royal Holloway

passed through a collimator so as to select a single wavelength of 0.709 Å. X-rays are then diffracted in transmission through the sample and collected by a CCD camera, following the same principles for conversion into visible light as are described for the detectors above. The system is designed to accept samples between 0.1 and 0.5 mm in thickness. The sample is placed on a 4-axis goniometer capable of rotating through nearly every possible angle, enabling the capture of the accessible reciprocal space. The CrysAlis$^{Pro}$ software paired with the system allows for almost complete automation of the measurement process, and includes a powerful analysis software package, CrysAlis$^{Pro}$.

### 3.3.4 Refinement of powder and single-crystal diffraction data

The single crystal diffraction data was collected using the CrysAlis$^{Pro}$ software sweet [69]. This software controls all aspects of the measurement, including exposure times, absorption corrections due to sample geometry and sample orientation. As each exposure is performed, CrysAlis$^{Pro}$ records the orientation of the crystal, with respect to the incident beam and detector. The sample is rotated through real space in order to access as many $(hk\ell)$ planes as possible,

see section 2.1.1. Once measurements are complete, each exposure is analysed, and diffraction peaks identified. CrysAlis$^{Pro}$ then builds a 3D map of reciprocal space, occupying it with diffraction peaks. Although this software does offer some basic symmetry analysis, for full analysis the diffraction data is imported into a crystallographic refinement software, in this case Jana2006 [70].

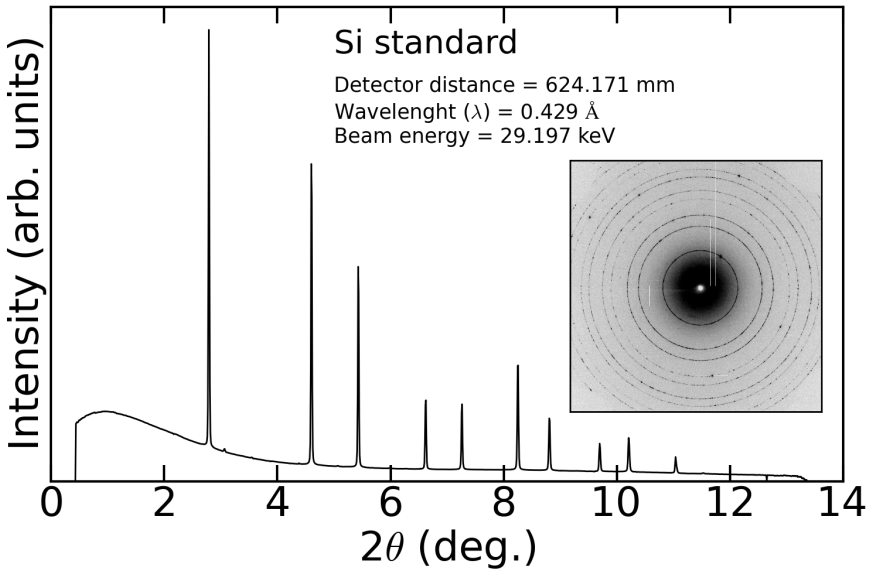


**Figure 3.10:** Integrated intensity vs. $2\theta$ pattern of a Si calibration sample. Refinement of the pattern has determined $\lambda = 0.429$ Å, with a sample to detector distance of 624.171 mm. The inset shows the Si powder diffraction detector image of the pattern presented, as captured with the Mar 345 image plate detector on the I15 beam line.

The powder diffraction patterns presented in this thesis were analysed using the Topas refinement package [71]. In this work a Le Bail type refinement was used, requiring the user to know the space group and approximate lattice parameters. A theoretical diffraction pattern is then calculated with the addition of an $n^{th}$ order polynomial (background) when required. Theoretical diffraction peaks are modelled using a pseudo-Voigt peak function [72], which is a convolution of a Gaussian and a Lorentzian distribution:

$$f_{pV}(x) = (1 - \eta) f_G(x; \gamma_G) + \eta f_L(x; \gamma_L) \tag{3.4}$$

where $f_G(x; \gamma_G)$ and $f_L(x; \gamma_L)$ are the normalised Gaussian and Lorentzian func-

tions, with FWHM $\Gamma = 2(ln2)^{1/2}\gamma_G = 2\gamma_L$,

$$f_G(x;\gamma_G) = (1/\pi^{1/2}\gamma_G)exp(-x^2/\gamma_G^2) \tag{3.5}$$

and

$$f_L(x;\gamma_L) = (1/\pi\gamma)(1 + x^2/\gamma_L^2)^{-1} \tag{3.6}$$

and $\eta$ is a parameter which mixes the two functions [72].

Topas then determines the difference between the calculated and measured pattern and employs a least squared fitting algorithm, adjusting the lattice parameters to minimise the differences between the two. This refinement process looks to minimise the quantity:

$$S_y = \sum w_i(y_i - y_{ci})^2 \tag{3.7}$$

Here $y_i$ and $y_{ci}$ are the measured and calculated intensities at the $i^{th}$ $2\theta$ position respectively, and $w_i$ is a weighted factor equal to $1/y_i$. The overall goodness of fit of the refinement is calculated, giving the weighted profile factor $R_{wp}$, by the following equation:

$$R_{wp} = \left(\frac{\sum_i w_i(y_i - y_{ci})^2}{\sum_i w_i y_i^2}\right)^{\frac{1}{2}} \tag{3.8}$$

The goodness of fit and the interpretation of the $R_{wp}$ value is often limited by the background present in the diffraction pattern.

Given pressure cells inherently produce data with a higher level of background, the Bragg or intensity $R$-factor is a better indicator as it provides a measure of agreement between the intensities calculated by the model and those observed in the measurement. The Bragg $R$-factor is given by [71]:

$$R_{Bragg} = \frac{\sum_i |I^i_{obs} - I^i_{calc}|}{\sum_i |I^i_{obs}|} \tag{3.9}$$

where $I_{obs}$ and $I_{calc}$ are the $2\theta$ positions of the $i^{th}$ peak of the observed and calculated patterns. The $R_{Bragg}$ goodness of fit hence relies only on the position of the peaks rather than their profiles.

## 3.4 Light Scattering

There are many ways in which the interactions between matter and the electromagnetic spectrum may inform us about the inner workings of a material. Minute changes in the wavelengths of scattered photons allow us to build a picture of inter-atomic structures and vibrations, while the absorption of specific energies can reveal details regarding the chemical composition of substances. This section will provide an overview of two such techniques, used in this thesis, namely Raman and Infrared (IR) spectroscopy.

### 3.4.1 Raman Spectroscopy

Raman spectroscopy utilises slight shifts detected in the wavelength of a scattered photon, to probe the inter-atomic vibrations (phonons) of a system. These subtle changes are often indicative of far more complex transition in the structural, electrical or magnetic state of the compound, making Raman spectroscopy ideal for preliminary investigations. The measurement process itself is non-destructive to the sample and requires no specialised mounting or sample preparation, while the systems are relatively cheap and have very low running costs. This makes Raman spectroscopy an ideal first step in any structural investigation.

The principle of Raman spectroscopy is straight; positioning a molecule in an electric field $\mathbf{E}$ induces a dipole moment $\mathbf{p}$ within that molecule. The relation between this induced moment and said electric field is expressed by the power series:

$$\mathbf{p} = \alpha\mathbf{E} + \frac{1}{2}\beta\mathbf{E}^2 + \frac{1}{6}\gamma\mathbf{E}^3... \tag{3.10}$$

where $\alpha$ $\beta$ and $\gamma$ are the tensor values for polarisability, hyperpolarisability and $2^{nd}$ hyperpolarisability respectively. Given $\alpha \sim 10^{-40}$ C$\cdot$V$^{-1}$ and $\beta \sim 10^{-50}$ C$\cdot$V$^{-2}$, in practice, $\beta$ and $\gamma$ reduce by a factor of 10 billion each time and are hence usually negated [73]. This leaves the dependence of the induced moment $\mathbf{p}$ directly proportional to the electrical field:

$$\mathbf{p} = \alpha\mathbf{E} \tag{3.11}$$

The polarisability of the sample varies as inter atomic distances change due to lattice vibrations. This periodic variation may be modelled as:

$$\alpha(t) = \alpha_0 + \alpha_v \cos(2\pi v_p t) \tag{3.12}$$

where $\alpha_0$ is the polarisability in equilibrium position and $\alpha_v$ is the change in polarisability during a vibration of frequency $v$. From this equation it is clear that a phonon is only Raman active if $\alpha_v \neq 0$.

We may consider light as an oscillating electrical field, described by:

$$\mathbf{E}(t) = \mathbf{E}_0 \cos(2\pi v_\lambda t) \tag{3.13}$$

where $\mathbf{E}_0$ is the maximum field value, $v_\lambda$ the frequency of the photon and $t$ is time.

Combining these models brings us to an approximation of the induced dipole moment relative to the internal vibration and the frequency of the incident photon:

$$\mathbf{p} = \alpha_0 \mathbf{E}_0 \cos(2\pi v_\lambda t) + \alpha_v \mathbf{E}_0 \cos(2\pi v_p t) \cos(2\pi v_\lambda t) \tag{3.14}$$

which equates to:

$$\mathbf{p} = \alpha_0 \mathbf{E}_0 \cos(2\pi v_\lambda t) + \frac{1}{2}\mathbf{E}_0[\cos(2\pi(v_\lambda - v_p)t) - \cos(2\pi(v_\lambda + v_p)t)] \tag{3.15}$$

Thus, we see it is possible to split the induced dipole moment into 3 components, each with a different frequency. The first term corresponds to the elastic scattering (Rayleigh scattering ) of light, possessing the same frequency and hence the same energy as the incident photon, $v_\lambda$. The $2^{nd}$ and $3^{rd}$ terms describe the inelastic scattering of light, known as Raman Scattering. The energy gain term is known as Anti-Stokes scattering and the energy loss side as Stokes scattering. This process is depicted schematically in in figure 3.11. Given there are exponentially fewer molecules starting in the higher energy vibrational state, the intensity of anti-Stokes scattering is far less than that of Stokes scattering.

When performing a Raman measurement, an intense, monochromatic beam of electromagnetic radiation (usually a laser) is focussed on the sample. The

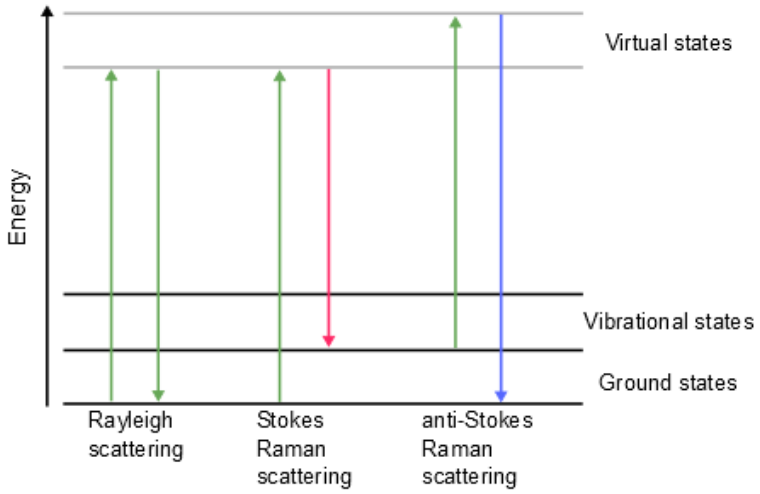


**Figure 3.11:** Schematic energy level diagram illustrating the processes that occur during Raman and Rayleigh scattering.

intensity of scattered radiation is measured as a function of wavelength, and typically presented as a function of the Raman wavenumber, $\omega$, expressed in $cm^{-1}$. This relates to the difference in frequency between scattered and incident light via the expression:

$$\omega = \frac{\nu_m}{c} - \frac{\nu_0}{c} \tag{3.16}$$

Where $\nu_m$ and $\nu_0$ are the frequencies of scattered and incident light respectively and $c$ is the speed of light [73].

The Raman spectra presented in this thesis have been measured at I15, using a LabRam HR800 spectrometer, available in one of the peripheral laboratories of the beamline [58]. In order to excite Raman-active phonons, either a 532 nm (green) or 473 nm (blue) laser is used. Spectra may be obtained above 100 $cm^{-1}$ and the spectral coverage determined by the gratings (1200 or 1800 grooves per mm) used. Results presented in this work were collected using the grating with 1200 grooves/mm and captured using a Peltier-cooled CCD, kept at an operating temperature of -70° ∼C.

A built in microscope allows the system to focus on $\mu$m scale samples, necessary for DAC experiments. For alignment, the sample is illuminated using an in-line white light, operating in both reflection and transmission and observable

via a live camera feed, used to position and focus on the sample. The sample stage itself has a full range of motion in the $x$, $y$ and $z$ axis, with a very high degree of accuracy ($\mu$m scale) so as to allow focusing on the very small samples found in DAC experiments.

### 3.4.2 Infrared Spectroscopy

Infrared (IR) spectroscopy relies on the absorption of IR radiation by matter. When the frequency of a vibrational mode matches that of the incident photon, that photon may be absorbed by the system, increasing the energy of that system. The resulting absorption lines observed in the spectra are proportional to the energy difference between the vibrational ground and excited states. For a lattice vibration to be IR "active" it must associate with a change in the dipole moment of the system.

The IR region of the electromagnetic spectrum may be broken into three parts; near infrared (NIR) contains the higher energy portion of the spectrum, $\lambda$ = 0.8 to 2.5 $\mu$m, and can be used to excite higher harmonic structural vibrations. The mid-IR range covers $\lambda$ = 2.5 to 25 $\mu$m and is used to study fundamental vibrations. Finally, far infrared (FIR) lies on the border of the microwave region, $\lambda$ = 25 to 1000 $\mu$m , and is used primarily in rotational spectroscopy.

The IR-absorption experiment were conducted at beamline B22 at DLS. B22 specialises in Infrared Micro-Spectroscopy and Infrared imaging. The IR radiation produced at B22 spans the entire IR spectral range, extending from near-IR ($\lambda$ = 700 nm - 2500 nm) up to the far-IR or THz region ($\lambda$ = 15 $\mu$m - 1 mm) and is between 100 and 1000 times brighter in the mid-far-IR region than conventional broadband IR sources [74].

Mounting a DAC onto the B22 Hyperion 3000 IR microscope requires the use of a custom plate fitted to the mapping stage. Fine alignment of the beam is optimised to the aperture of the DAC with only partial clipping by the cell, due to the limited numerical aperture of the DAC. The full synchrotron Radiation Infrared beam (at 233 mA) was delivered in standard 15× reflection and trans-

mission modes. A standard Ge coated lowpass filter limits the spectral range below 3950 $cm^{-1}$. B22 uses a Bruker Vertex 80 V FTIR detector, with a scanner velocity of 40 kHz and spectral resolution of 4 $cm^{-1}$.

## 3.5 Neutron Scattering

Thermal neutrons possess four key characteristics that make them an excellent tool for probing the many important features of matter. Their wavelength range in the order of inter-atomic distances, allowing for scattering and diffraction, while the fact they possess no charge means they scatter directly from the atomic nuclei via the nuclear force. Neutrons have a magnetic moment, meaning they interact with unpaired electrons. Elastic scattering from these magnetic ions provides information on the arrangement of electron spins and density distributions. Inelastic scattering gives the energies of the magnetic excitations. Finally, the energies of neutrons are of the order of atomic excitations, meaning that when scattered inelastically, via the creation or annihilation of an excitation, their change in energy is easily measured. This section will explore the nature of these scattering events, as well as provide an overview of the measurement process.

### 3.5.1 Neutron Sources

Neutron sources, designed specifically for research, typically operate in one of two ways, generating neutrons through spallation of heavy nuclei by accelerated particles or through fission processes confined within a nuclear reactor [24]. Reactor sources provide a constant flux of thermal neutrons, while spallation sources are used to produce bursts of neutrons, generating a beam with a time structure dependent on the frequency with which incident particles strike the target. The work of this thesis has utilised only reactor based sources.

Much like their energy providing counterparts, scientific reactors are built based on generating controlled fission reactions [75]. Neutrons are absorbed by nuclei of $^{235}U$, exciting them and causing them to fragment into nuclides of a lower

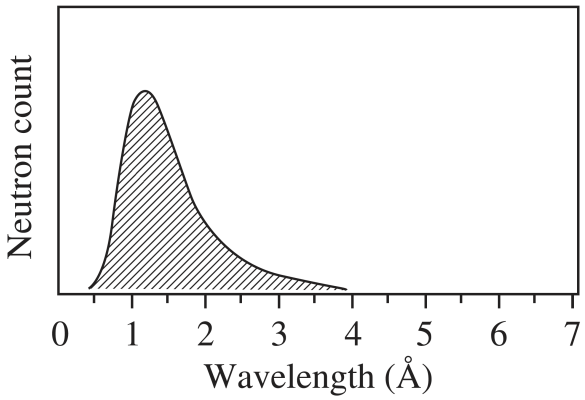


**Figure 3.12:** The Maxwellian distribution of thermal neutrons from a nuclear reactor source [24].

atomic number. This process releases, on average, ∼2.5 neutrons. Of these, 1.5 are reabsorbed by the reactor fuel, continuing the fission process, and 1 escapes, emitted with an energy of ∼2 MeV. The majority of the energy created in the fission reaction (∼200 MeV per event [75]) manifests as heat, the management of which quickly becomes the limiting factor of any reactor design. A reactor with a thermal power of 1 MW will radiate $3\times10^{16}$ neutrons/s globally; these must then be extracted from the core and guided to the instrumentation. The flux available at the sample site is hence proportional to the core's neutron density, the solid angle of extraction from the core and the efficiency of the guides' reflectivity. For example, obtaining a flux of $10^{15}$ n/cm$^2$s at the instrumentation requires a reactor with a thermal power of the order of 60 MW.

Despite their vastly inferior intensities, where neutrons excel over X-rays is in their ability to resolve excitations within a compound [75]. However, while typical excitation energies are on the order of tens of meV or less, neutrons emitted from the core have an initial energy of 2 MeV ($\lambda \approx 0.0064$ Å). Therefore neutrons must first be "cooled" before they interact with the sample. This is done through collisions with light elements, H, D or Be. Once in thermal equilibrium with these moderators the neutrons, now called thermal neutrons, take on an energy distribution described by a Maxwellian spectrum, see figure 3.12. The typical naming conventions for neutron energies are provided in table 3.2.

**Table 3.2:** Typical parameters of neutron beams [24].

| | E(meV) | $\lambda$(Å) | $\nu$(m/s) |
|---|---|---|---|
| Epithermal neutrons | 8180 | 0.1 | 39560 |
| Hot neutrons | 327 | 0.5 | 7912 |
| Thermal neutrons | 36.4 | 1.5 | 2637 |
| Cold neutrons | 0.818 | 10.0 | 396 |
| Ultra-cold neutrons | 0.00818 | 100.0 | 40 |

A modest estimate for the energy resolution of a detector would be ∼10% ($\Delta E/E$) [75]. This puts the resolution of a thermal neutrons with $E \approx$36 meV around ∼3 meV. By comparison, X-rays, with energies between 5 keV and 15 MeV, would have a maximum energy resolution around ∼500 eV. As such neutrons are often used to probe structural or magnetic (phonons and magnons) lower-energy excitations within a material.

### 3.5.2 Triple Axis Spectrometry

Much like X-rays, once generated neutrons are tailored to their specific task, guided to the sample and the scattered neutrons collected for analysis. Although the instrumentation is, necessarily, physically different, the laws informing its operation remain largely the same. This thesis presents data collected through both elastic and inelastic neutron scattering, with the use of triple-axis spectrometers at the FRM II reactor in Munich Germany [76] and the ORPHEE reactor at LLB in France [77].

Triple axis spectrometry (TAS) acquires its name from the three axes of rotation central to the process; namely the monochromator, the sample and the analyser. These are indicated in figure 3.13, along with scattering angles, $2\theta_M$ scattering from the monochromator, $2\theta_S$ scattering from the sample and $2\theta_A$ scattering from the analyser. The incident, $\mathbf{k}_i$, and final, $\mathbf{k}_f$, scattering vectors of the neutron are also shown.

Triple axis spectrometry requires a constant beam of neutrons for diffraction and hence a reactor based source. In order to attain the highest levels of neutron flux, detectors are often constructed right next to the reactor core. Where this is not an option, neutrons are guided down a beam pipe to their research station targets, much like a beam line at a synchrotron facility. However, unlike the highly collimated beam produced by synchrotrons, neutrons emerge from the reactor with a high level of angular divergence, making collimation far more important in the beam conditioning process.

Once collimated, neutrons are projected onto a single crystal monochromator (typically Cu(111), Si(111) or pyrolytic graphite (PG) (002)), where a single wavelength is selected, again utilising the diffraction angles dictated via Braggs Law. Adding curvature to monochromators allows them to also serve as focussing mirrors, the aim being to create a beam with geometry similar to the dimensions of the sample under inspection. An artefact of the energy selection process is that monochromators will also reflect neutrons of higher order wavelengths, e.g. $2\mathbf{k}_i$, $3\mathbf{k}_i$... etc. These higher order neutrons will contribute to the neutron monitor count, however are far less likely to be scattered by the sample and as such must be corrected for, either through instrumentation or in the analysis process.

Once the single energy is selected, the beam is focused on and diffracted by the sample. The sample sits on a stage mounted on a two axis goniometer, capable of rotating or tilting the sample to a very high degree of precision. The majority of facilities will also have the ability to control the sample environment, changing parameters such as temperature, pressure and magnetic field strength at the sample position.

Incident neutrons scatter from the sample position in all possible directions with a range of energies. The analyser sits at an angle $2\theta_S$, with respect to the beam incident on the sample, and selects neutrons of a specific energy, directing them towards the detector. Analysers operate under the same principles as monochromators, utilising Braggs law to select and focus specific wavelengths. For the majority of TAS experiments, $\mathbf{k}_f$ is held constant. From this, the neutron

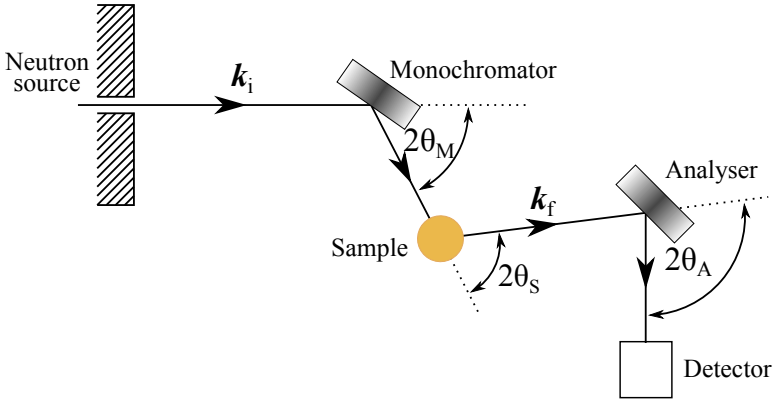


**Figure 3.13:** Schematic diagram of a triple axis spectrometer, showing the arrangement of the source, monochromator, sample, analyser and detector.

energy loss is calculated via:

$$\hbar\omega = \frac{\hbar^2(\mathbf{k}_i^2 - \mathbf{k}_f^2)}{2m_n} \tag{3.17}$$

where $m_n$ is the mass of a neutron and $\omega$ is its angular frequency.

#### 3.5.2.1 MIRA-2 - FRM II

The Forschungsneutronenquelle Heinz Maier-Leibnitz (FRM II) reactor, at the Technische Universität München (TUM), is a heavy water moderated reactor with a thermal power of 20 MW, producing a neutron flux of up to $8\times10^{14}$ neutrons $cm^{-2}s^{-1}$ [76]. The core is an aluminium - $U_3Si_2$ alloy, containing ~8.1 kg of enriched $^{235}U$ and is capable of running for 60 days at full power. The cold neutrons used by the MIRA instrument are produced via a liquid deuterium ($D_2$) moderator, kept at a temperature of ~25 K. Wavelengths are selected using a horizontal focusing highly oriented pyrolytic graphite (HOPG) monochromator, capable of selecting wavelengths between $\lambda_{min} = 3.5$ Åand $\lambda_{max} = 6$ Å. Scattered neutrons are collected via an analyser consisting of 2 cavities and a $^3$He-spin filter. MIRA-2 uses a 1 inch $^3$He finger detector. The MIRA-2 triple axes system sits on a series of motorised tables, which enables extremely fine control of the diffraction geometry and allows the system to resolve energies down to ~220 $\mu$eV,

dependent on $\mathbf{k}_i$.

For the measurements on MIRA presented in this thesis, the sample has been mounted in a dry fridge with a base temperature of ∼7.2 K [76]. The MAG-2.2T-HTS magnetic sample environment was used, capable of producing fields up to ±2.2 T, with a homogeneity range of ⊘ = 15 mm.

#### 3.5.2.2 TAS 4F2 - LLB

The ORPHEE reactor found at the Laboratoire Léon Brillouin (LLB) is a swimming pool type reactor with a thermal power of 14 MW and a flux of $3\times10^{14}$ neutrons $cm^{-2}s^{-1}$ [78]. The core is an aluminium - uranium alloy, enriched with 6 kg of $^{235}U$, which requires renewal every 100 days. The cold source, used by the 4F instrumentation, is mediated via liquid hydrogen and has a flux of $17.5\times10^{9}$ neutrons $cm^{-2}s^{-1}$, providing a flux at sample of $\sim3.5\times10^{6}$ neutrons $cm^{-2}s^{-1}$. Neutron energies are selected using a double crystal monochromator (DCM) set-up of pyrolytic graphite, capable of selecting wavelengths between $\lambda_{min}$ = 2 Å and $\lambda_{max}$ = 6 Å. Scattered neutrons are then collected via an analyser consisting of a combination of pyrolytic graphite and Ge(111). The detector is $^{3}He$ based with dimensions, ⊘ = 5 cm $h$ = 15 cm. The 4F2 triple axis system sits on a series of motorised tables, which enables extremely fine control of the diffraction geometry and allows the system to resolve energies down to ∼220 $\mu$eV, dependent on $\mathbf{k}_i$.

For the measurements at 4F2 presented in this thesis, the sample has been mounted into a $^{4}He$ cryostat with base temperature of 1.5 K [78].

# Chapter 4

# Exploration of $NbFe_2$

The $Nb_{1-x}Fe_{2+x}$ system displays a rich magnetic phase diagram over a very small doping range. What truly marks this as a system of particular interest, however, is the non-Fermi liquid like behaviour indicative of ferromagnetic quantum criticality in the region where the border of magnetism is masked by a spin density wave (SDW) phase [79, 80] (section 4.1). In Section 4.2 previous knowledge of the $Nb_{1-x}Fe_{2+x}$ system is reviewed. Section 4.3 contains the observation of the response of the SDW phase to a magnetic field. In Section 4.4 the low-energy excitation spectrum at zero field of slightly Fe-rich $Nb_{0.981}Fe_{2.019}$ is presented.

## 4.1 Instability of Ferromagnetic Quantum Critical Points and masking by modulated order

As has been mentioned in previous sections, the exploration of ferromagnetic quantum phase transitions in metals has been under close inspection in recent years, leading to a number of theoretical and experimental studies [6]. These investigations have revealed numerous examples of non-Fermi liquid states [7, 9] and unconventional superconductivity [8, 81, 82], however have not been able to answer the question: can a ferromagnetic quantum critical point exist in clean band magnets. To date, systems with the potential of possessing a FM QCP instead present one of two avoidance scenarios; the transition becomes first order

(discontinuous) in nature [83] or, the low temperature order of the system changes completely, be that to some nematic order or a long-wavelength spin density wave state [84].

Ferromagnetic quantum phase transitions have been traditionally described in terms of the generalised Landau-Ginzburg-Wilson approach of free energy functionals, it has however been found that additional non-analytical corrections are required to describe these states accurately. The intuitive interpretation of this is that fluctuations in an excitation spectrum, the disorder of a system, may stabilises phases, presenting a new order that would not be stable in their absence [85]. This mechanism is referred to as *order by disorder*. The fundamentals of this theory are that changes in the Fermi surface of a system, for example through the introduction of some order parameter, modify the electron dispersion. As a result, this reconfigures the spectrum of low-lying excitations and hence shifts the zero-point energy of the fluctuations.

A key prediction of order by disorder is the increase of the spiral ordering wavevector with temperature. This is observed clearly in PrPtAl which, rather than a simple FM-PM transition, presents three separate transitions in close proximity [86]; the first, around $\approx$5.85 $\pm$0.05 K, to a doubly modulated incommensurate spin density wave state, then to a single incommensurate modulation of different period about $\approx$ 5.5 $\pm$0.2 K and finally to uniform ferromagnetism between 5.04.3 K. This is observed in both neutron and resonant X-ray scattering results across multiple samples, with signatures of the transitions also present in thermodynamic measurement such as heat capacity and d.c. and a.c. susceptibility.

Similar to this, $Sr_3Ru_2O_7$ offers an example of a field-tunable metamagnetic quantum phase transition masked by SDW order [87]. Here the system undergoes a rapid increase in magnetisation, from 0.2 to 0.35 $\mu_B Ru^{-1}$, near the metamagnetic field, $B_C \approx 7.95$ T, which, however, is masked by a 1 T region of two distinct SDW phases. The relatively small field range in which this ordered state exists suggests that their origin is due to a new mechanism related to the details of the

electronic structure near the Fermi energy, possibly combined with the stabilising effect of magnetic fluctuations.

$Nb_{1-x}Fe_{2+x}$ presents as an ideal candidate for the investigation of the SDW scenario in a clean itinerant system, due to the presence of a ferromagnetic phase transition extrapolating to zero temperature at zero field.. This allows for a multi-probe approach, with particular attention paid to neutron scattering [39].

## 4.2 Properties of $Nb_{1-x}Fe_{2+x}$

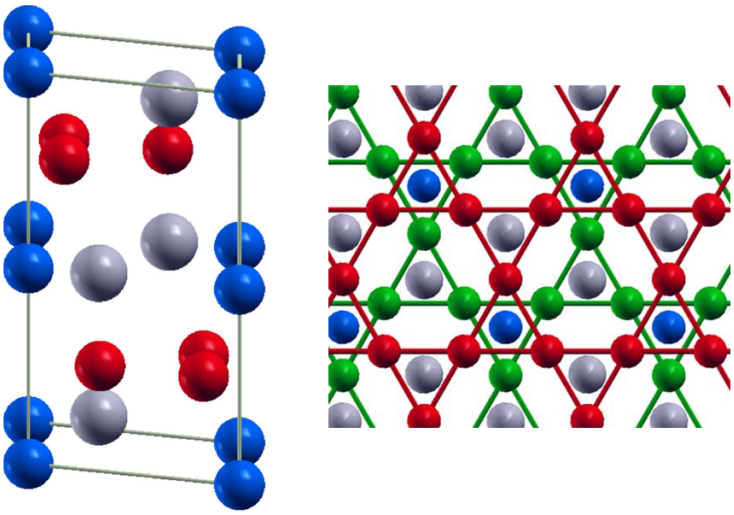

**Figure 4.1:** *(left)* Crystal structure of NbFe2 with sites Fe($6h$) red, Fe($2a$) blue, and Nb($4f$) gray. *(right)* View along the $c$ axis. The upper and lower kagome layers formed by the Fe($6h$) sites are separated into red and green, respectively. Red Fe($6h$) shows upper kagome, green Fe($6h$) shows the lower kagome, while Fe($2a$) sites are blue and Nb($4f$) sites are grey. Images taken from [88]

$NbFe_2$ crystallises in the hexagonal C14 Laves phase, space group $P6_3/mmc$, see figure 4.1. The unit cell consists of 4 formula units, 8 Fe atoms and 4 Nb atoms. Within the unit cell, the Fe atoms occupy two distinct sites, $2a(0,\ 0,\ 0)$ and $6h(y,\ 2y,\ \frac{3}{4})$. Together, these form a layered structure consisting of a kagome lattice (Fe($6h$)), separated by Fe($2a$) atoms centred on the line drawn between alternate kagome triangles [89]. The Fe atoms situated at these two distinct sites may, in principle, host two different magnetic moments. Nb atoms occupy the

interstices in the Fe structure at the $4f(\frac{1}{3}, \frac{2}{3}, x)$ site, lying slightly out of plane with respect to the Fe($2a$) atoms, and are hence considered to lie within Fe cages. Amongst Fe sites, nearest neighbour distances between Fe($2a$) and Fe($6h$) sites are similar, Fe($2a$)-Fe($6h$) = 2.42 Å, Fe($6h$)-Fe($6h$) = 2.37 Å, meaning that, when doping, the dopant site is likely determined by the bonding network of Fe cages rather than the volume available at the site [88].

$Nb_{1-x}Fe_{2+x}$ is metallic, with its electronic properties governed by the $3d$ orbitals of Fe and $4d$ orbitals of the Nb atoms [90]. Experimentally, at low temperatures, $Nb_{1-x}Fe_{2+x}$ reveals a rich phase diagram across a narrow range of compositions, $x$ = -0.06 to 0.04 [80, 91, 92], shown in figure 4.2. The high temperature PM phase is characterised by a clear Curie-Weiss behaviour in the inverse susceptibility [93]. Further susceptibility measurements point towards this being an easy $c$ axis system [94].

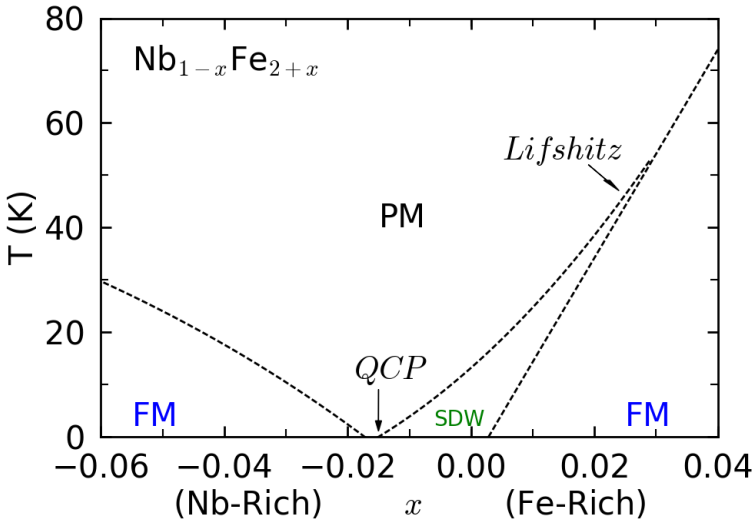


**Figure 4.2:** Temperature vs doping phase diagram of $Nb_{1-x}Fe_{2+x}$ , adapted from [12].

The Fe-rich compositions at $x = 0.04$ is found to exhibit remanent magnetisation below the Curie temperature $T_C \approx 70$ K and is thus labelled ferromagnetic [92]. This transition is also seen as a kink in the resistivity temperature dependence $T_\rho$ [80], see figure 4.3. At lower temperatures, hysteresis loops are observed in the $M(H)$ curves. As $x$ decreases so too does $T_C$, being suppressed to zero

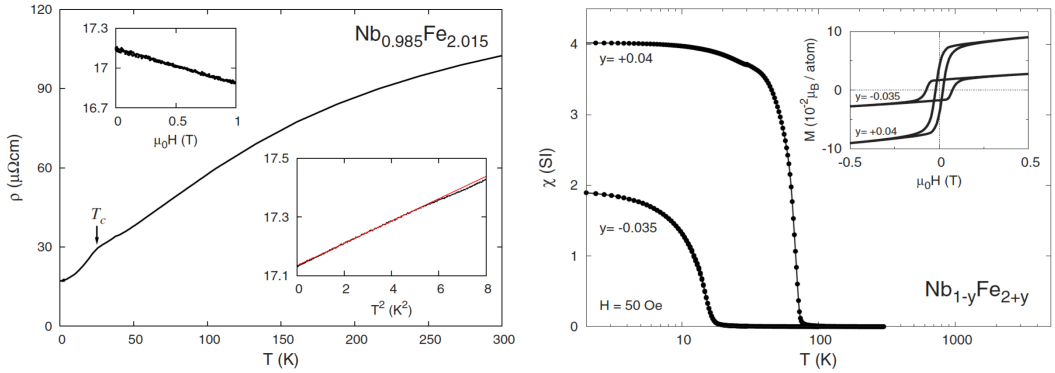


**Figure 4.3:** (*left*) Resistivity $\rho$ of $Nb_{1-x}Fe_{2+x}$ with $x = 0.015$. Clearly visible is the FM transition temperature at $T_C = 25$ K. At this point the $\rho$ is seen to follow a $T^{\frac{5}{3}}$ law, shown in lower inset. The magnetoresistance is almost flat at 100 mK, upper inset. (*right*) Temperature dependence of dc magnetic susceptibility for $Nb_{1-x}Fe_{2+x}$ samples with $x = 0.04$ and $x = -0.035$. Results are taken from [91].

temperature near stoichiometry [92].

At the border of FM, evidence for a further magnetically ordered phase has been found [94]. The transition temperature $T_N$ into this phase has been initially observed in magnetisation and NMR measurements [93]. $T_N$ is also clearly visible in the magnetic susceptibility and magnetoresistnance measurements [95]. The phase appears at a Lifshitz point located near $x = 0.02$ at 38 K [91] and $T_N$ extrapolates to zero at $x \approx$ -0.015.

The lack of any ordered moment in the magnetisation previously suggested that this phase is characterised by a modulated magnetic order. Recent electron spin resonance (ESR), muon spin relaxation ($\mu$SR) and Mössbauer spectroscopy studies have, pointed to a spin density wave (SDW) as the order of this phase [96]. This has since been verified, using neutron scattering measurements [39]. For $x = 0.0019$, at $T = 36.4$ K a magnetic ordering wavevector $\mathbf{Q}_{SDW} = (0\ 0\ \ell_{SDW})$ with $\ell_{SDW} = 0.095$ r.l.u. is observed. Meanwhile, $\ell_{SDW}$ displays a $T$ and $x$ dependence where $\ell_{SDW}$ decreases on approaching the FM phase, but remains finite up to $T_c$.

Beyond $x =$ -0.015 the system enters a second FM state [93], however demonstrates qualitative differences to the Fe-rich FM phases, confirming the two states

are different in nature [91]. The FM states are demonstrated to be intrinsic to the $C14$ Laves phase, rather than originating from an impurity phase, as suggested by [88].

There has been significant effort to simulate the effects of both Nb and Fe Doping using density functional theory calculations (DFT) [88, 89]. At stoichiometry,

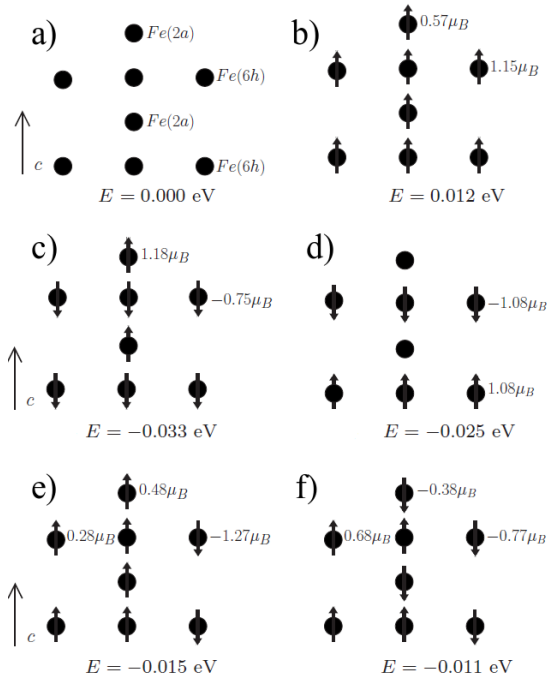


**Figure 4.4:** Potential spin configurations of Fe atoms in $NbFe_2$. Configuration *(c)*, having the lowest energy, is believed to represent the ground state of the stoichiometric system [89].

$x = 0$, the lowest energy and hence dominant order is ferrimagnetic [89]. Here, Fe($2a$) sites have a moment of 1.18 $\mu_B$ while each Fe($6h$) has 0.75 $\mu_B$ in the opposite direction, this is shown in figure 4.4.c. Supporting this, a combination of *ab initio* calculations and spin-dependent Compton scattering was used to determine a ferrimagnetic arrangement of Fe moments, through which the Fe($2a$) sites were found to align antiparallel to the bulk moment [88].The disparities found between experimental and computational results show that the DFT models used do not capture all of the physics relevant for the $Nb_{1-x}Fe_{2+x}$ system.

An important aspect of $Nb_{1-x}Fe_{2+x}$ seems to be the presence of strong elec-

tronic correlations [80]. This is characterised by a very high magnetic susceptibility, $\chi \sim 0.02$, along with an enhancement in the specific heat capacity Sommerfeld coefficient of $\gamma = C/T \simeq 45$. This results in a Wilson ratio of $R_W \simeq 60$, suggesting extreme proximity of ferromagnetism.

This is particularly apparent at $x \approx$ -0.015, where the SDW is suppressed. Here, the resistivity and heat capacity deviates from conventional Fermi-liquid behaviour, implying the presence of a quantum critical point (QCP) [91, 97, 80, 39]. Measurements at $x =$ -0.01 reveal a $T^{3/2}$ power-law dependence of the resistivity $\rho$ as well as a logarithmic temperature dependence of the Sommerfeld coefficient $\gamma = C/T$. This spans near 2 orders of magnitude in $T$, extending down to 0.1 K [80].

### 4.2.1 $Nb_{0.981}Fe_{2.019}$ - OFZ28 Growth and Characterisation

The $Nb_{0.981}Fe_{2.019}$ crystal presented here (OFZ28.3.2.4) was grown and characterised by Dr. William Duncan, in collaboration with Andreas Neubauer and Wolfgang Münzer. Seed and feed rods were grown in the radio frequency induction furnace at Royal Holloway, before the crystal was then grown using the ultra high vacuum (UHV) optical floating zone (OFZ) furnace, at the E21 institute of the Technical University Munich, which has been adapted for metallic growths. The growth rods were rotated via a magnetic mechanism, allowing the atmosphere to remain completely isolated, and the chamber connected to a turbo pump generating a vacuum of $\leq 10^{-9}$ mbar. The feed and seed rods used 99.99% Puratronic niobium powder and 99.99% Puratronic iron powder, which were degassed in UHV down to $10^{-8}$ mbar, prior to being melted into rods. The Nb bar was then annealed in an UHV radio frequency furnace at $\sim 2400°$C, for one week.

The single crystal was then characterised extensively via resistivity, susceptibility and magnetisation measurements, as well as by X-ray diffraction and neutron depolarisation [98]. Neutron diffraction reveals the OFZ28 growth to be polycrystalline in nature, with several regions. Towards the end of the growth rod is a large section of single crystal $Nb_{0.981}Fe_{2.019}$, with mosaicity between 0.3°

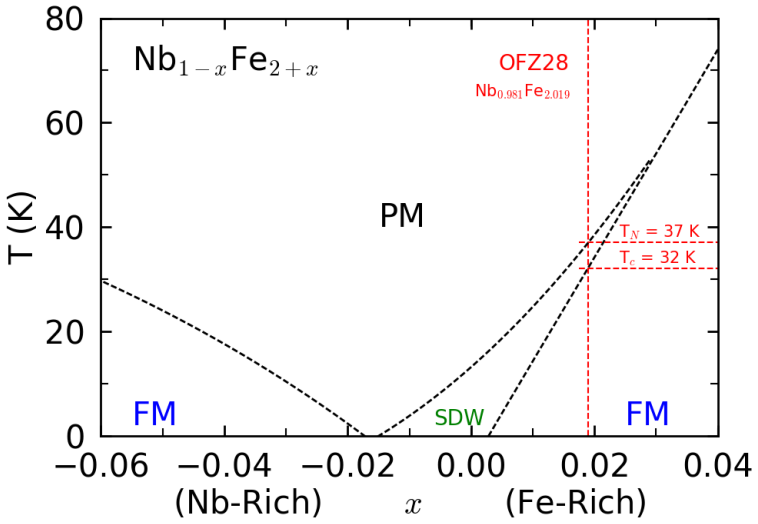


**Figure 4.5:** Temperature vs doping phase diagram of $Nb_{1-x}Fe_{2+x}$ , displaying the positioning of the Fe-rich OFZ28 sample, adapted from [12].

and 0.4°. Depolarisation measurements were performed on the entire rod which showed a wide range of depolarisation temperatures.

A range of physical property measurements were performed on the sample, in both $\mathbf{c}||H$ and $\mathbf{a}||H$ orientations. Real and imaginary parts of the AC susceptibility show a maximum at 29.5 K for $\mathbf{c}||H$ and 28 K for $\mathbf{a}||H$, although there is no corresponding peak or anomaly in any resistivity measurements.

## 4.3 Neutron Diffraction

As described in previous sections, the $Nb_{1-x}Fe_{2+x}$ composition-temperature phase diagram, in zero field, contains a spin-density wave (SDW) phase, at the ferromagnetic quantum phase transition. This section investigates the evolution of that SDW state, with increasing field. In particular, the field-temperature phase diagram, for $H||c$, of a sample with composition $Nb_{0.981}Fe_{2.019}$. This experiment was performed at the FRM II facility on the MIRA triple axis spectrometer. The *ac* scattering plane was chosen.

### 4.3.1 Data Analysis

Data is first normalised to a monitor value of 140,000 counts, corresponding to an exposure time of ≈5 minutes. Data is fitted using a standard Gaussian distribution plus constant background:

$$f(x) = ae^{\frac{(x-b)^2}{2\sigma_x^2}} + c \tag{4.1}$$

where $a$ is the peak intensity, $b$ the peak position in $\mathbf{Q}_{(SDW,x)}$, $\sigma_x$ the standard deviation and $c$ the constant background. The Full Width at Half Maximum (FWHM) is calculated using the formula:

$$FWHM = 2\sqrt{2ln2}\sigma_x \approx 2.355\sigma_x \tag{4.2}$$

In order to generate the phase diagram, intensities, $I(B,T)$, were calculated using the following formula:

$$I(B,T) = FWHM_l \times FWHM_h \times a_l \tag{4.3}$$

Only the amplitude of the $\ell$ scans are used in this determination due $h$ scans not always passing precisely through the peak maxima, due to the $T$ dependence of $\mathbf{Q}_{SDW}$ .

### 4.3.2 Diffraction Results

Measurements were performed over a wide region of the temperature - field space, as shown in figure 4.6. Presented below are a number of measurement sets exemplifying the diffraction of neutrons by the magnetic order at key $T-B$ positions.

Scanning first in temperature, at zero field, we see clear magnetic diffraction at (1 0 2-$\ell_{SDW}$), with $\ell_{SDW} \sim 0.092$, between 30 and 36 K, see figure 4.7. As the temperature is lowered towards $T_N$, at ≈ 37 K, a broad peak begins to emerge signalling the onset of the SDW phase. The amplitude of this peak reaches its maximum at $T \approx 33$ K and is then completely suppressed again by $T \approx 30$ K. This suppression is expected given the observation of ferromagnetism below

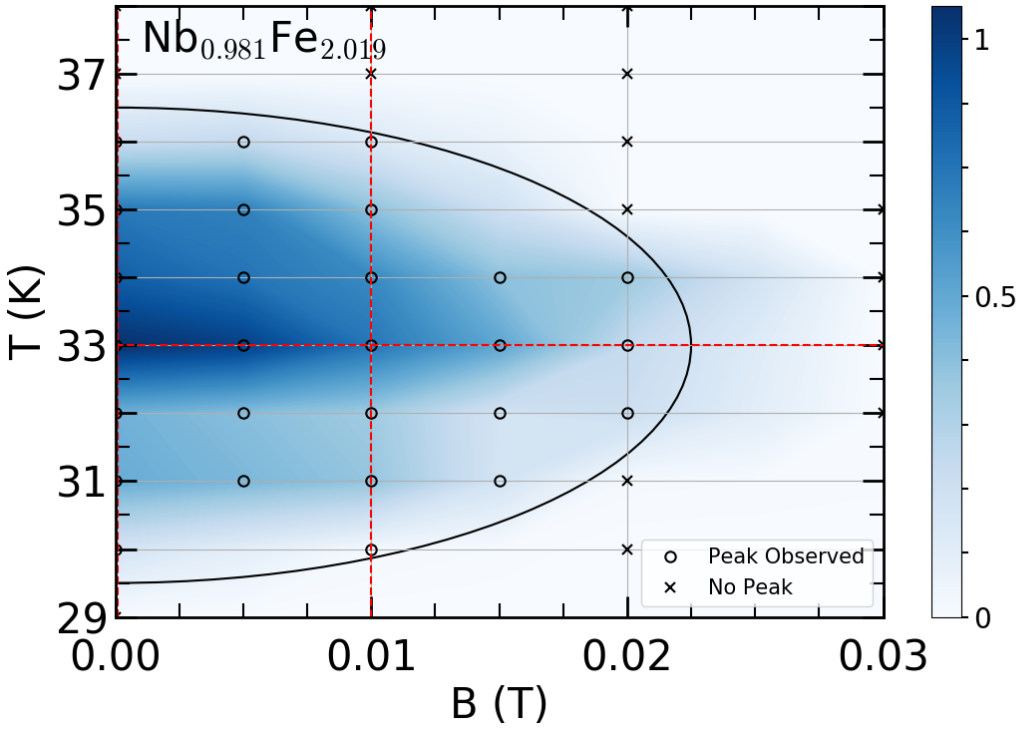


**Figure 4.6:** Field-temperature phase diagram of the SDW order found in $Nb_{0.981}Fe_{2.019}$. The position of the diffraction measurements shown in figures 4.7, 4.8 and 4.9 are marked by the red dashed lines. A rough phase boundary, serving purely as a guide to the eye, is shown by the solid black line.

$T_C \approx 32$ K [80]. This rise and fall of intensity is shown in figure 4.7.a, calculated via equation 4.2 and normalised to the peak at 33 K and 0 T. As temperature is decreased, the FWHM of the SDW peak remains fairly constant, broadening very slightly at lower temperatures (figure 4.7.b). While, in the $\ell$ direction at least, the SDW peak is observed to shift towards the nuclear position at lower temperatures (figure 4.7.c).

With zero external field, the highest SDW diffraction intensity is found at 33 K, just above the critical temperature of $T_C \approx 32$ K. Figure 4.8 shows diffraction at the $Q_{SDW}$ position of (1 0 -2-$\ell_{SDW}$) at fields between 0.0 T and 0.06 T. As the field strength is increased, the magnetic ordering is suppressed and the peak amplitude reduced, with complete suppression just after $H_c \simeq 0.02$ T. Figure 4.8 shows only the measurements made with decreasing field, however measurements

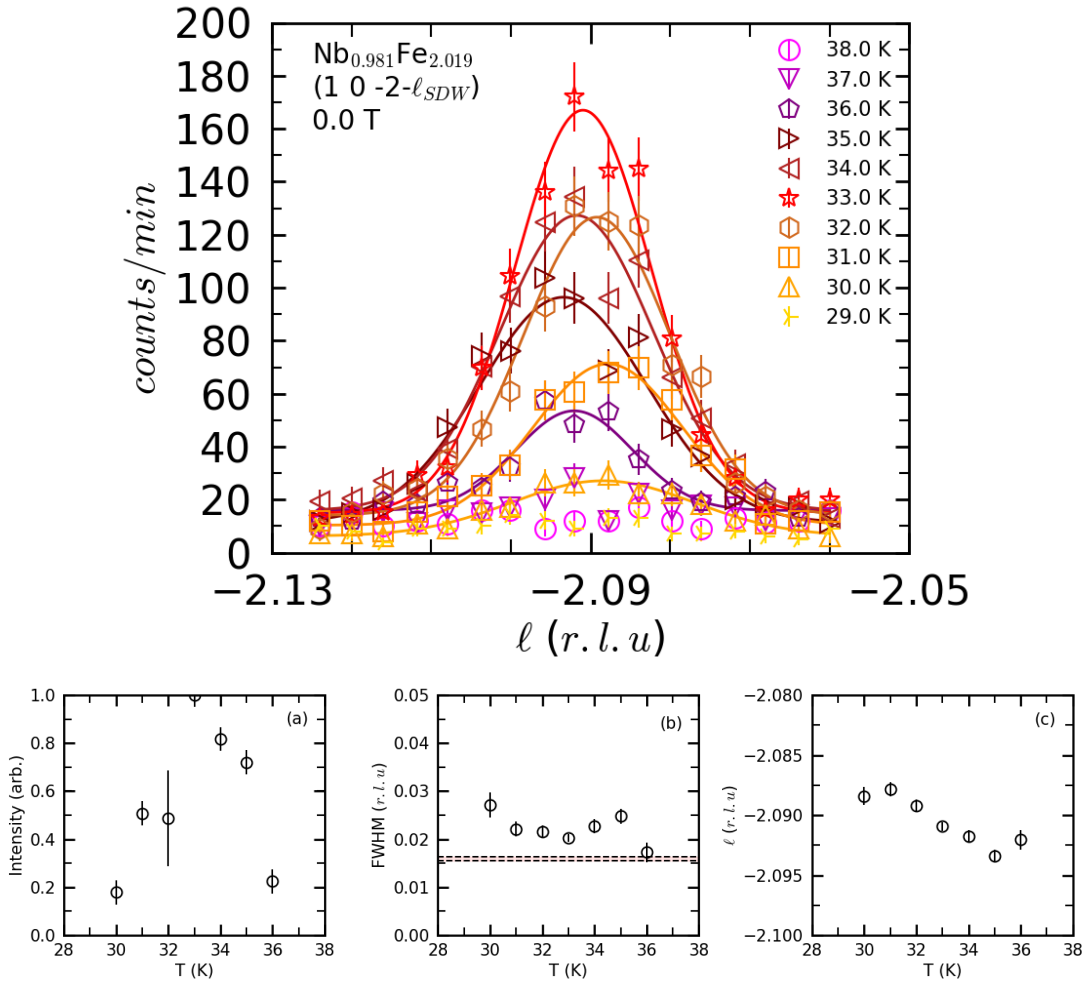


**Figure 4.7:** (*top*) Temperature dependence of neutron diffraction of the SDW satellite peak near (1 0 2.092) between 38 K and 29 K in zero field. As temperature decreases, the magnetic order emerges around the ordering temperature $T_N \approx 37$ K, increases to a maximum amplitude at 33 K, then decays completely by 30 K. (*a*) Normalised peak intensity vs temperature, showing a maximum at 33 K. Values are calculated using equation 4.2. The large error at 32 K is due to poor $h$ scan data. (*b*) Evolution of the full width at half maximum with decreasing temperature. The area marked by the dashed lines indicate the $FWHM$ of the nuclear peak. (*c*) $\ell$ position of the SDW peak.

with increasing field strengths yielded similar results, shown in figures 4.8.a-c. Here the effect of increasing field is clearly visible; intensity decreases, the FWHM remains roughly constant and the $\mathbf{Q}_{(SDW,\ell)}$ value shifts towards the nuclear peak at lower fields.

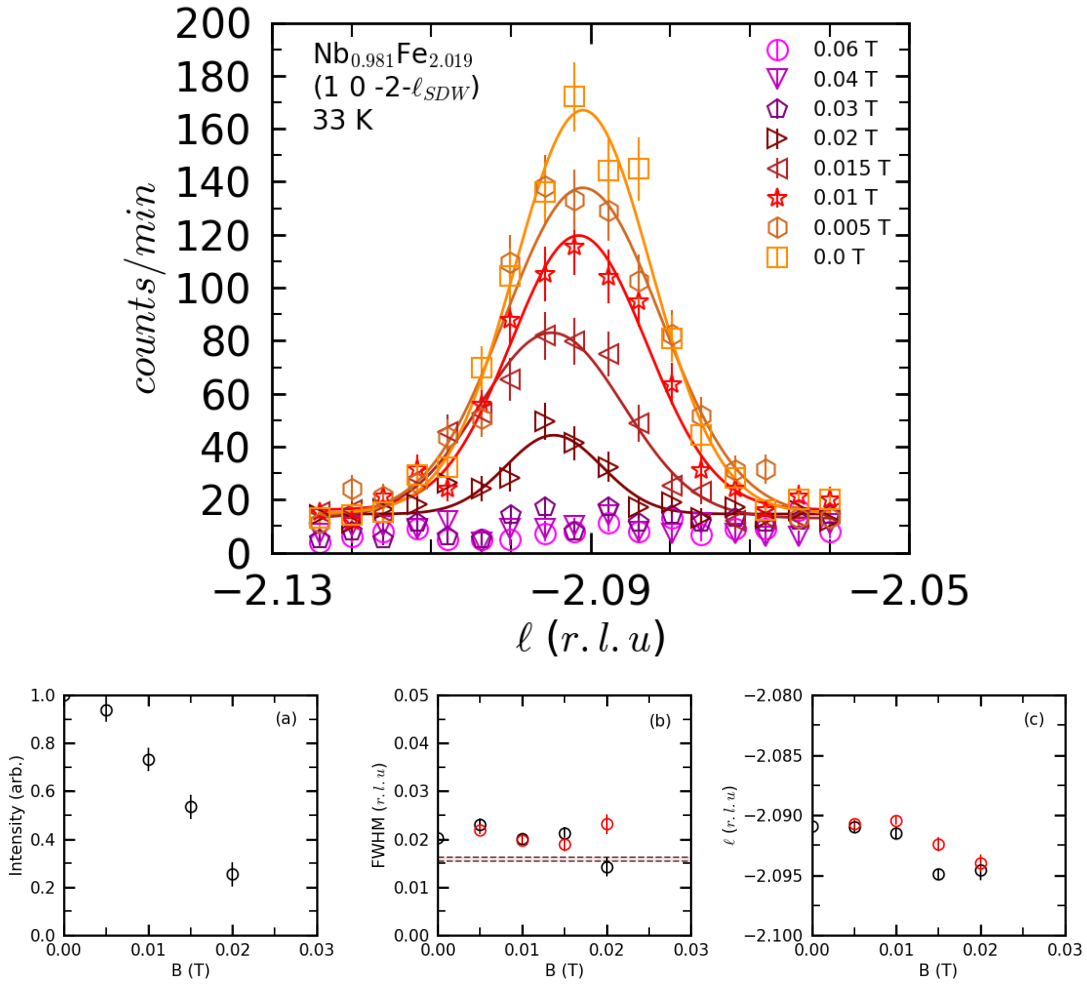


**Figure 4.8:** (*top*) Field dependence of neutron diffraction of the SDW satellite peak near (1 0 2.092), at 33 K. As the field strength is increased, order is suppressed. Between $H = 0.02$ and $H = 0.03$ T the SDW order fully disappears. Only down sweep measurement are shown for clarity.(*a*) Normalised peak intensity vs field at 33 K, as field is increased the peak intensity is suppressed. Values are calculated using equation 4.2. (*b*) Evolution of the full width at half maximum value with increasing (red) and decreasing (black) magnetic fields. The area marked by the dashed lines indicate the $FWHM$ of the nuclear peak at 33 K. (*c*) $\ell$ position of the magnetic Bragg peak, from measurements with increasing (red) and decreasing (black) field.

Figure 4.9 shows the temperature dependence of neutron diffraction at the $\mathbf{Q}_{SDW}$ position at a constant field of 0.01 T. Measurements were taken with both decreasing and increasing temperature sweeps. The SDW order begins to

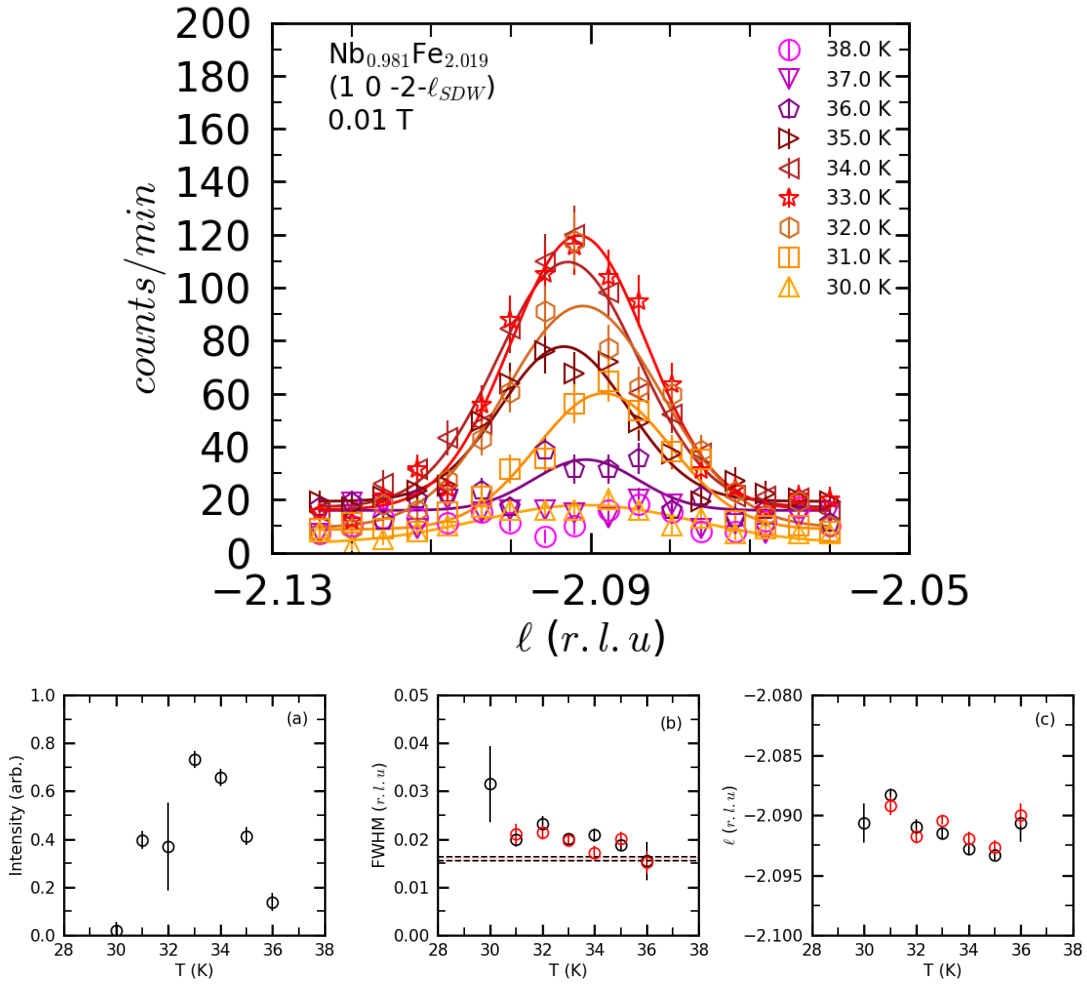


**Figure 4.9:** (*top*) Temperature dependent neutron diffraction of the $\mathbf{Q}_{SDW}$ position in $Nb_{0.981}Fe_{2.019}$ at H = 0.01 T. As temperature decreases, the magnetic order emerges around the ordering temperature $T_N \approx 37$ K, increases to a maximum amplitude at 33 K, then decays completely by 30 K. (*a*) Normalised intensity vs temperature plot at 0.01 T. Visible is a clear maximum at 33 K, amplitude decreasing out to 30 and 36 K. Values are calculated using equation 4.2. The large error at 32 K is due to poor $h$ scan data. (*b*) Evolution of the full width at half maximum value with increasing (red) and decreasing (black) temperatures at H = 0.01 T. The area marked by the dashed lines indicate the FWHM of the nuclear peak at 0.01 T. (*c*) $\ell$ position of the SDW order peak, from measurements during heating (red) and cooling (black).

emerge at 36 K, just below $T_N \approx 37$ K at zero field, increases to a maximum coherence at 33 K and then decaying, disappearing by ≈30 K. Despite a very similar temperature range to the zero field measurements, the intensities of the

diffraction peaks at 0.01 T are slightly weaker, indicating some suppression of the order. This is clear when comparing figures 4.7 and 4.8. Comparison of heating and cooling data sets show the peak amplitudes, FWHM and peak position values to remain consistent, within the established error.

### 4.3.3 Discussion

The final temperature-field phase diagram is presented in figure 4.10. The relative diffraction peak intensities have each been normalised to the 33 K, $H = 0$ T peak, given this position shows the strongest diffraction. This diagram clearly show the existence of a SDW region between $\approx$ 30 K and 36 K, the darker regions indicating a stronger order. This spin density wave ordering is suppressed via the introduction of an external field, becoming undetectable after $\approx$ 20 mT at 33 K. Away from 33 K however, this critical field reduces rapidly, the parabola in figure 4.10 serving as a guide to the eye and indicating a suggested phase boundary.

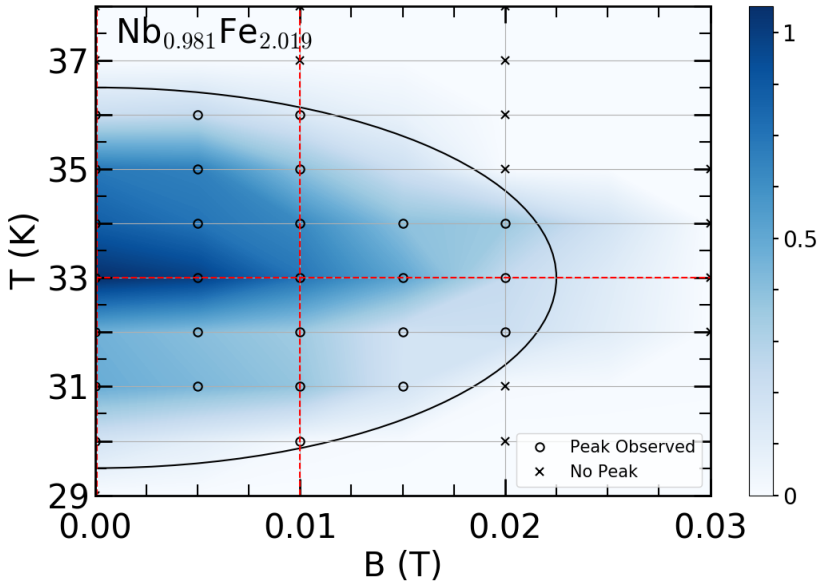


**Figure 4.10:** Field-temperature phase diagram of the SDW order found in $Nb_{0.981}Fe_{2.019}$. The position of the diffraction measurements shown in figures 4.7, 4.8 and 4.9 are marked by the red dashed lines. A rough phase boundary, serving purely as a guide to the eye, is shown by the solid black line.

These results are qualitatively similar to those published in [99], the $H - T$

phase diagram obtain through neutron diffraction and bulk susceptibility measurements, shown in figure 4.11. In their case the field required to suppress the SDW order is of the same magnitude but slightly larger, ∼0.06 T, simply due to the sample being slightly less Fe-rich. This results in a slightly weaker initial FM phase, demonstrated by the lower transition temperature.

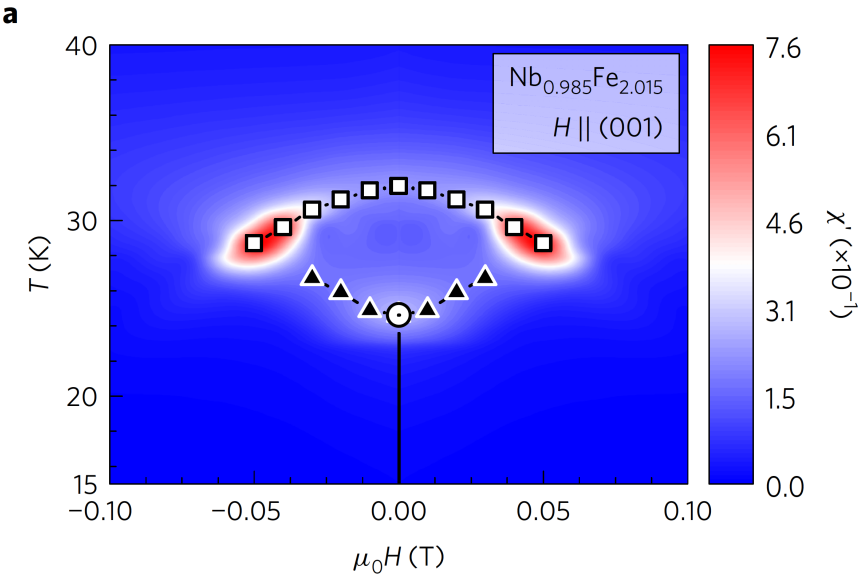


**Figure 4.11:** Temperature-magnetic field phase diagram for Fe rich $Nb_{0.985}Fe_{2.015}$. Colour shows the real part of the a.c. magnetic susceptibility $\chi'$(H, T) [99].

## 4.4 Inelastic Neutron Scattering

In the previous section we have shown that the phase diagrams detailing the SDW phase masking FM order, obtained through magnetic susceptibility and neutron scattering measurements, agree not only in zero field but also at finite field. Presented in this section are inelastic neutron scattering measurements, performed using the triple-axis spectrometer 4F2 at LLB (section 3.5.2.2), probing the low-energy spectra in the vicinity of the SDW phase. These findings are then compared to the model of a damped harmonic oscillator, as is predicted for the behaviour of ferromagnetic quantum criticality, the details of which are outlined in Section 2.3.

### 4.4.1 Data Correction

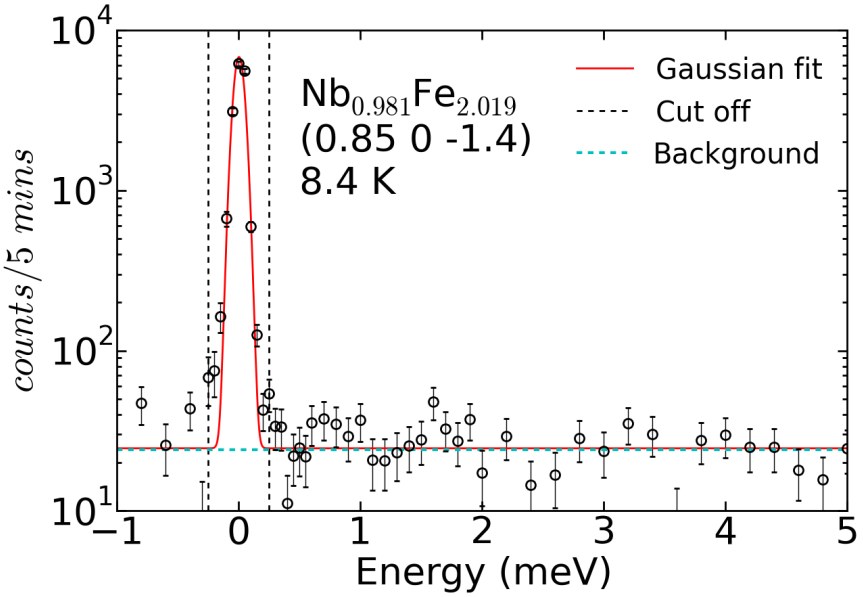


**Figure 4.12:** Background measurement of inelastic neutron scattering found in $Nb_{0.981}Fe_{2.019}$ at (0.85 0 -1.4) at 8.4 K. The red line shows the Gaussian fit function including a constant background, the black dashed lines indicates the points at which the elastic line contribution is less than 1 count.

The first step in the analysis process is to attain the true value of the monitor count. As discussed in previous sections (3.5.2), higher harmonic neutrons are not filtered by the monochromator and therefore contribute to the monitor count, but not the final signal. To correct for this, a $\mathbf{k}_i$ dependent factor, supplied by the beamline, is applied to the count value. From this, a true monitor count can be determined. This value was then normalised to 10,000, equating roughly to a 5 min exposure.

Next the background of the normalised data is determined using measurements at (0.85, 0, 1.4), see figure 4.12. This measurement is far enough from nuclear Bragg peaks or regions of significant excitations as to consist only of an incoherent elastic line and background noise. The elastic line is fitted using a simple Gaussian function and the background with a constant:

$$I = Ae^{-\frac{(E-E_0)^2}{2\sigma^2}} + c \tag{4.4}$$

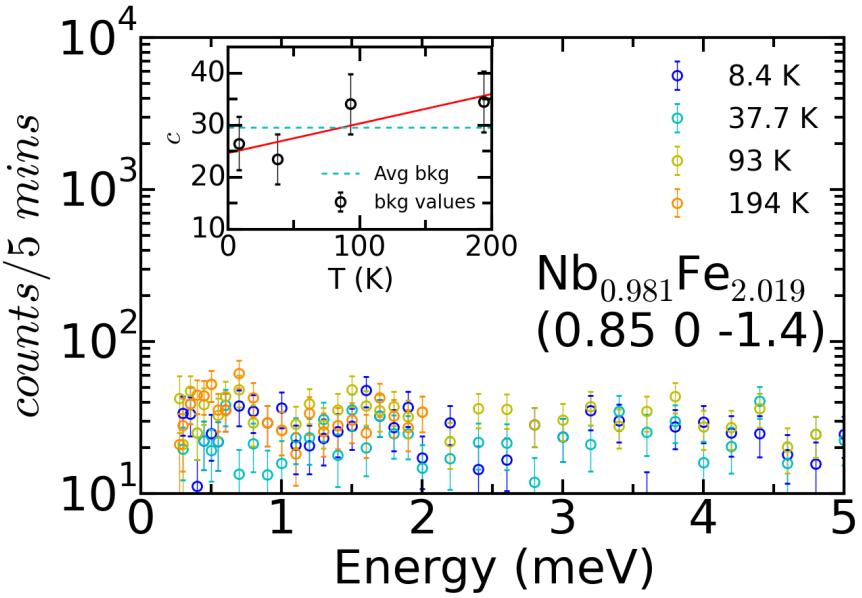


**Figure 4.13:** Background of the inelastic neutron scattering data as measured at (0.85 0 -1.4). Data sets at different temperatures have been fitted with a constant. The inset shows the temperature dependence of the background, fitted with a linear function (red line). The slope is within the error of this set of experiments. The average background in the measured temperature range is indicated by the turquoise dashed line.

Here $A$ denotes the amplitude, $E_0$ peak position, $\sigma$, the standard deviation and $c$ the constant background. From the fitted data the energy at which the elastic line contribution becomes insignificant (less than 1 count) is determined, here a value of $\pm 0.25$ meV. The stability of $E_0$ was also checked and found not to move from the $E_0 = 0$ position. The remaining background signal was checked for any forms or incoherent structure using Gaussian and Lorentzian functions, however, in each case the best fit was found to be a simple constant. This process was repeated over a number of temperatures.

The constant background at a number of temperatures is shown in Figure 4.13. Although there appears to be a weak temperature dependence, this is within the error of this set of measurements and a temperature independent constant background of 29 counts/5 mins has therefore been subtracted from the normalised data.

After background subtraction, the normalised raw data, the remaining signal

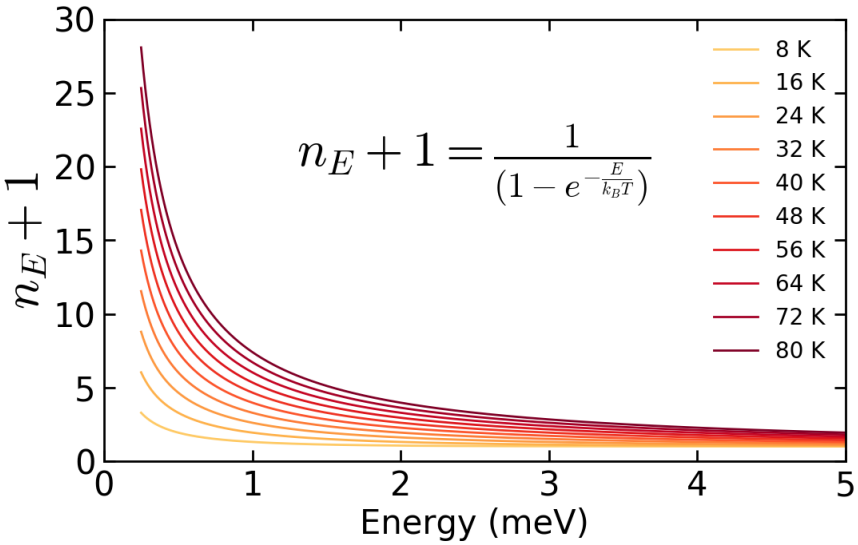


**Figure 4.14:** Energy Temperature dependence of detailed balance factor.

has been divided by the detailed balance factor of $1/(1 - e^{-E/k_B T})$ in order to obtain the imaginary part of the magnetic susceptibility $\chi''$. Figure 4.14 demonstrates how this factor increases with temperature. The simultaneous effect of background subtraction and division by the detailed balance factor is shown in figure 4.15.

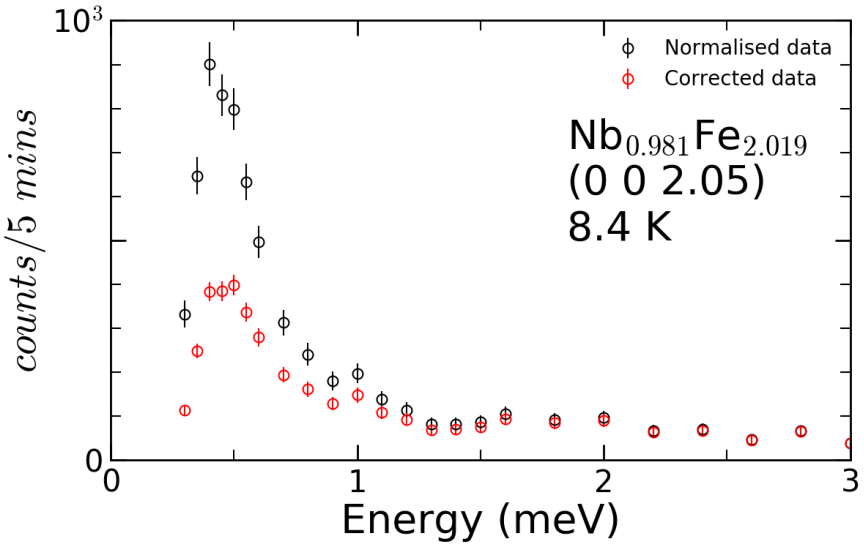


**Figure 4.15:** Inelastic neutron scattering measurement at (0 0 2.05) and 8.5 K. Black points represent raw normalised data, prior to background subtractions and detailed balance correction. Red points depict the same data set after the detailed balance correction has been applied.

### 4.4.2 Data Fitting

As shown in section 2.3, the excitations predicted for the vicinity of a FM-PM transition are modelled by over-damped harmonic oscillations. Even as measurements move away from this point, the system is assumed to be described by a simple damped harmonic oscillator model. The imaginary part of the magnetic susceptibility, representing the energy dependent response of each magnetic mode, is given by:

$$\chi'' = \frac{\chi_0 D E_0^2 E}{(E^2 - E_0^2)^2 + E^2 D^2} \tag{4.5}$$

here $\chi_0$ is the static susceptibility, $E_0$ the resonance energy and $D$ the damping factor. In the over-damped regime, $D >> E_0$. Equation 4.5 is reduced to:

$$\chi'' = \frac{\chi_0 \Gamma E}{\Gamma^2 + E^2} \tag{4.6}$$

where $\Gamma = E_0^2/D$. In the limit of critical fluctuations, i.e. $\Gamma \to 0$, equation 4.6 further reduces to:

$$\chi'' = \frac{A}{E} \tag{4.7}$$

where $A = \chi_0 \Gamma$.

### 4.4.3 Inelastic Neutron Scattering Results

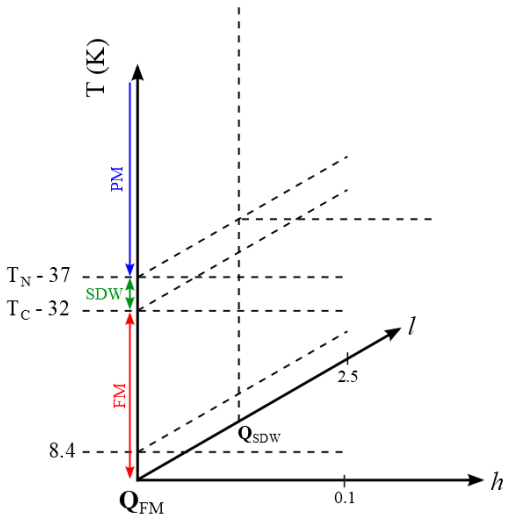


**Figure 4.16:** $h$-$\ell$-$T$ space indicating the cuts (dashed lines) of the inelastic neutron scattering measurements of $Nb_{0.981}Fe_{2.019}$. Also indicated are the Néel temperature, $T_N$ =37 K, Curie temperature, $T_C$ = 32 K, as well as the regions of the various magnetic phases.

It is well established that at the stoichiometry of our sample, $x = 0.019$, $Nb_{1-x}Fe_{2+x}$ exists as paramagnetic down to the Néel temperature of $T_N = 37$ K [99]. At this point, the systems orders into a spin density wave state, which remains down to the Curie temperature of $T_C = 32$ K, where upon it undergoes yet another magnetic phase transition, to an ordered ferromagnetic state. Presented below are inelastic neutron scattering measurements of the low-energy excitations, found near the (0 0 2) position. Figure 4.16 provides a pictorial representation of the measurement space.

This section begins with measurements taken with the system firmly in the FM phase, at $T = 8.4$ K, before moving to measurements taken at the transition temperatures of $T_C$ and $T_N$, at the $\mathbf{Q}_{FM}$ and $\mathbf{Q}_{SDW}$ positions. The temperature dependence of the low energy excitations is then investigated, both at the $\mathbf{Q}_{FM}$ and $\mathbf{Q}_{SDW}$ positions.

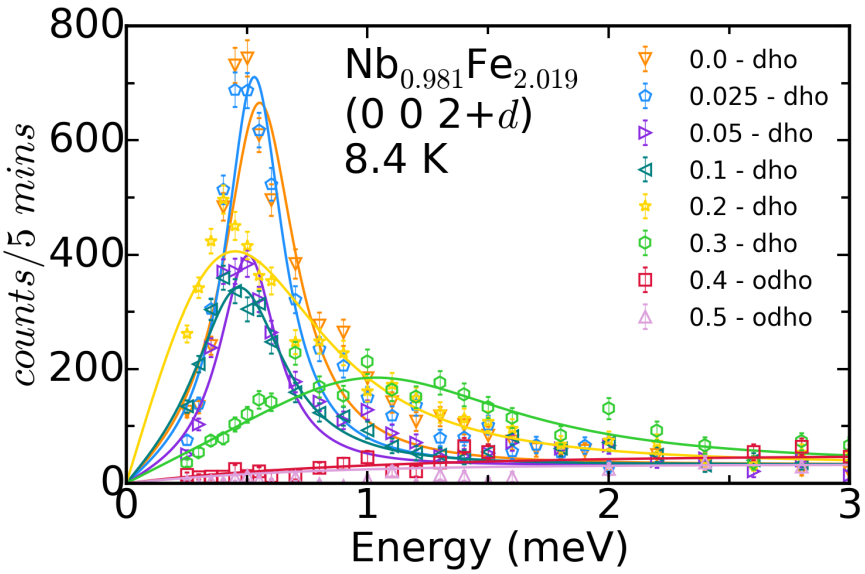


**Figure 4.17:** The $\ell$ dependence of the low energy excitations found in $Nb_{0.981}Fe_{2.019}$ at (0 0 2±$d$) and 8.4 K. In the FM region, well defined damped excitations are visible, which broaden as the measurements move away from the $\mathbf{Q}_{FM}$ position. The legend specifies where the data has been fitted using a damped or over-damped harmonic oscillator model (dho or Odho respectively).

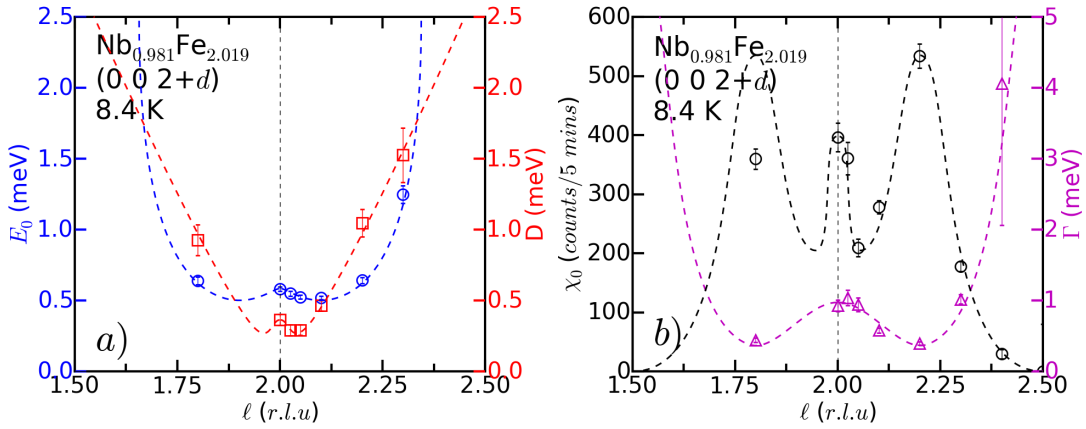


**Figure 4.18:** Fit parameters characterising the $\ell$ dependence of the low-energy spectra in $Nb_{0.981}Fe_{2.019}$ at 8.4 K. Parameter obtained via fits using the damped harmonic oscillator (equation 4.5) and the over-damped harmonic oscillator (equation 4.6) models. (a) shows excitation energy $E_0$ (blue circles) and damping factor $D$ (red triangles). (b) shows static susceptibility $\chi_0$ (black circles) and quasielastic line width $\Gamma$ (purple triangles). Dashed lines serve as guides to the eye.

#### 4.4.3.1 Low energy excitations in the FM phase

Figure 4.17 displays measurements of the low energy-spectra between (0 0 1.8) and (0 0 2.5), at 8.4 K, firmly in the FM region. Clearly visible are damped low energy excitations, which are soft (low energy) over a wide range of **Q**. These energy spectra have been fitted using either a damped harmonic oscillator (dho) or over-damped harmonic oscillator (odho) model. As the measurements are taken further away from the $\mathbf{Q}_{FM}$ position, we see a general increase in the excitation energy, as well as broadening of the excitation. The precise fit parameters, describing the excitation, are shown in figure 4.18. Here we can see that these damped excitations have an energy of less than 1 meV, over a considerable **Q** range, the minimum energy being 0.51 ± 0.11 meV at a position of $d_\ell = 0.1$ $r.l.u$, roughly the $\mathbf{Q}_{SDW}$ position at $T_C$ of $d_\ell = 0.093$. We observe a minimum damping of 0.29 ± 0.037 meV at $d_\ell = 0.025$ $r.l.u$, again away from the $\mathbf{Q}_{FM}$ position. Both the excitation energy and the damping then increase as $d_\ell$ increases. For the quasi-elastic line width, we see a minimum of 0.4 ± 0.024 meV at $d_\ell = 0.2$ and a considerable increase away from this point. Finally the static susceptibility of the excitations shows a decrease away from the $\mathbf{Q}_{FM}$ position.

The $h$ dependence of the low energy excitations is shown in figure 4.19. Clearly visible are the damped low energy excitations increasing in energy and becoming broader away from the $\mathbf{Q}_{FM}$ position. Again, the energy spectra is fit with either the dho or odho models, attaining the the fit parameters displayed in figure 4.20. Here it is clear that the lowest value of $E_0$, $D$ and $\Gamma$, with $\ell = 2$, are located at the $h = 0$ position, with $E_0 = 0.58 \pm 0.016$ meV, $D = 0.36 \pm 0.039$ meV and $\Gamma = 0.93 \pm 0.079$ meV. The static susceptibility displays a maximum at $h = 0$ and decreases with increasing $|h|$.

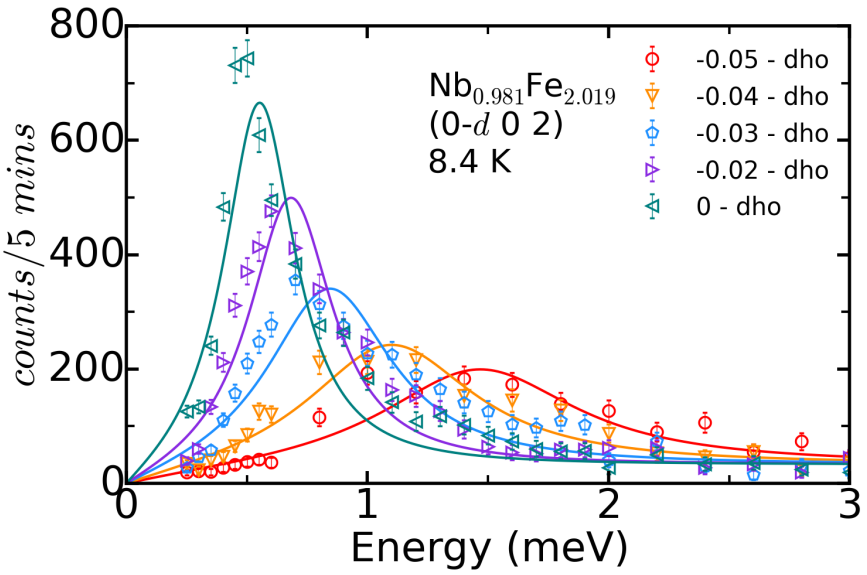


**Figure 4.19:** The $h$ dependence of the low energy excitations found in $Nb_{0.981}Fe_{2.019}$ at (0±$d$ 0 2) at 8.4 K. In the FM region, well defined damped excitations are visible, which broaden as the measurements move away from the $\mathbf{Q}_{FM}$ position. The legend specifies whether the spectra are fitted using a damped harmonic oscillator (dho) or over-damped harmonic oscillator (odho) model.

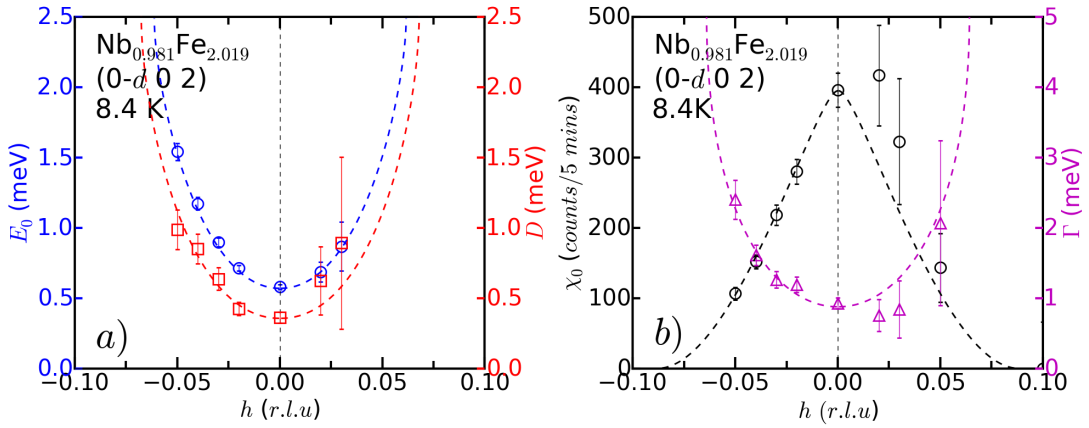


**Figure 4.20:** Fit parameters characterising the $h$ dependence of the low-energy spectra in $Nb_{0.981}Fe_{2.019}$ at 8.4 K. Parameters obtained via fits using the damped harmonic oscillator (equation 4.5) and the over-damped harmonic oscillator (equation 4.6) models. (a) shows excitation energy $E_0$ (blue circles) and damping factor $D$ (red squares). (b) shows static susceptibility $\chi_0$ (black circles) and quasielastic line width $\Gamma$ (purple triangles). Dashed lines serve as guides to the eye.

#### 4.4.3.2 Low energy excitations at $T_C$

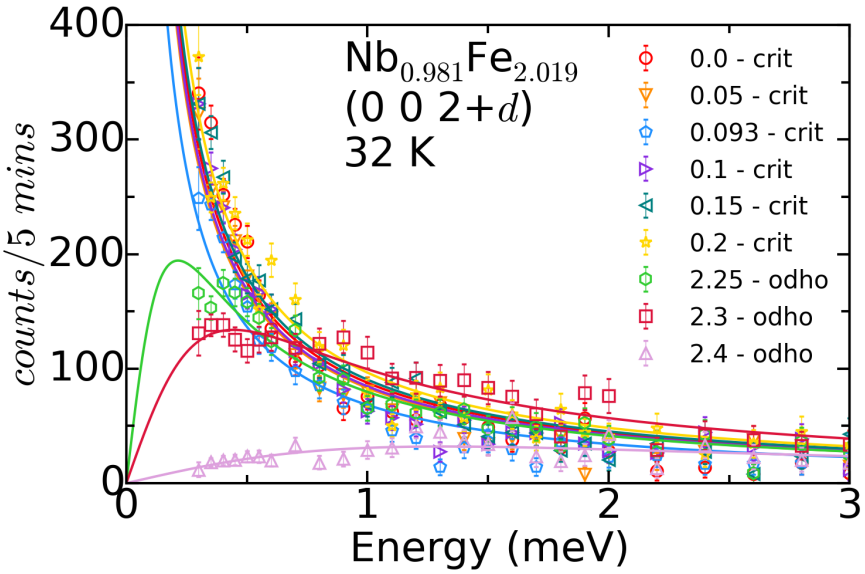


**Figure 4.21:** The $\ell$ dependence of the low energy excitations found in $Nb_{0.981}Fe_{2.019}$ at (0 0 2±$d$) at $T_C$ = 32 K. At the boundary between the ferromagnetic and spin density wave region we observe strongly damped low energy excitations, which broaden as the measurements move away from the $\mathbf{Q}_{FM}$ position. The legend describes whether the data has been fitted with an over-damped harmonic oscillator (odho) model or the model of critical fluctuations (crit).

The low-energy excitations of $Nb_{0.981}Fe_{2.019}$ at the SDW-FM transition temperature of $T_C$ = 32 K are shown in figure 4.21. Here we see the $\ell$ dependence of the low energy excitations found at the phase boundary. These low-energy spectra are here dominated by quasi-elastic scattering, the line width of which broadens when moving away from $\mathbf{Q}_{FM}$ in the $\ell$ direction. The resulting spectra were fit using the over damped harmonic oscillator model (odho), with the parameters shown in figure 4.22. For $\ell$ values close to 2, the line width $\Gamma$ lies within the energy resolution of the experiment, resulting in a $1/E$ dependence of the data. The quasielastic line width has therefore been taken as 0.1 ± 0.1 meV. The line width remains below 0.2 meV for a considerable range, $\ell$ = 2 to $\ell$ = 2.2 *r.l.u.*, before rising for larger $\ell$ while the static susceptibility simultaneously decreases.

The $h$ dependence of the quasi-elastic scattering at $T_C$ is shown in figure

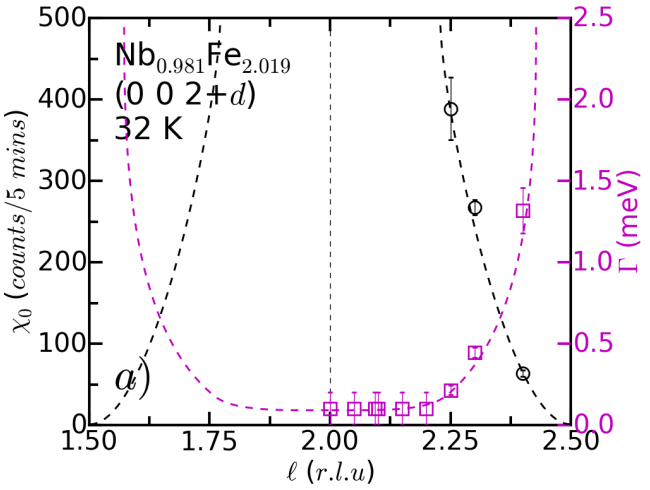


**Figure 4.22:** Fit parameters characterising the $\ell$ dependence of the low-energy spectra in $Nb_{0.981}Fe_{2.019}$ at 32 K. Parameters are obtained via fits using the over-damped harmonic oscillator model, (equation 4.6) or, near (0 0 2) and in the limit $\Gamma << E$, $\chi'' = \chi_0\Gamma/E$. (a) displays static susceptibility $\chi_0$ (black circles), and the quasi elastic line width $\Gamma$ (purple squares).

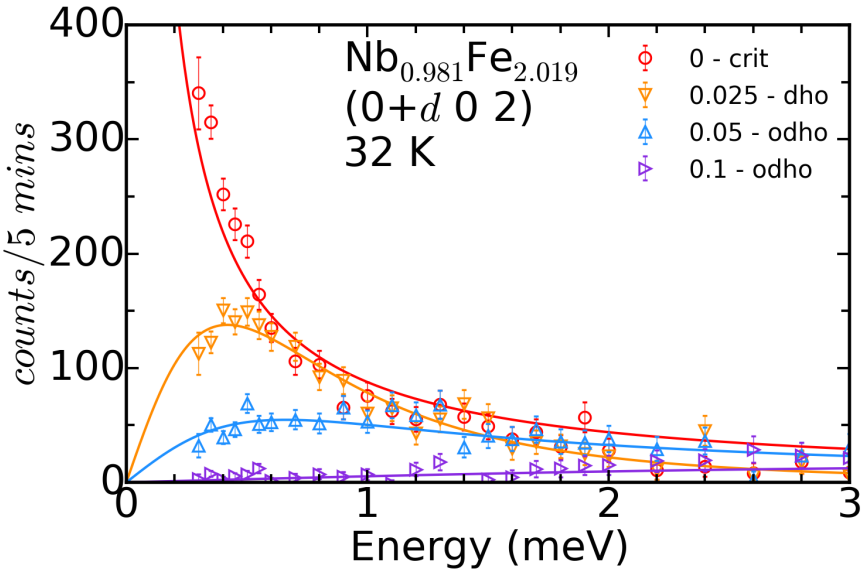


**Figure 4.23:** The $h$ dependence of the low energy excitations found in $Nb_{0.981}Fe_{2.019}$ at (0$\pm d$ 0 2) and $T_C = 32$ K. At the boundary between the ferromagnetic and spin density wave region we observe strongly damped low energy excitations, which broaden as the measurements move away from the $\mathbf{Q}_{FM}$ position. The legend describes whether the data has been fitted with a damped harmonic oscillator (dho), over-damped harmonic oscillator (odho) model or the over-damped model in the limit $\Gamma << E$ (crit).

4.23. Here the low energy excitations are suppressed far more quickly along the $h$ direction than along the $\ell$ axis. By $d_h = 0.025$ *r.l.u.*, the line width is already larger than the energy resolution of 0.2 meV, with the quasi elastic scattering becoming broader and weaker with increasing $h$ and being almost completely suppressed by $h = 0.1$ *r.l.u.* By comparison, the same level of damping is not seen until $d_\ell = 0.25$ *r.l.u.*, with excitations still not completely suppressed at $d_\ell = 0.4$ *r.l.u.*. Figure 4.24 shows the $h$ dependence of the resulting fitting parameters, as was qualitatively observed in figure 4.23, there is a clear decrease in static susceptibility coupled with an increase in the quasi elastic line width.

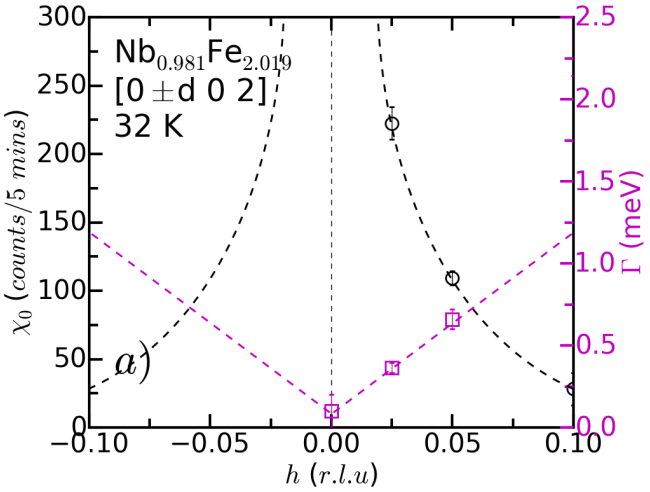


**Figure 4.24:** Fit parameters characterising the $h$ dependence of the low-energy spectra in $Nb_{0.981}Fe_{2.019}$ at 32 K, centred about the $\mathbf{Q}_{FM}$ position. Parameters are obtained via fits using the damped harmonic oscillator model (equation 4.7) or over-damped harmonic oscillator model (equation 4.6), sometimes in the limit $\Gamma << E$ (equation 4.7). Here, static susceptibility $\chi_0$ is depicted with black circles, and the quasielastic line width, $\Gamma$, by purple squares.

#### 4.4.3.3 Low energy excitations at $\mathbf{T}_N$

The low-energy excitations measured at the PM-SDW phase transition, $T_N$ =37 K, are presented in figure 4.25, showing the $\ell$ dependence of the low energy excitations between (0 0 2) and (0 0 2.5). These spectra are characterised by the quasielastic scattering line width, which increases with increasing $\ell$. Curves are fitted using the damped harmonic oscillator and over-damped harmonic oscillator

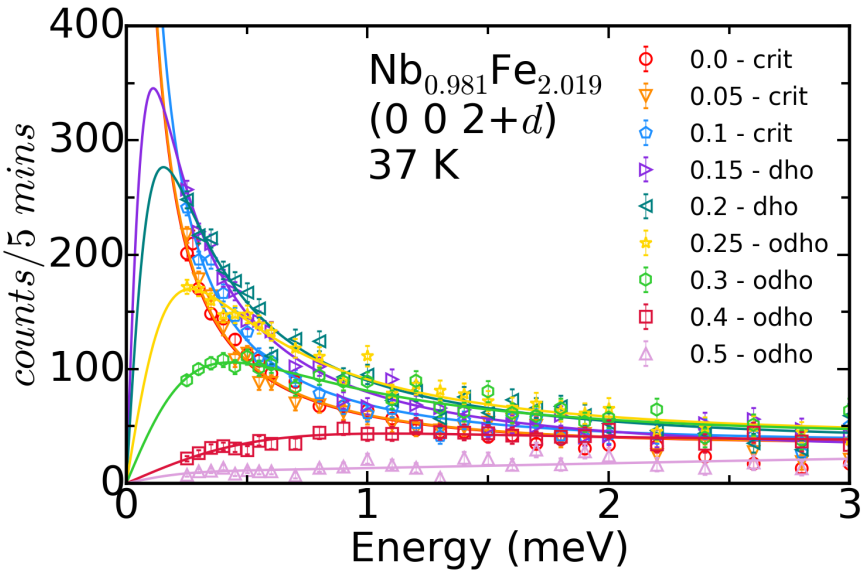


**Figure 4.25:** The $\ell$ dependence of the low energy excitations found in $Nb_{0.981}Fe_{2.019}$ at (0 0 2±$d$) at $T_N$ = 37 K. At the boundary between the spin density wave and paramagnetic region we observe strongly damped low energy excitations, which broaden as the measurements move away from the $\mathbf{Q}_{FM}$ position. The legend describes whether the data has been fitted with a damped harmonic oscillator model (dho), over-damped harmonic oscillator (odho) or, the odho model in the limit $\Gamma << E$ (crit).

models, at times in the $\Gamma << E$ limit, with the fit parameters displayed in figure 4.26. For $\ell$ up to 2.1, the line width lies within the experimental resolution ($\Gamma$ < 0.2 meV) and therefore the data can be fitted with the $1/E$ dependence expected for the critical fluctuations. In this case $\Gamma$ is taken to be 0.1 ± 0.1 meV. Further increasing $\ell$, we observe a reduction of static susceptibility $\chi_0$ and an increase in the quasielastic line width $\Gamma$. The downturn observed out at $d_\ell = 0.5$ *r.l.u.* is likely due to a poor fit of such a broad feature opposed to anything of physical interest.

The $h$ dependence of the quasielastic scattering near the $\mathbf{Q}_{SDW}$ position, (0 0 2.093) to (0.1 0 2.093), is shown in figure 4.27. We see that with increasing $d_h$, the quasielastic scattering broadens. The data are fitted using the damped harmonic oscillator or over-damped harmonic oscillator models, sometimes in the limit $\Gamma << E$, with the fit parameters displayed in figure 4.28. Once again, we see a rapid decrease in static susceptibility, alongside an increase in the quasielastic

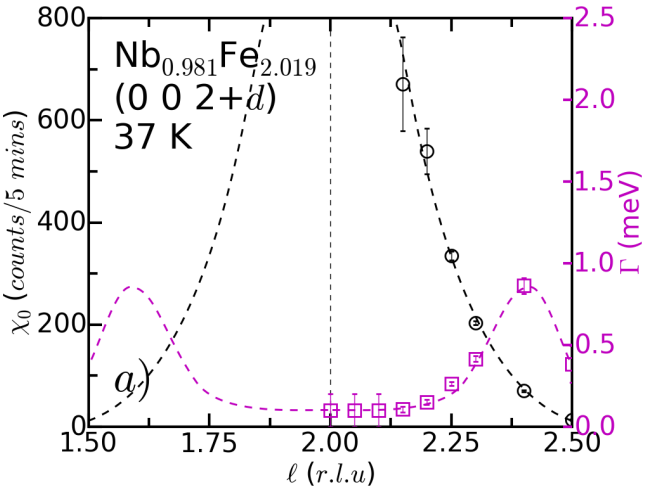


**Figure 4.26:** Fit parameters characterising the $\ell$ dependence of the low-energy spectra in $Nb_{0.981}Fe_{2.019}$ at 37 K, near the (0 0 2) position. Parameters are obtained via fits using the damped harmonic oscillator model (equation 4.5) or over-damped harmonic oscillator model (equation 4.6) sometimes in the $\Gamma << E$ limit (equation 4.7). Here, static susceptibility $\chi_0$ is depicted via black circles, and the quasielastic line width, $\Gamma$, by purple squares.

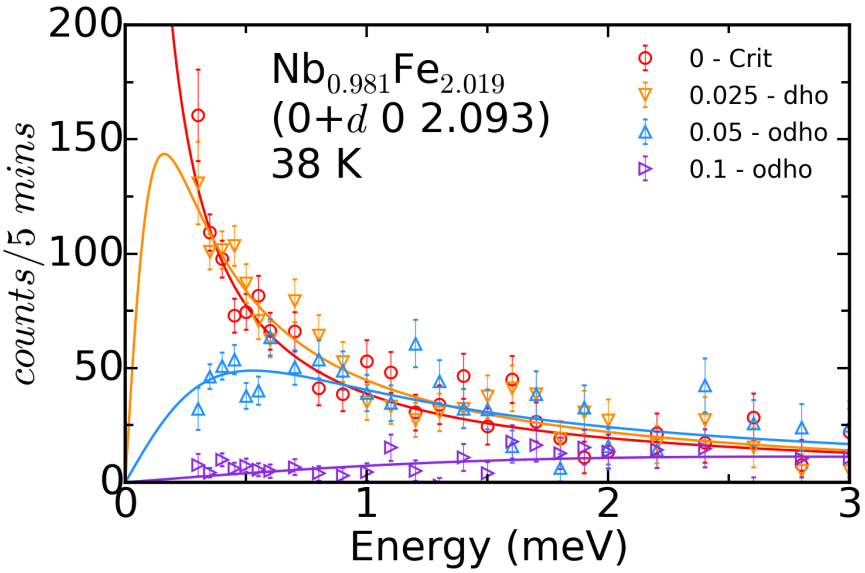


**Figure 4.27:** The $h$ dependence of the low energy excitations found in $Nb_{0.981}Fe_{2.019}$ at $(0\pm d\ 0\ 2.093)$ at $T = 38$ K. At the boundary between the paramagnetic and spin density wave region we observe strongly damped low energy excitations, which broaden as the measurements move away from the $\mathbf{Q}_{SDW}$ position. The legend states whether the data has been fitted with a damped harmonic oscillator model (dho), over-damped harmonic oscillator (odho) or the $\Gamma << E$ limit of the odho model (crit).

line width with increasing $d_\ell$.

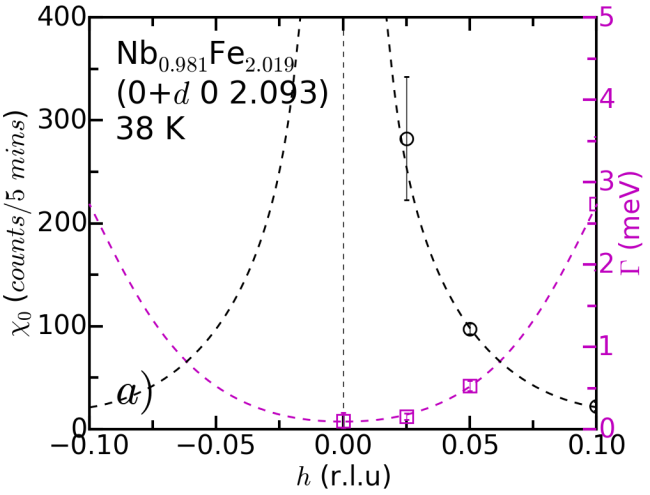


**Figure 4.28:** Fit parameters characterising the $h$ dependence of the low-energy spectra in $Nb_{0.981}Fe_{2.019}$ at 38 K, near the $\mathbf{Q}_{SDW}$ position. Parameters are obtained via fits using the damped harmonic oscillator model (equation 4.7), over-damped harmonic oscillator model (equation 4.6) or the $\Gamma << E$ limit of the over-damped harmonic oscillator model (equation 4.7). Here, static susceptibility $\chi_0$ is depicted via black circles, and the quasielastic line width, $\Gamma$, by purple squares.

#### 4.4.3.4 Temperature dependence of low energy excitations

Figure 4.29 shows the temperature dependence of the low energy excitations found at the ferromagnetic position, $\mathbf{Q}_{FM}$ = (0 0 2). Starting in the low temperature ferromagnetic region, distinct, sharp, low energy excitations are clearly observed below 1 meV. As the temperature is increased, these excitations shift to lower energies and broaden. With increasing temperatures, up to $T_C$ = 32 K, the previously observed well defined excitations decrease in energy, eventually merging with the quasielastic scattering of the elastic line. Beyond the ordering temperature, $T_N$ =37 K, the static susceptibility, $\chi_0$, of the excitations drops off rapidly, presenting a weakening of the quasielastic scattering. The data obtained here were fit using the model of a damped harmonic oscillator below $T_C$ and an over-damped harmonic oscillator above $T_N$. For measurements within the SDW region, the limit of $\Gamma \rightarrow 0$ is assumed. The resulting parameters, associated with

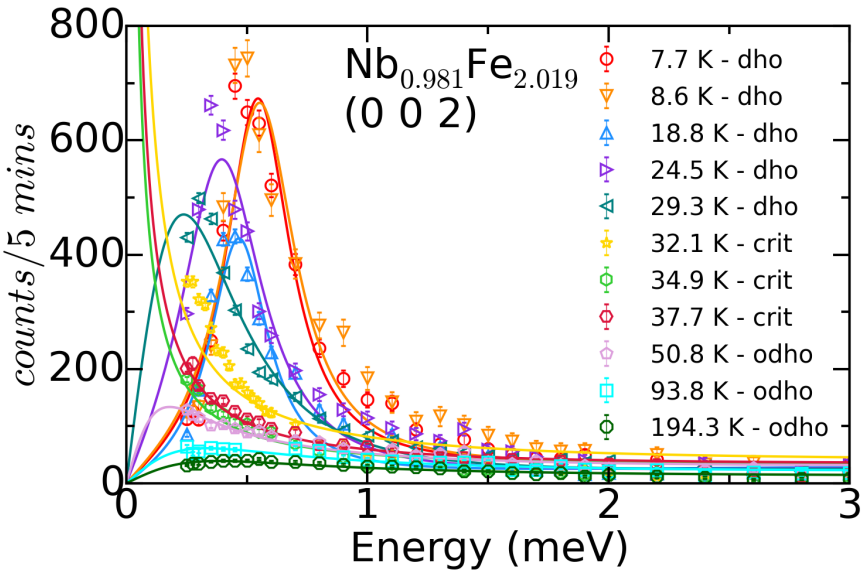


**Figure 4.29:** Temperature dependence of low energy excitations in $Nb_{0.981}Fe_{2.019}$ at the $\mathbf{Q}_{FM}$ position of (0 0 2). The low energy spectra are characterised by well-defined excitations at low temperatures. As $T$ increases, the excitations broaden and become weaker. Data has been fitted with damped harmonic oscillator (dho) or over-damped harmonic oscillator (odho) models, the latter at times in the $\Gamma \to 0$ limit (crit.)

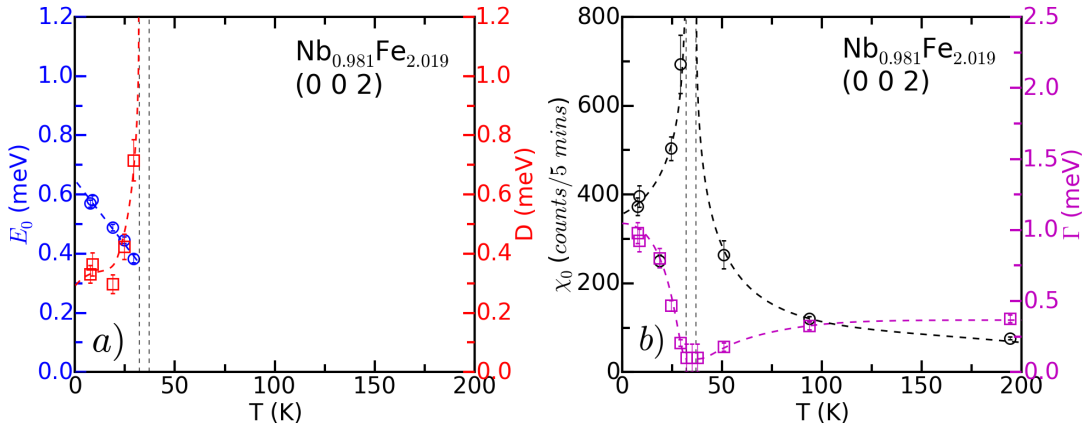


**Figure 4.30:** Fit parameters characterising the $T$ dependence of the low energy excitation spectra at (0 0 2) in $Nb_{0.981}Fe_{2.019}$. Parameters obtained via fits using the damped harmonic oscillator (equation 4.5) and the over-damped harmonic oscillator (equation 4.6) models. (a) shows excitation energy $E_0$ (blue circles) and damping factor $D$ (red triangles). (b) shows static susceptibility $\chi_0$ (black circles) and quasi elastic line width $\Gamma$ (purple circles). Dashed lines serve as guides to the eye.

these fits are presented in figure 4.30. Below $T_C$ it is possible to clearly track the energies $E_0$, and damping, $D$, of the excitations, with $E_0$ clearly increasing with decreasing temperature while $D$ decreases. Meanwhile, $\Gamma$ is seen to decrease as the temperatures approach the SDW region, with the static susceptibility increasing rapidly, this clearly marking the formation of the SDW order.

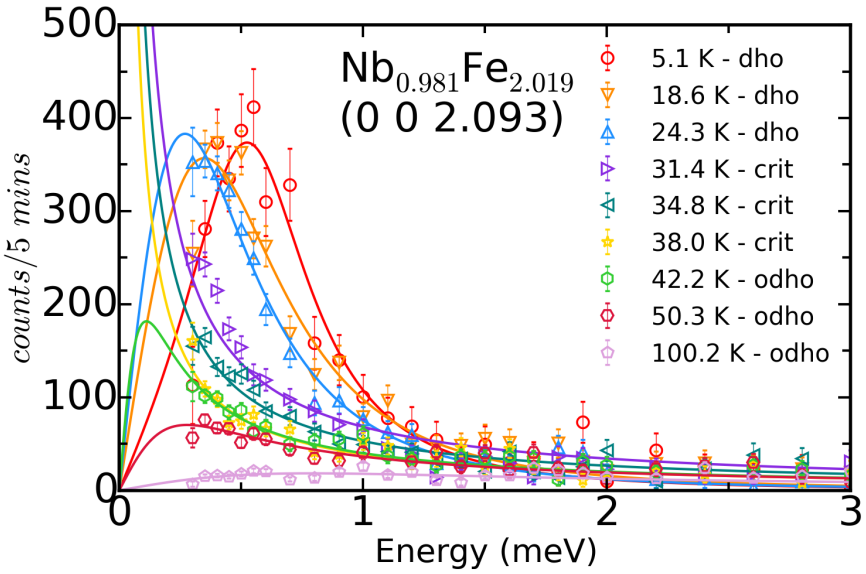


**Figure 4.31:** Temperature dependence of low energy excitations in $Nb_{0.981}Fe_{2.019}$ at the $\mathbf{Q}_{SDW}$ position of (0 0 2.093). The low energy spectra are characterised by well-defined excitations at low temperatures. As $T$ increases, the excitations broaden and become weaker. Data has been fitted with damped harmonic oscillator (dho) or over-damped harmonic oscillator (odho) models, the latter at times in the $\Gamma \to 0$ limit (crit.)

Figures 4.31 and 4.32 contain the equivalent temperature dependence of the low-energy spectra, however now at the $\mathbf{Q}_{SDW}$ position. The behaviour at this position is qualitatively similar to the spectre at $\mathbf{Q}_{FM}$ . In the low temperature FM phase, damping is larger and $\Gamma$ therefore smaller at the $\mathbf{Q}_{SDW}$ position. Looking at the high temperature paramagnetic regime, we find the reverse situation, with $\Gamma$ being smaller at the $\mathbf{Q}_{FM}$ position.

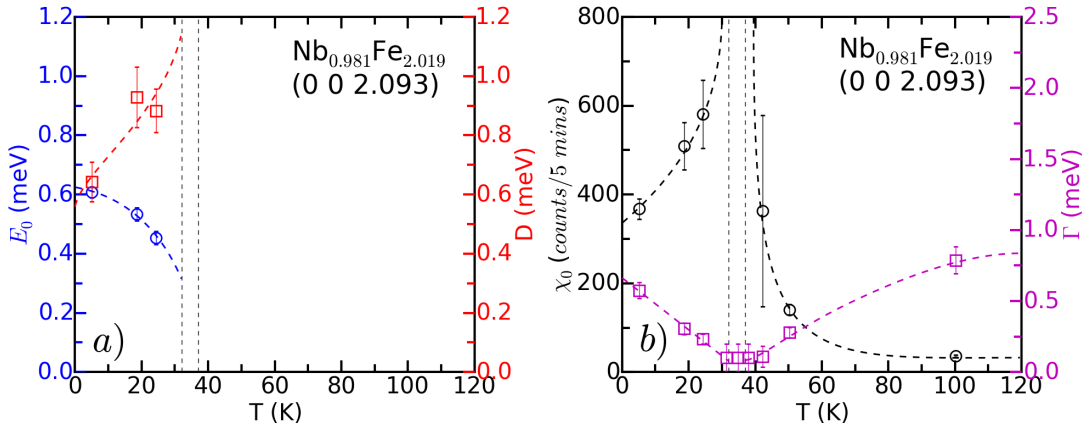


**Figure 4.32:** Fit parameters characterising the $T$ dependence of the low energy excitation spectra at (0 0 2.093) in $Nb_{0.981}Fe_{2.019}$. Parameter obtained via fits using the damped harmonic oscillator (equation 4.5) and the over-damped harmonic oscillator (equation 4.6) models. (a) shows excitation energy $E_0$ (blue circles) and damping $D$ (red triangles). (b) shows static susceptibility $\chi_0$ (black circles) and quasielastic line width $\Gamma$ (purple circles). Dashed lines serve as guides to the eye.

### 4.4.4 Discussion

Presented in the section above is significant low-energy scattering, across a wide range of temperatures, in the $Nb_{0.981}Fe_{2.019}$ system. These excitations are generally well described by the damped harmonic oscillator models, discussed in section 4.3.2.

Within the ferromagnetic regime, spectra are dominated by weakly damped excitations with an excitation energy of 0.5 meV. The minimum in excitation energy would be expected at the ferromagnetic ordering wave vector $\mathbf{Q}_{FM}$. However, surprisingly, these excitations present a minimum near the spin density wave ordering wave vector $\mathbf{Q}_{SDW}$ rather than at the $\mathbf{Q}_{FM}$ position, see Figure 4.18.

As the system enters the spin density wave region, the energy gap closes and excitations turn into quasielastic scattering. The results show that the quasielastic line width Gamma is zero within the resolution of the experiment over a considerable $\mathbf{q}$ range, from $\ell$ =2 to $\ell$ = 2.2 r.l.u. at $T_N$. The spin fluctuations found within this range may therefore be considered critical in nature. The inclusion of the $\mathbf{Q}_{FM}$ and $\mathbf{Q}_{SDW}$ positions in this range may be a reflection of the

simultaneous proximity of tuned $Nb_{0.981}Fe_{2.019}$ to FM and SDW order. For values of $\ell > 2.3$, or $h > 0.1$, $\Gamma$ increases beyond 1 meV.

Entering the paramagnetic phase, the low energy excitation spectra continue to be dominated by quasi elastic scattering. As temperature increases, Gamma gradually broadens and reaches values of the order of 0.5 meV at 100 K, even in the region of QFM and $\mathbf{Q}_{SDW}$. Simultaneously, the static susceptibility $\chi_0$ collapses towards higher temperatures.

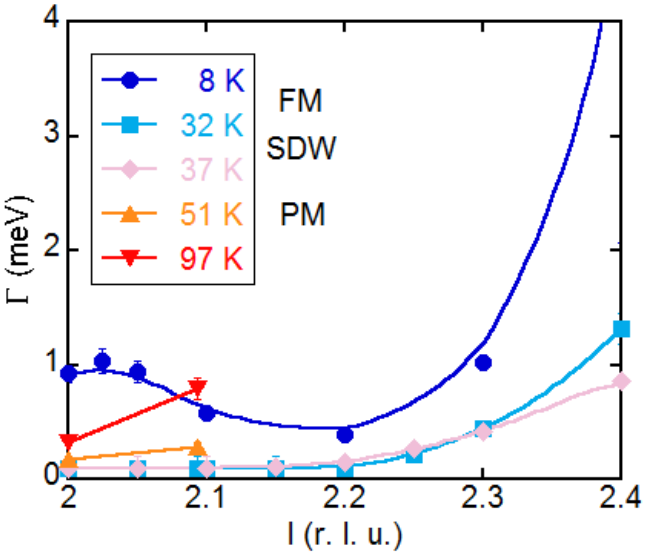


**Figure 4.33:** The **q** dependence of $\Gamma$ over a range of temperatures.

Figure 4.33 shows an overview of the **q** dependence of $\Gamma$ at a number of temperatures. Although $\Gamma$ may only be interpreted as the quasielastic line width in the PM and SDW temperature range, it is always taken as a measure of the damping character of the magnetic excitations. Hence, a reduction in $\Gamma$ describes a transition to a more over-damped regime. Similarly to $E_0$, the minimum of $\Gamma$ is found away from $Q_{FM}$ in the FM state.

The evolution of $\Gamma$ at $T_N$ can be determined by the basic model of ferromagnetic spin fluctuations, as outlined in section 2.3. In order to test this, the **q** dependence of $\Gamma$ is fitted using the formula:

$$\Gamma_{\mathbf{q}} = \gamma(\chi^{-1}\mathbf{q} + c\mathbf{q}^3) \tag{4.8}$$

in the ferromagnetic case, and:

$$\Gamma_{\mathbf{q}} = \frac{\gamma c_1 c_2 \mathbf{q}^3(\mathbf{Q} - \mathbf{q}^2)}{c_1 \mathbf{q}^2 + c_2(\mathbf{Q} - \mathbf{q})^2} \tag{4.9}$$

in the case of ferromagnetism superimposed with a spin density wave (FM+SDW) order case. Here $\mathbf{Q}$ represents a second minimum in the energy dependence of the system. These have been plotted for the $h$ and $\ell$ directions at 37 K, on the border of the PM-SDW transition, see figure 4.34. In both cases the model fits the data with a high degree of accuracy. From the fit of the FM-SDW transition, a $\mathbf{q}$ value of 0.0926 $\pm 1.7\times10^{-3}$ r.l.u may be extracted, which agrees very well with the values published in [39]. Quasielastic scattering above $T_N$ can be seen to follow the standard model of FM spin fluctuations well, however signs of the imminent appearance of a SDW order are difficult to detect due to the resolution of the experiment.

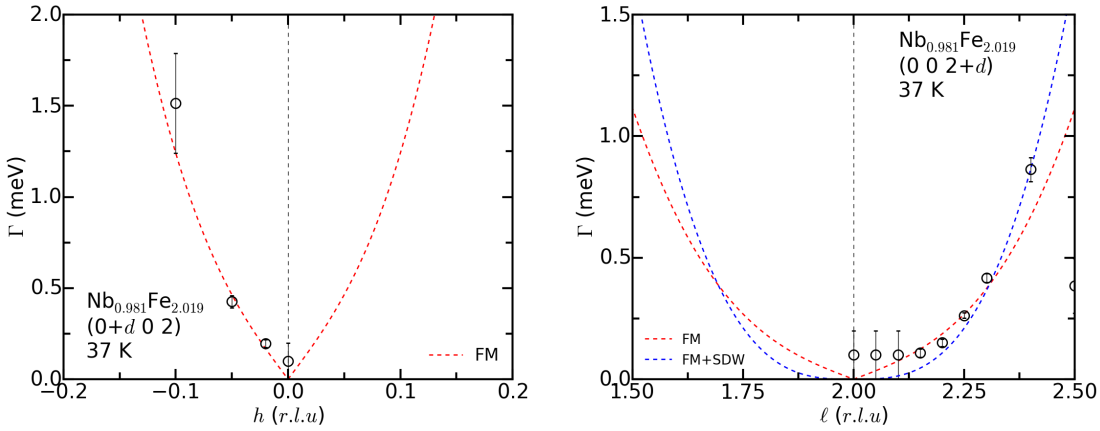


**Figure 4.34:** The $\Gamma(\mathbf{q})$ dependence at $T_N = 37$ K, in the (*left*) $h$ and (*right*) $\ell$ directions. Data fit using the FM and FM+SDW models, eq.4.8 and eq.4.9 respectively.

## 4.5 Conclusion

Neutron scattering has been used to further investigate the border of ferromagnetism in $Nb_{0.981}Fe_{2.019}$, with the aim to develop a better understanding of the interplay between the ferromagnetic order and the spin density wave that emerges

to mask the quantum critical point. The extension of the SDW phase masking the FM QCP at zero field into finite field has been explored. Most importantly, the first low excitation spectra associated with a FM QCP masked by a SDW phase have been obtained.

Magnetic neutron diffraction has been used to map out the location of the spin density wave region, recently identified to mask the ferromagnetic quantum critical point at zero field, in the field-temperature phase diagram. The Fe rich stoichiometry of $Nb_{0.981}Fe_{2.019}$ possesses a $T_N \approx 37$ K and $T_C \approx 32$ K, as has been measured in previous works, [39, 99, 12]. This SDW order was found to reduce significantly with the application of small external fields fields along the easy $c$ axis, suppressing completely at a critical field of $H_C \approx 0.2$ T at $T = 33$ K. As Fe content is increased, it is likely the critical field reduced further as the SDW region is weakened by ferromagnetism of Fe and the system moves closer to a simple FM-PM phase transition beyond the Lifshitz point. A completely different field-temperature phase diagram of $Nb_{0.981}Fe_{2.019}$ is expected for field perpendicular to the easy $c$ axis. In addition to the suppression of the SDW phase the FM phase is also suppressed, albeit on a larger field scale of 2.5 T, allowing for the study of a field-driven unmasked FM-PM quantum phase transition.

Using inelastic neutron scattering, the low energy excitation spectra of the same Fe rich sample, $Nb_{0.981}Fe_{2.019}$, were measured in zero field. The paramagnetic phase is characterised by quasielastic scattering with a minimum at $\mathbf{Q}_{FM}$ even in the vicinity of $T_N$, where one would usually expect to observe the influence of the proximity to SDW order on the spectra.

In the spin density wave phase quasielastic scattering, where $\Gamma$ is less than the energy resolution of 0.1 meV, is seen across a considerable $\mathbf{q}$ range. This covers both $\mathbf{Q}_{FM}$ and $\mathbf{Q}_{SDW}$, strongly suggesting that those spin fluctuation are critical in nature. Despite this, comparison with the spin fluctuation theory for standard FM fluctuations model, as well as that of the combined FM+SDW fluctuations, shows good agreement within the resolution of the experiment. Because of this agreement, one can say that the spectra above $T_C$ do not so far indicate the

presence of SDW order.

The strongest sign of a deviation from the physics of ferromagnetic order is seen in the damped spin-wave excitations within the ferromagnetic state, where the minimum excitation energy of $E_0 \approx 0.6$ meV is observed. Surprisingly, the minimum in the dispersion is located away from the $\mathbf{Q}_{FM}$ position suggesting that the proximity of the SDW order has an influence on the spin waves. It will be interesting to test whether theories of FM QCPs masked by modulated magnetic order, such as those discussed in section 4.1, can account for the unconventional spin wave dispersion observed in the FM phase of $Nb_{0.981}Fe_{2.019}$.

A next important step in the investigation of the low energy excitation spectrum of the $Nb_{1-x}Fe_{2+x}$ system will be to perform high energy resolutions INS measurements to probe the $\mathbf{q}$ dependence of the soft excitations near $T_C$ and $T_N$ using e.g., the spin-echo technique within polarised neutron scattering, to see whether deviations from standard FM spin fluctuation theory can be observed in the $\mu$eV range. Apart from that it will be exciting to obtain excitation spectra in samples with reduced iron content in order to examine the region of the FM-SDW and SDW-PM QPTs. The analysis of such data should provide unique insight into the physics of ferromagnetic quantum criticality.

# Chapter 5

# Exploration of $Cu_2OSeO_3$

The $Cu_2OSeO_3$ system has gained notoriety in recent years for displaying the first skyrmion lattice phase in a large band-gap Mott insulator. As described in Section 5.1 The system crystallises in the same chiral-cubic $P2_13$ space group as the metallic binary helimagnets FeGe and MnSi. In section 5.2 previous knowledge of the system is reviewed. An overview of the various experimental set-ups is given in section 5.3. Section 5.4 then presents results from Raman and Infrared spectroscopy, before section 5.5 explores the crystallographic structure through single crystal and powder X-ray diffraction. The conclusions reached through these investigations are then discussed in section 5.6, along with thoughts on how to progress.

## 5.1 Formation of the Skyrmion lattice phase

Multiferroic and magnetoelectric (ME) materials, in which magnetic and electric properties are directly coupled, have recently gained significant interest in the scientific community due to their potential use in high density storage and energy efficient devises. This interest has inspired numerous theoretical and experimental studies, generating a number of possible mechanisms responsible for governing these effects [100, 101, 102]. More recently, helical spin textures have been found to directly affect the symmetry of charge distribution and magnetically induce

electric polarisation [103], and as such the skyrmion, a novel topological spin texture, is now believed to play a vital role in quantum magneto-transport processes.

The formation of a skrymion phase has been found in binary metallic alloys with B20 structure, namely MnSi [15] and FeGe [18], as well as various pseudo-binary compounds in which the FM metal was substituted such as $Fe_{1-x}Co_xSi$ [17]. Each of these is found to crystallise in the cubic lattice with chiral space group $P2_13$. In these non-centrosymmetric systems, the spin-exchange interactions are composed of two terms: symmetric $\vec{\mathbf{S}_i} \cdot \vec{\mathbf{S}_j}$ (e.g., ferromagnetic) and antisymmetric $\vec{\mathbf{S}_i} \times \vec{\mathbf{S}_j}$, where $\vec{\mathbf{S}_i}$ and $\vec{\mathbf{S}_j}$ represent spins on neighbouring sites. The antisymmetric exchange term, called Dzyaloshinskii-Moriya (DM) interaction, leads to the formation of a helical spin texture with fixed handedness (spin chirality). The application of an external magnetic field is then found to form a skrymion lattice phase, located between the helical and field-induced spin-collinear (ferromagnetic) states, just below the onset of magnetic order. Given the close relation between the structural and magnetic properties of these binary compounds, a number of pressure studies have been performed, to investigate the structural stability. It was found that the suppression of the magnetic order is not accompanied by a structural transition up to 30 GPa [20, 19].

The discovery of multiferroic properties in the insulator $Cu_2OSeO_3$ along with the existence of a skyrmion lattice phase, presents an ideal target for extending the investigation into the link between structural symmetry and magnetoelectric materials. $Cu_2OSeO_3$ crystallises in the same non-centrosymmetric space group, $P2_13$. It attains, however, a far more complex crystal structure as each unit cell contains 8 formula units. Thus far, pressure studies, performed up to 6 GPa, have found no structural instabilities [21, 22]. Therefore, studies have been performed to much higher pressure to determine the structural stability of $Cu_2OSeO_3$ in this extended range.

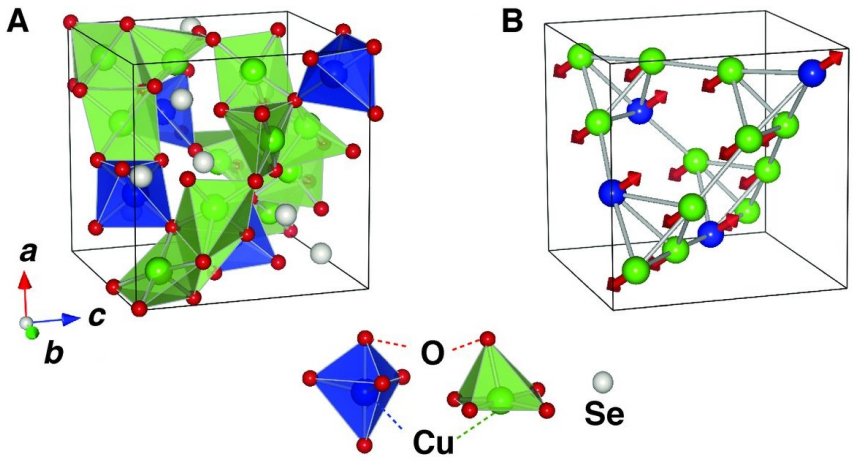


**Figure 5.1:** (a) Crystal structure of $Cu_2OSeO_3$ , characterised by three building blocks, square pyramidal $CuO_5$ (Cu(12*b*)), trigonal bipyramidal $CuO_5$ (Cu(4*a*)), and a lone pair containing tetrahedral $SeO_3$ unit. (b) Ferrimagnetic spin alignment of $Cu^{+2}$ sites [103].

## 5.2 Introduction to $Cu_2OSeO_3$

$Cu_2OSeO_3$ crystallises in the non-centrosymmetric, cubic space group of $P2_13$, first established in ref. [104]. Each unit cell consists of 8 f.u.: 32 O, 16 Cu and 8 Se atoms. The crystal structure comprises a three-dimensional array of distorted corner-sharing copper tetrahedra, in which $Cu^{2+}$ ions occupy two inequivalent sites, those being 4*a* and 12*b*. Oxygen atoms then form distorted polyhedra about these sites, $CuO_5$ trigonal bipyramidal polyhedra about Cu(4*a*) and $CuO_5$ square pyramidal polyhedra about the Cu(12*b*) site. These exist in a ratio of 1:3. The Se atoms then form lone pair tetrahedral $SeO_3$ units [105, 106, 107, 108]. This structure is depicted in figure 5.1.a, with the $Cu^{2+}$ ion network shown in figure 5.1.b. This $P2_13$ structure is observed to remain stable down to 10 K with no apparent structural transition [106]. Evolution of lattice parameters are seen to follow the approximation for bare thermal expansion due to thermal vibrations of a solid as derived in [109] and are dictated by $a(T) = a_0 + A\coth(\theta/T)$.

Initially, at ambient pressure, $Cu_2OSeO_3$ was found to undergo a ferrimagnetic phase transition at $T_c = 58.8$ K, whereupon three ferromagnetically aligned Cu(12*b*) moments pair anti-ferromagnetically with a fourth Cu(4*a*) moment [105,

106]. Bond valence sum (BVS) calculations have been used to confirm the +2 oxidation state of the Cu ions, BVS(Cu($4a$)) = 2.06(2) and BVS(Cu($12b$)) = 2.02(2) [110].

Below $T_C$, the ferromagnetic exchange and Dzyaloshinskii-Moriya (DM) interactions balance to produce a long-period helical magnetic order, with a pitch of ∼70 nm, and a weak anisotropy fixing it along the ⟨100⟩ crystallographic plane [100, 103]. Application of a weak external magnetic field may be used to overcome the inherent anisotropy, unpinning the helices from the lattice and inducing a conical phase above $B_C$. Increasing this field is found to further stabilise a pocket $A$-phase, known as the skyrmion phase, close to $T_C$. Still higher fields then overcome the DM interactions and helical correlations with the system entering a field polarised phase [106]. These features are illustrated schematically in figure 5.2.

Magnetization measurements were used in the construction of the magnetic phase diagram [100]. Here it was found that above a critical temperature of $T_C$ of 58.8 K, $Cu_2OSeO_3$ displays a strong Curie-Weiss dependence, with $\mu_{CW} \approx 1.5\mu_B$/Cu. As field is increased, a faint maximum develops in the vicinity of $T_C$, analogous to the MnSi system in which these maxima arise due to the formation of a skyrmion lattice phase [21], labelled A-phase in figure 5.2. As temperature is decreased, $M(B)$ increases, saturating at $m_s = 0.48\mu_B$/Cu in large fields. Neutron diffraction measurements were then used to identify the emergent helimagnetic, conical and skyrmion lattice phase.

Raman spectroscopy studies performed on the $Cu_2OSeO_3$ system find no structural lattice distortions at temperatures below $T_C$, while at ambient pressure [111]. At 290 K, a total of 84 Γ-point Raman active modes are expected, with 53 of these identified between 0 and 850 cm$^{-1}$ and 21 observed between 850 cm$^{-1}$ and 2000 cm$^{-1}$. Each of these modes display anomalies in their eigenfrequencies below $T_C$, as well as an increase in their integrated intensities. This is attributed to an increase in dynamic polarisability due to contributions from the magnetoelectric effect [111]. Below $T_C$, three new modes appear, at ∼261, 270 and 420

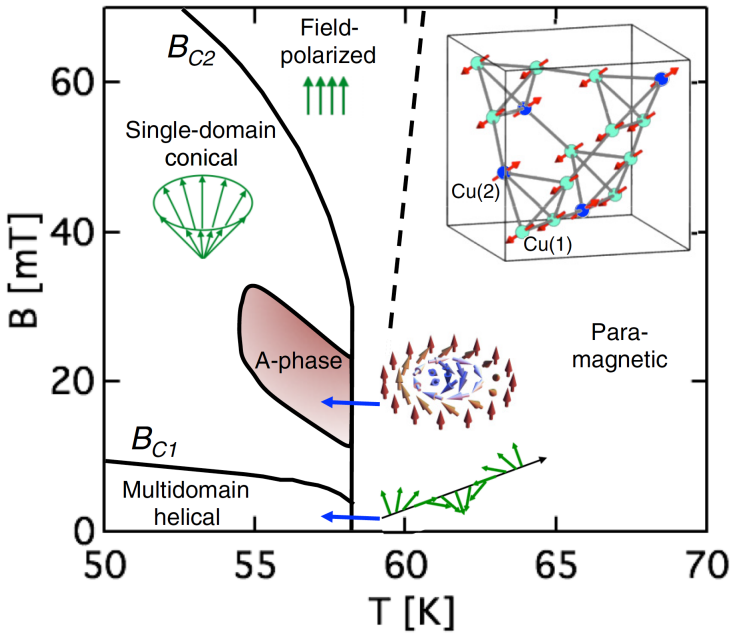


**Figure 5.2:** Schematic representation of the field-temperature phase diagram of $Cu_2OSeO_3$ , illustrating the spin alignments of various phases. The inset shows the crystal structure with the two different $Cu^{2+}$ ion sites [16].

$cm^{-1}$ the explanation being that these modes coincide with a metamagnetic phase transition between two different ferrimagnetic structures which are very close in energy.

The Infrared (IR) reflection and transmission spectra of single crystal $Cu_2OSeO_3$ have been measured between 5 and 300 K, again at ambient pressures, using light spanning from the Far-IR to visible light spectrum [112]. Although no drastic anomalies are found in the phonon spectrum around $T_C$, an anomalous jump in the dielectric constant is observed in its vicinity. Two of the modes exhibiting such behaviour across $T_C$ have been assigned to the motions of oxygen around a central copper, the ion responsible for the systems magnetic order.

## 5.3 Experimental Details

### 5.3.1 $Cu_2OSeO_3$ - Growth and Characterisation

The single crystal $Cu_2OSeO_3$ sample measured in this thesis was grown via chemical vapour transport reaction [113]. A microcrystalline powder was synthesised by reaction of CuO (Alfa Aesar 99.995%) and SeO2 (Alfa Aesar 99.999%), heated to 300° C for 2 days then 600° C for 7 days. This was then recrystallised using a chemical transport reaction in a temperature gradient from 575° C (source) to 460° C (sink) with HCl used as the transport agent. Selected crystals were then characterised using Energy-dispersive X-ray spectroscopy (EDXS), x-ray powder and x-ray single-crystal diffraction, revealing very high quality of crystal [113]. Due to the use of diamond anvil cells, the samples investigated in this thesis are all less than 300 $\mu$m × 300 $\mu$m × 100 $\mu$m in length. The implication of this being that all the samples presented here were taken from an extremely small fragment of a single bulk sample.

### 5.3.2 Raman set-up - I15 Supplementary Lab at Diamond Light Source

Raman measurements were performed using the LabRam HR800 system, see section 3.4.1. Those presented below were taken using the 532 nm laser source at 25% intensity, hole size 100 $\mu$m (laser light aperture) and using the grating with 2400 grooves per mm. Each measurement exposed the sample for 15 minutes with no observable adverse effects. Between each measurement, the cell was left to stabilise at the new pressure for ≈30 minutes.

### 5.3.3 IR - set-up - B22 at Diamond Light Source

For near infrared (NIR) measurements, the internal NIR source of the Bruker FTIR system was used with the lowpass Ge filter removed. The same apertures are used in both the IR and NIR microscope at 15× in transmission mode, along

with the UV-VIS-NIR beam splitter.

Operating in transmission mode provided good quality signal, despite losing the spectral region above 1250 $cm^{-1}$ due to nitrogen impurities in the lower diamond. Background spectra were obtained through a clear region of the DAC sample chamber. The sample and reference spectra ratio well, allowing for the effective removal of all atmospheric peaks and resulting in a clear spectrum. No significant interference fringes were observed in the transmission spectra, ($T = I_{sample}/I_{background}$). Spectra were attained using both a single rectangular aperture above the sample, $\sim$15$\sim$20 $\mu$m, and a "loose confocal" aperture, for which an additional metal plate was placed below the sample plane. This second aperture was set to $\approx$2$\times$ the size of the upper aperture in order to better define the beam at the sample and reduce stray light. Both set-ups were found to produce similar spectra however the "lose confocal" spectra presented higher absorbance values and a generally noisier spectra. This is consistent with the reduction of stray light around the sample and gives a more accurate measure of the true absorbance.

### 5.3.4 Xcalibur

A single crystal $Cu_2OSeO_3$ sample, measuring approximately 0.5×0.5×0.7 mm in size, was mounted to the end of a 0.3 mm diameter glass capillary using a small amount of vacuum grease. The capillary was fixed into a brass holder using wax before being mounted in the goniometer.

### 5.3.5 DAC loadings

The high pressure measurements presented in this section were performed using a verity of DACs and PTMs. In each instance a ruby sphere was used as a pressure marker. The details of each loading are provided in table 5.1. P = plate DAC, M = membrane DAC, LA = leaver-arm DAC. Unless otherwise stated, cells were loaded with Type Ia diamonds.

**Table 5.1:** Details of each diamond anvil cell loading presented in this thesis.

| | DAC | Culet ($\mu$m) | X-ray Energy (keV) | $\lambda$ (Å) | Detector | Pressure Medium | $p_{max}$ (GPa) |
|---|---|---|---|---|---|---|---|
| Raman | LA | 300 | | 5320 | LabRam HR800 | He | 15.78 |
| IR | P | 300[a] | | | Bruker Vertex 80 V | KBr | 14.9 |
| SXRD | P | 300 | 17.997 | 0.6889 | Rugaku Saturn 724 | Meth:Eth | 15.06 |
| PXRD-1 | M | 300 | 29.174 | 0.42499 | Mar345 | He | 10.454 |
| PXRD-2(1) | LA | 300 | 29.197 | 0.429 | P.E. | He | 3.9 |
| PXRD-2(2) | LA | 300 | 29.2 | 0.42481 | Mar345 | He | 10.06 |
| PXRD-2(3) | LA | 300 | 40.996 | 0.30358 | P.E. | He | 14.49 |

[a] Type IIa diamonds

## 5.4 Spectroscopy Results

### 5.4.1 Raman spectroscopy

All Raman spectra, collected for $Cu_2OSeO_3$ , can be seen in figures 5.3, 5.4 and 5.5. Figures 5.3 and 5.4 show spectra taken with increasing pressure, while figure 5.5 shows the spectra taken upon pressure release. Ruby fluorescence peaks remained well defined across all measurement, indicating high quality hydrostatic pressure. Pressure was steadily increased to 15.8 GPa, at which point instabilities were observed in the sample chamber. Pressure was then released to avoid damage to the diamonds. A total of 26 Raman active modes are expected below 900 $cm^{-1}$ , in accordance with observations made in [112]. Of these 26, 17 may be seen in the zero pressure spectra presented in this work.

Figure 5.3 presents Raman spectra between 0 GPa and 9.7 GPa. Closing the cell, there are a number of initial changes to the spectra seen between 0 GPa and 1.7 GPa. All modes are seen to harden, as is expected as bond lengths are reduced. The peak initially observed at $\sim$580 $cm^{-1}$ appears to sharpen, likely due to the initial pressure increase slightly altering the orientation of the crystal and reducing/removing scattering surfaces between the CCD and crystal.

A splitting of the mode located around $\sim$500 $cm^{-1}$ is observed in the 2.3 GPa spectrum (indicated by the arrow in fig.5.3). It is likely that the initial width of the peak, seen at ambient pressure, is due to the presence of several peaks in close proximity. With increasing pressure, these peaks harden at different rates, allowing them to be resolved separately and meaning that by 3.4 GPa there are two distinct peaks. The higher frequency peak continues to harden as pressure is increased while the lower frequency peak broadens (possibly splitting again) and is gradually suppressed.

A second split occurs in the $\sim$600 $cm^{-1}$ mode between 5.0 and 5.4 GPa (arrow in fig.5.3). At 5 GPa a slight shoulder can be seen on the left of the peak. This then shifts to become a distinct peak by 5.4 GPa. At 7.7 GPa the higher frequency mode seems to have been further suppressed in intensity. The broadening

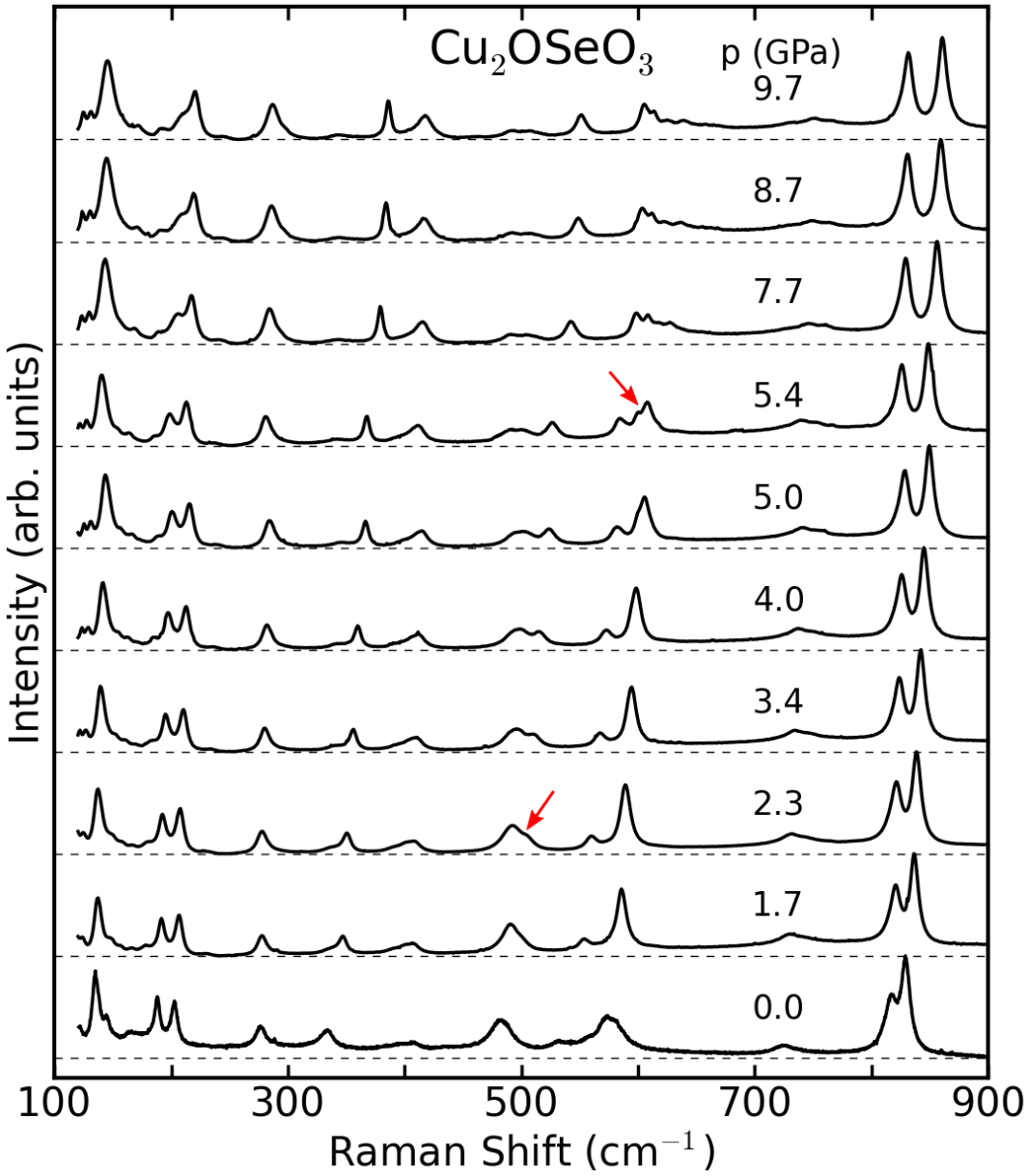


**Figure 5.3:** Raman spectra of $Cu_2OSeO_3$ upon pressure increase, below 9.7 GPa. All spectra are normalised, with respect to the strongest peak for ease of comparison, and shifted vertically with respect to the zero pressure pattern. Dashed lines indicate the baseline for each spectra. Red arrows indicate a pressure-induced splitting of modes.

suggesting the formation of a number of modes that are indistinguishable in this set. Between 5.4 GPa and 7.7 GPa the mode seen at ∼580 $cm^{-1}$ (to the left of the arrow) is seen to suppress suddenly.

Alongside the pressure induced hardening of modes, the sample seems to undergo some form of electronic transition as its bulk color changes from a dark

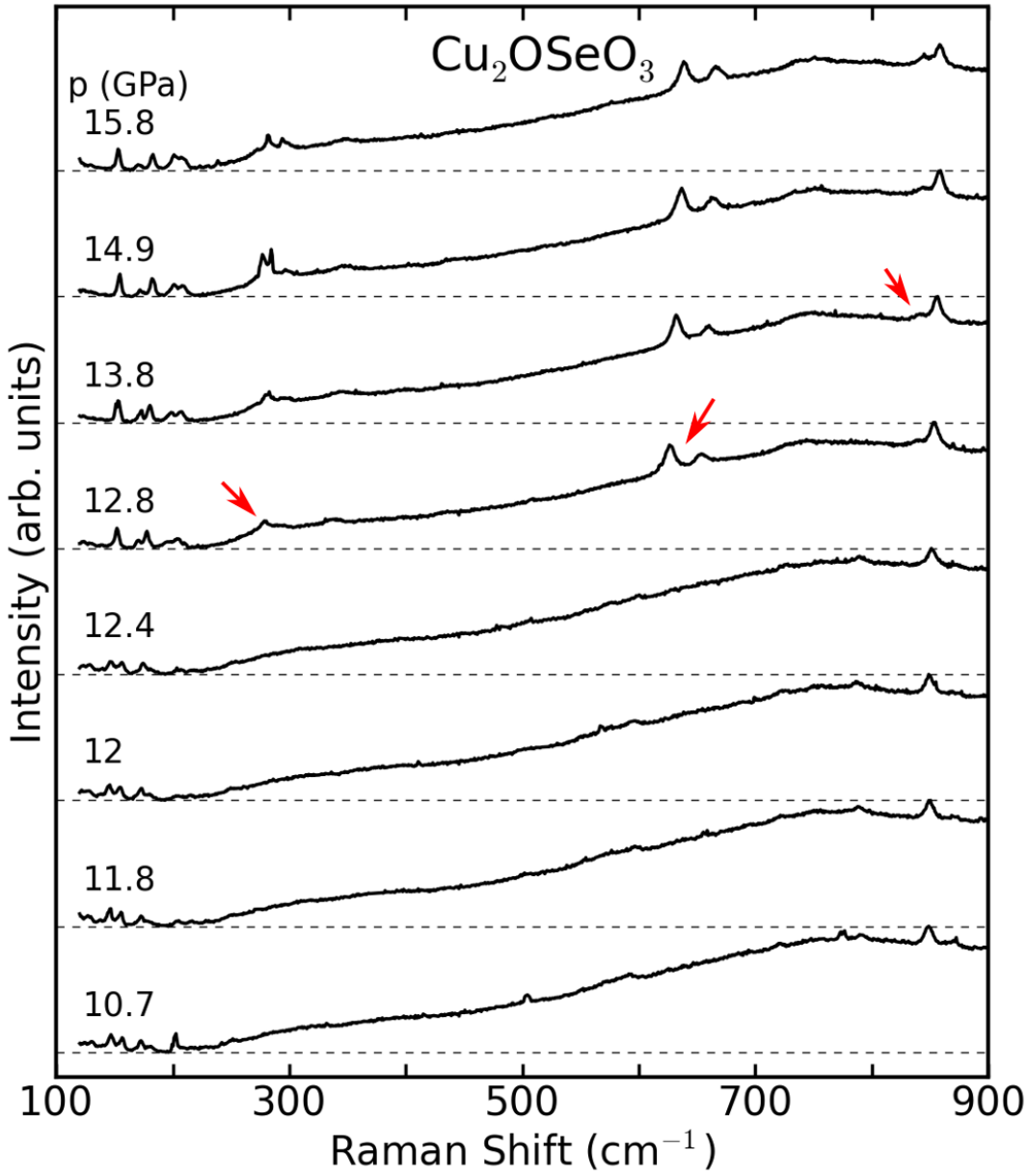


**Figure 5.4:** Raman spectra of $Cu_2OSeO_3$ above 10.7 GPa. All spectra are normalised, with respect to the strongest peak, and shifted with respect to the zero pressure pattern. Dashed lines indicate the baseline for each spectrum.

green to dark red and then to black. This transition begins around 6 GPa, continuing to 9.7 GPa, by which point the sample has become opaque. About this point, the Raman signal decreases considerably, as can be seen in figure 5.4. This is accompanied by a massive drop in intensity in the majority of those modes present in the initial spectra, many being completely suppressed. Under closer inspection however, a number of modes remain detectable, seen below $\sim 250$ cm$^{-1}$ and above 800 cm$^{-1}$ , although it is not clear these bare any relation to modes previously present.

These newly emerged modes then remain relatively static as pressure is increased with little to no increase in intensity. Between the pressures of 12.4 GPa and 12.8 GPa, yet more modes appear, seen around $\sim 280$ cm$^{-1}$ and $\sim 630$ cm$^{-1}$ . These modes however are seen to harden with increasing pressure. The mode visible at 840 cm$^{-1}$ also appears to begin to harden at a more appreciable rate after 12.8 GPa, with the emergence of yet another mode on the lower energy side, indicated by the red arrow in figure 5.4. This mode shows an increase in intensity up to 15.8 GPa, the highest pressure reached in this experiment.

As pressure was released, Raman spectra were taken in order to establish whether the changes observed were reversible, these are shown in figure 5.5. Initially there is very little difference between 15.8 GPa and 9.3 GPa, the new modes soften gradually while maintaining their intensity. Then at 8.0 GPa there is yet another significant transition. Between 9.3 GPa and 8 GPa, the high pressure modes are suppressed completely, along with the higher frequency background reducing in intensity. This is accompanied by the emergence of a new range of strong, well defined, Raman modes. The fact that these modes again do not seem to align with any from the initial zero pressure spectra or any of the high pressure modes is indicative of the formation of a new structure. Reducing the pressure further, there is a general softening of the new modes, as well as a significant increase in intensity of the modes below 200 cm$^{-1}$, apart from mode located at $\sim 185$ cm$^{-1}$, that is almost completely suppressed by 0 GPa. The new spectra remaining down to zero pressure suggests the structure to be metastable. The

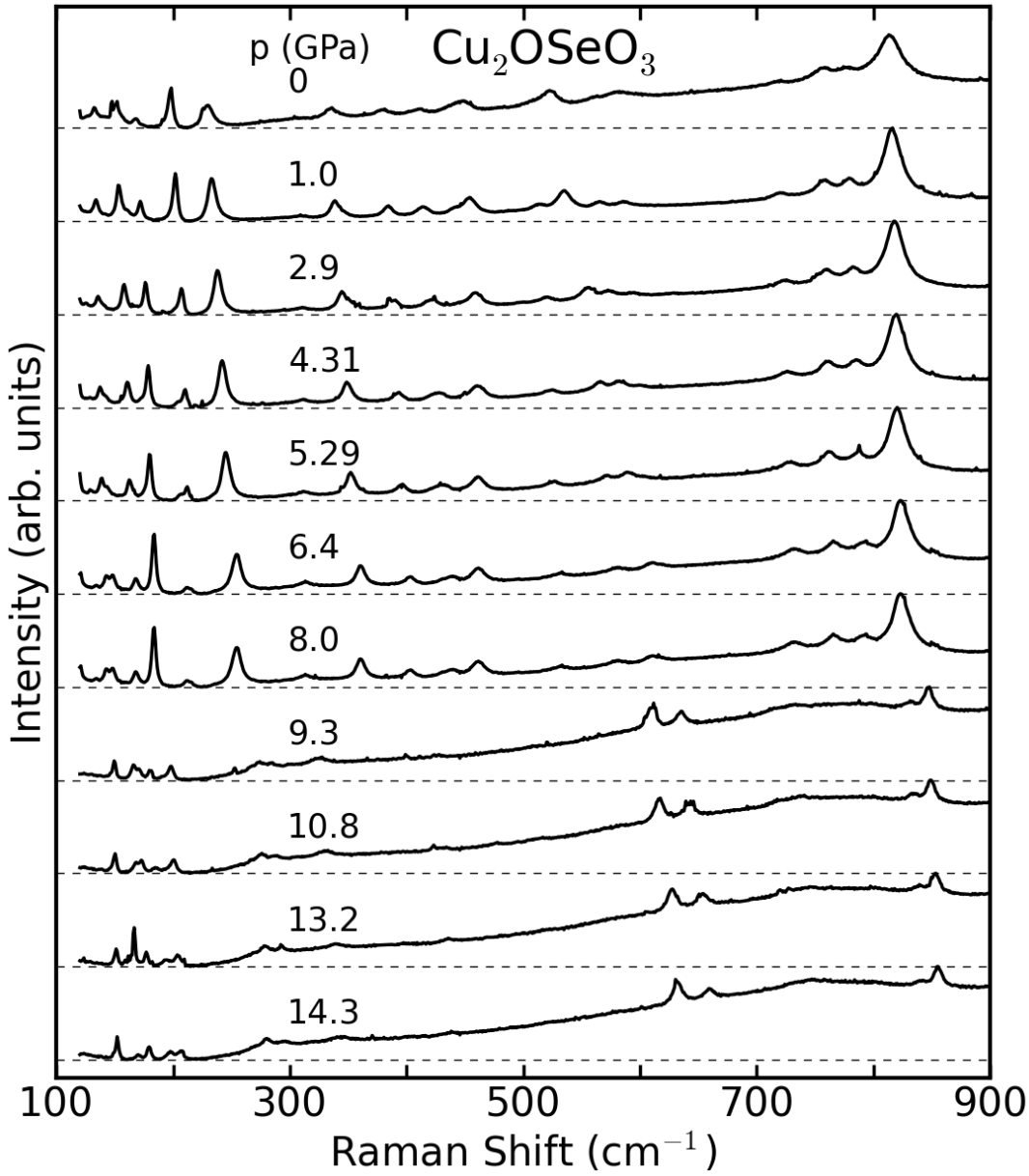


**Figure 5.5:** Raman spectra of $Cu_2OSeO_3$, upon pressure release. Between 9.3 GPa and 8.0 GPa a distinct new phase emerges, indicating a structural to a new low-pressure phase. Dashed lines indicate the baseline for each spectrum.

cell was then left over night and the sample remeasured to check the stability of this new phase; this measurement relieved the same new spectra.

A direct comparison between the initial and final zero pressure spectrum, see figure 5.6, shows a clear difference and strongly suggests a previously unknown structural phase. The crystal remains darker than its initial green colour, however

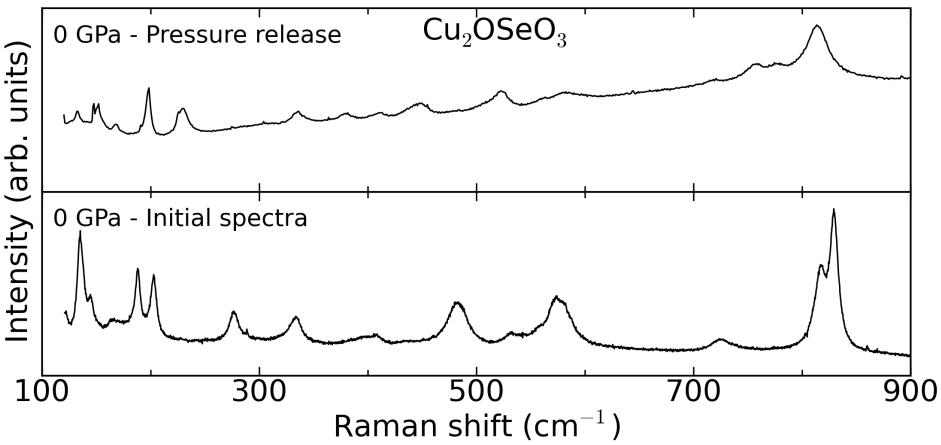


**Figure 5.6:** Raman spectra of $Cu_2OSeO_3$ at ambient temperature. The bottom graph depicts the initial spectra while the top shows the spectra after pressure release.

is no longer completely opaque. There are 15 modes visible, although the majority of these are broad with distinct shoulder features, suggesting a far greater number of unresolved modes. At lower frequencies we see 6 sharper peaks, none of which correspond to those observed in the initial spectra.

To clearly map the evolution of each Raman mode, estimate frequencies are plotted as a function of pressure in figure 5.7. The rate at which each mode shifts has been calculated along with their corresponding Grüneisen parameters. These have then been colour coded in order to more clearly see the rate at which modes shift with $\gamma < 0.4$ in black, $0.4 < \gamma < 0.6$ in blue and those with $\gamma > 0.6$ in red. The dashed vertical lines indicate significant pressures at which changes in the spectra are observed.

The 17 modes found at P = 0 are initially seen to harden as pressure increases, with the exception of those found at around 400 $cm^{-1}$ which actually soften very slightly. A distinct kink is then observed between 5.0 and 5.4 GPa, with 16 of the now 23 modes decreasing in frequency very slightly. This kink occurs simultaneously to the splitting of the peak at $\sim$ 580 $cm^{-1}$ . Together, these observations would hint at some form of structural change within the unit cell although likely only a very slight one. After 5.4 GPa the modes continue to harden, still at varying rates.

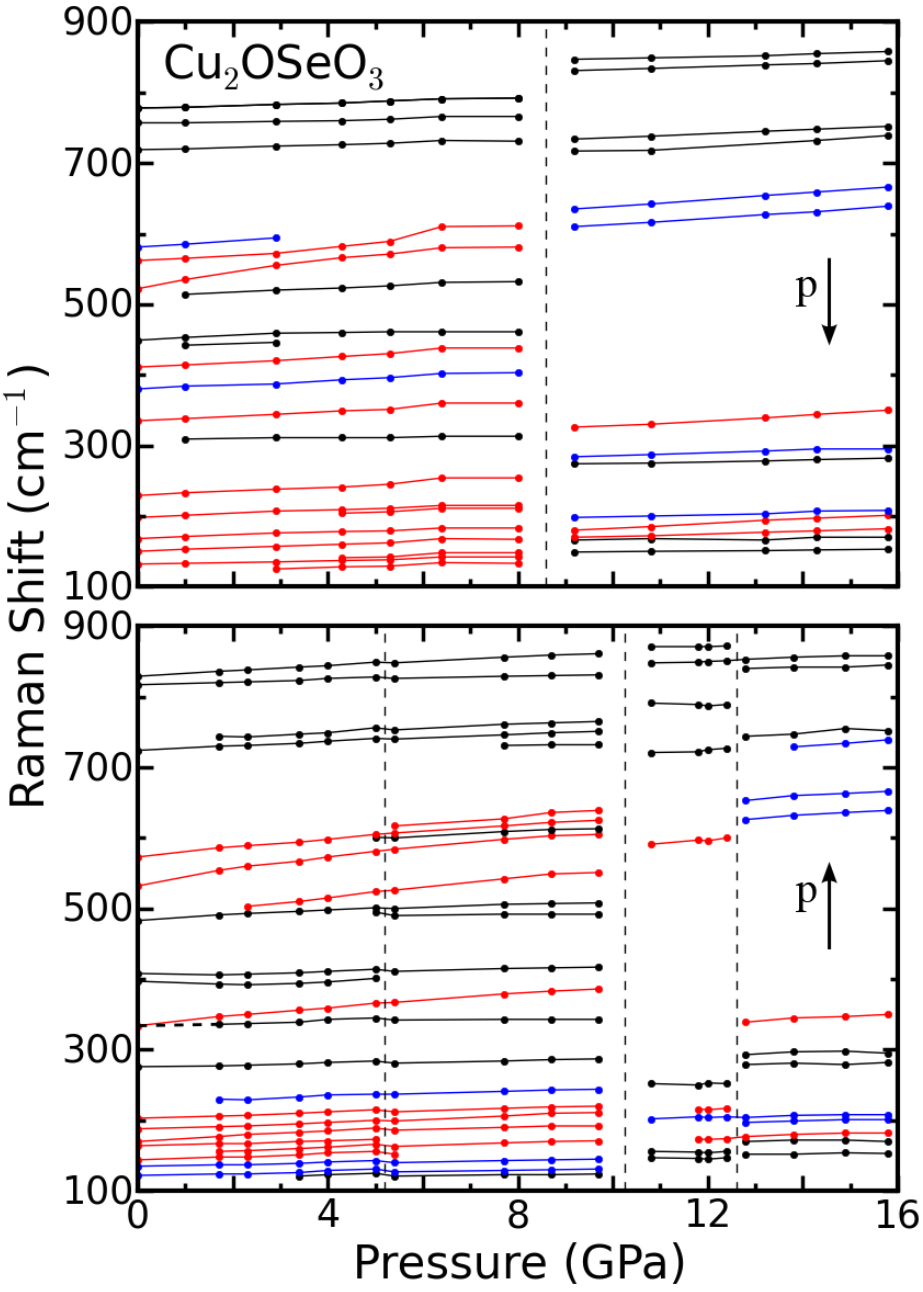


**Figure 5.7:** Raman mode frequencies plotted as a function of decreasing (*top*) and increasing (*bottom*) pressure. Line colour indicates modes with similar Grüneisen values, black being $\gamma < 0.4$, blue $\gamma$ between 0.4 and 0.6 and red $\gamma > 0.6$. Dashed vertical lines indicate pressures of significant change in the spectra.

The transition to a new high pressure phase is clearly visible at $\sim$ 10 GPa, with the newly emerging modes not corresponding to any of those previously observed. This is can only be interpreted as some form of structural transition,

although it at this time it is not possible to say whether this is to a new structural phase, or simply a destruction of the current one. A third change in the spectra is then observed at $\sim$ 12.4 GPa, with the emergence of yet more new modes, which persist up to the maximum pressure of 15.8 GPa. These modes remained upon pressure release, all of them gradually softening with decreasing pressure. This unknown high-pressure phase then transforms into yet another phase between 9 GPa and 8 GPa, that is stable down to ambient pressure.

The clear changes in Raman spectra, when paired with the colour change of the sample, suggest, at a minimum, that the electronic structure is highly pressure sensitive, while, at the most, that a number of previously unknown structural transitions exist at high pressure in the $Cu_2OSeO_3$ system. The apparent colour transition to opaque black may suggest a closing of a band gap, while the emergence of new structural frequencies hint towards the formation of new inter-atomic bonds and hence a new structure. To further investigate this hypothesis requires two approaches; IR spectroscopy in order to investigate the electronic structure of the system, and X-ray diffraction to probe the structure.

### 5.4.2 IR spectroscopy

The Raman spectroscopy results, presented in the previous section, point towards changes taking place in the electronic structure of the $Cu_2OSeO_3$ system. These pressure induced changes manifest as a change in the appearance of the crystal. Initially $Cu_2OSeO_3$ is a known insulator with a band gap of 2.1 eV [114], hence its green colour. With the crystal shifting to red then black, as pressure is increased, it is possible that this band gap is closing with system making a insulator to metallic transition. This hypothesis requires inspection of the band gap energy, which is performed using IR absorption spectroscopy, under pressure, on B22 at the Diamond Light Source.

#### 5.4.2.1 Data analysis

Far-infrared (FIR) and near-infrared (NIR) absorption spectrum were both analysed using an inverse tangent function:

$$f(\omega) = |m| \cdot \arctan\left(\frac{\omega - \omega_0}{\sigma}\right) + C \tag{5.1}$$

Here $|m|$ refers to the height of the edge, $\omega_0$ describes the location of the inflection point in the in the absorbance, $\sigma$ the width of the edge and $C$ is an offset. See figure 5.8.

For many of the NIR spectra the detector became over saturated beyond $\sim$10000 cm$^{-1}$ , due to reaching the upper limit of the detector. Therefore, before fitting, over saturated points were removed and the remaining data smoothed with a Savitzky-Golay low pass filter. Rather than simply a moving window of averaging points, the Savitzky-Golay method fits a polynomial to the data in the window and extracts a value from that fit. This method is used to extract underlying trends from high frequency data, removing noise, while preserving features. Once smoothed (blue line in figure 5.8) the spectra is fitted using equation 5.1.

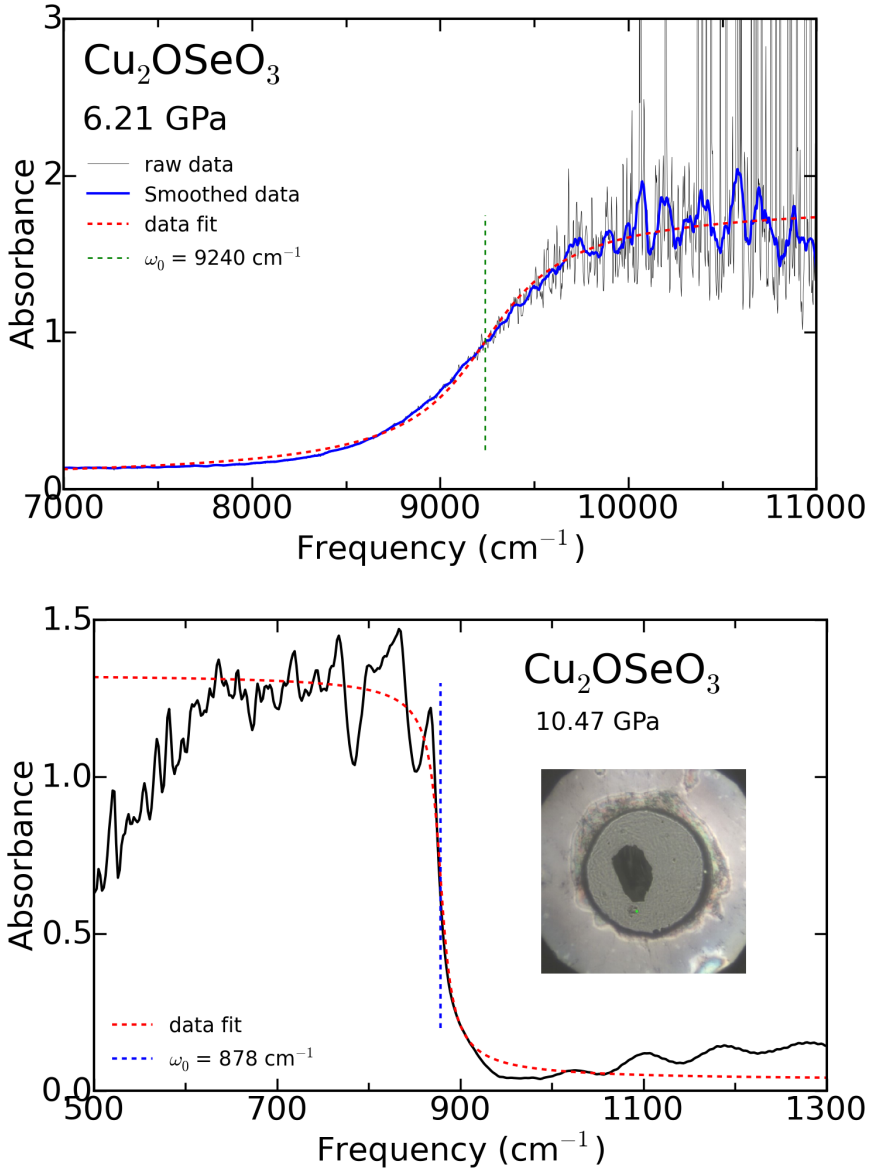


**Figure 5.8:** (*top*) Near-infrared absorption spectrum of $Cu_2OSeO_3$ at 6.21 GPa. Due to detector limits, beyond ∼10000 $cm^{-1}$ , spectra become noisy and over saturated. The data is therefore smoothed using a Savitzky-Golay low pass filter, blue line, before being fitted with eq.(5.1), red dashed line. (*bottom*) Far-infrared absorption spectrum of $Cu_2OSeO_3$ , taken at 10.47 GPa. The spectrum can be described by eq.(5.1). The insert shows the sample in transmitted light at 10.47 GPa. The initially green sample is now black and opaque.

#### 5.4.2.2 Results

Figure 5.9 shows the absorption spectra between 600 and 1200 $cm^{-1}$ , well within the far infrared (FIR) region. Spectra were taken over a range of pressures, between 1.4 GPa and 29.84 GPa, with strong absorbance seen above $\sim$ 950 $cm^{-1}$ in all cases. As pressure increases, there is first an increase in the frequency of the absorbance inflection point, $\omega_0^{(1)}$. Then, between 8.43 and 10.47 GPa, the position of $\omega_0^{(1)}$ jumps to a lower frequency. Further increasing the pressure, to 29.84 GPa, the absorbance edge continues to shift towards higher wavenumber. The discontinuity of the absorption edge coincides with the sample transitioning from a dark green colour to opaque black, as well as with the loss of Raman modes reported in section 5.4.1. From 15.77 GPa the absorption edge is also seen to begin to broaden, transitioning from a well defined sharp feature, to a far more spread out region covering $\sim$120 $cm^{-1}$.

Figure 5.10 depicts absorption spectra for the near-infrared (NIR) region of 7000 to 11000 $cm^{-1}$ . This lies at the upper end of the B22 Bruker Vertex 80 V detector limit, resulting in a high level of noise above $\sim$10000 $cm^{-1}$ . As a result, spectra presented here have been smoothed before the fit is attempted. As pressure is increased there is again a gradual shift in the absorption inflection point towards higher frequencies, which coincides with a smearing of the edge to cover a far larger range of frequencies, $\sim$1500 $cm^{-1}$ . As occurred in the FIR spectra, between 8.43 and 10.47 GPa there is a small drop in the frequency of the inflection point, $\omega_0^{(2)}$. In this instance however, rather than continuing to increase, $\omega_0^{(2)}$ remains almost constant up to 15.77 GPa before beginning to decrease.

These observations are summarised in figure 5.11, where the resulting fitting parameters are plotted as a function of pressure. The pressure dependence of the $\omega_0^{(1)}$ and $\omega_0^{(2)}$ values, figure 5.11.a & b, clearly shows the aforementioned discontinuity at $\sim$ 10 GPa, which corresponds to the disappearance of the all Raman modes (fig.5.7). Whereas $\omega_0^{(1)}$ resumes its increase with pressure, $\omega_0^{(2)}$ remains pressure independent up to $\sim$ 15 GPa. Here $\omega_0^{(2)}$ reverses its pressure dependence and decreases with increasing pressure.

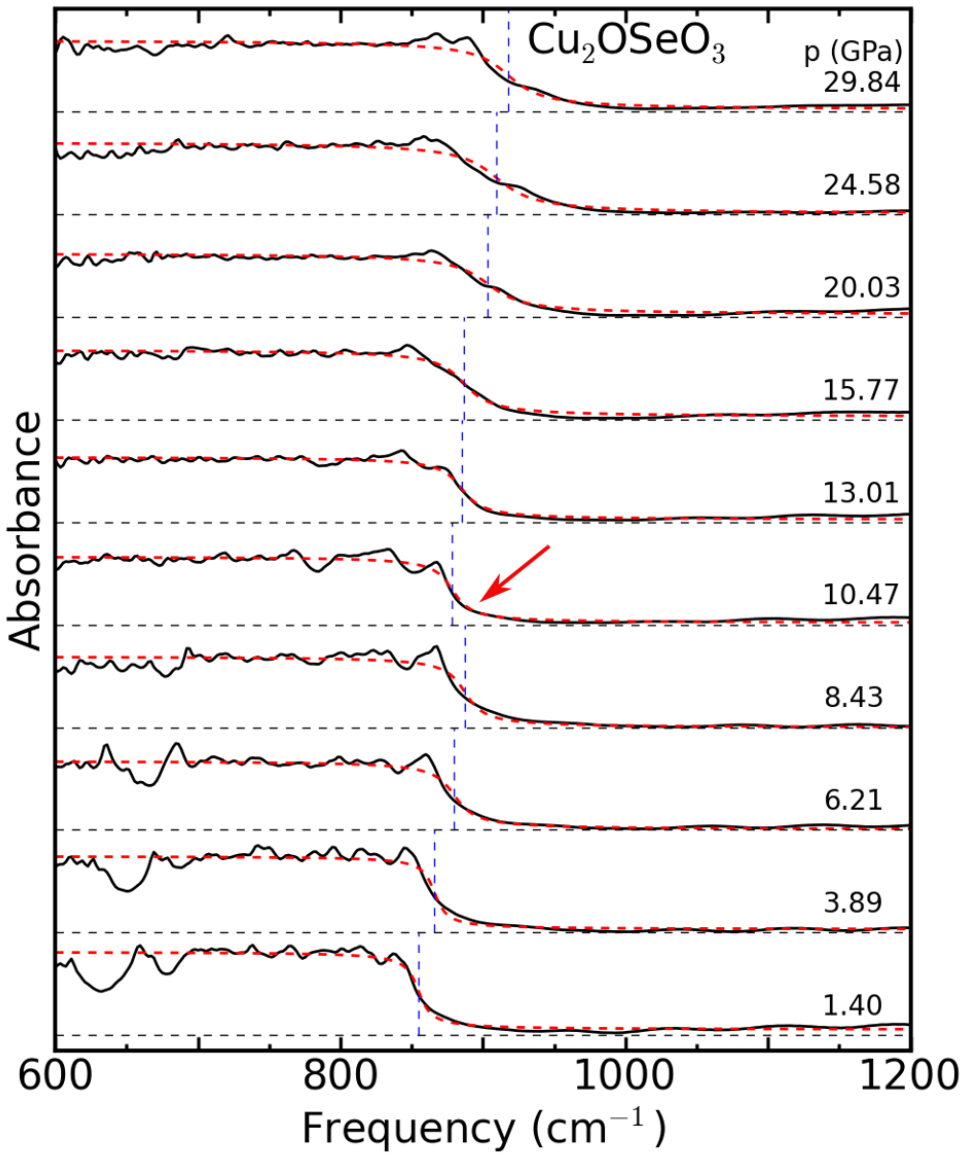


**Figure 5.9:** FIR absorption spectra of $Cu_2OSeO_3$ , upon pressure increase. Horizontal black lines depict data set base lines while vertical blue dashed lines indicate the point of inflection, $\omega_0^{(1)}$. The red arrow highlights the discontinuous decrease in $\omega_0^{(1)}$ frequency.

The absorbency edge "spread", figure 5.11.c), again reveals a number of interesting transitions. The IR values $\sigma^{(1)}$ appear to jump at ∼5 GPa, around the same pressure we observe peak splitting in the Raman data. Then, in the NIR values of $\sigma^{(2)}$, there is a very clear jump at $\sim$ 10 GPa, with values remaining near constant either side of this point. Each of these clear changes in the IR absorption spectra occur at pressures previously highlighted in the Raman data,

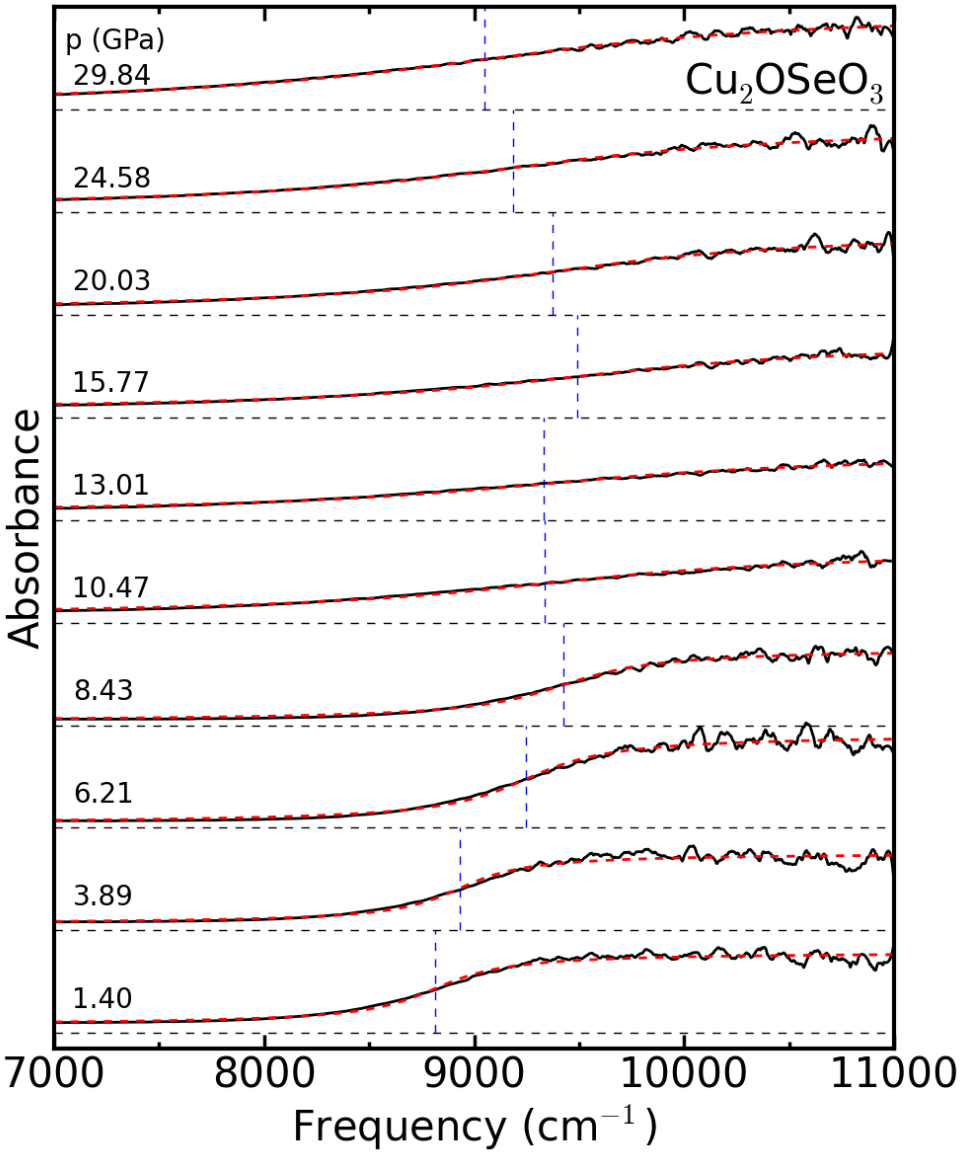


**Figure 5.10:** NIR absorption spectra for $Cu_2OSeO_3$ over a range of pressures. Data has been smoothed, before being fitted with an inverse tan function, equation 5.1. Edge position is indicated by blue dashed lines, $\omega_0^{(2)}$.

suggesting a clear link.

Although the same colour change is observed in the crystal, even at 29.84 GPa the IR spectra shows no significant shift in the absorbance edge towards the mid-IR range. This lack of reduction in the band gap removes any possibility that there is an insulator-metal transition, however, it is evident in the spectra at significant changes are taking place in the electronic structure of $Cu_2OSeO_3$

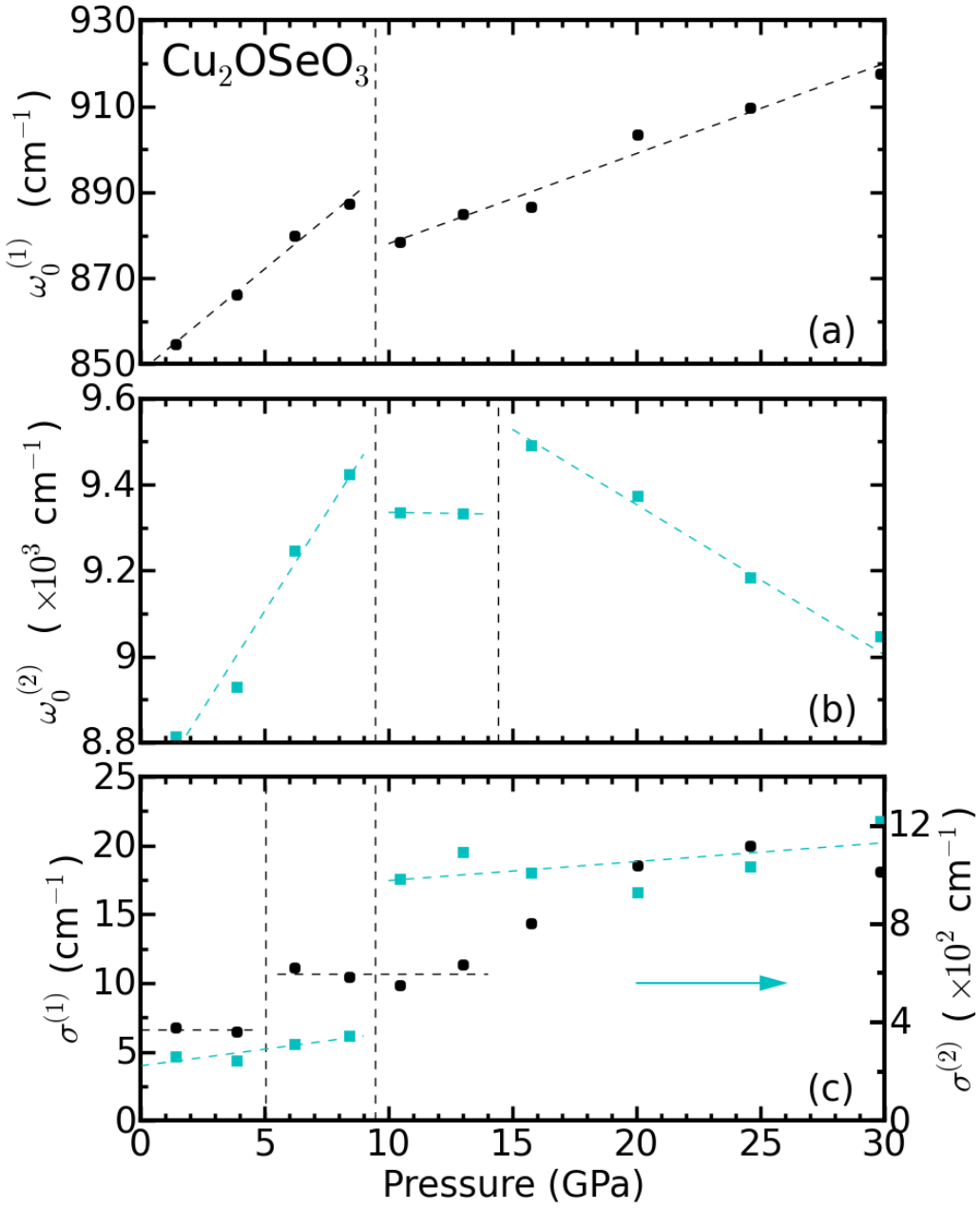


**Figure 5.11:** Pressure dependence of the fitting parameters $\omega_0^{(i)}$ and $\sigma^{(i)}$, i=1,2 (eq.5.1), used in the analysis of the absorption measurements. Discontinuities are indicated via dashed vertical lines, while pressure dependencies are indicated with non-vertical dashed lines.

with increasing pressure. From here, X-ray diffraction measurement are required in order to resolve any structural changes that may be effecting the electronic or magnetic phase of the $Cu_2OSeO_3$ system.

## 5.5 X-ray Diffraction Results

### 5.5.1 Single Crystal results

Interpretation of the Raman and IR results suggest a number of transitions between 0 and 30 GPa. While these may be the result of changes in the electronic or magnetic structures, resulting in the restriction of specific lattice vibrations, it is possible these transitions speak to changes in the crystallographic structure of the $Cu_2OSeO_3$ system. In order to explore this possibility, single crystal X-ray diffraction was performed on the sample, revealing precise atomic positions along with their shift with increasing pressure.

An initial zero pressure measurement was performed using the Xcalibur system at Royal Holloway. The diffraction produced highly symmetric patterns, with strong diffraction Bragg peaks, demonstrating the very high quality of the crystal. There was also no twinning found to be present in the sample, likely due to the very small size of the samples used. The peaks were indexed using the peak hunter process in the CrysAlis$^{Pro}$ software, before being fed into Jana2006 for the final structural determination. The refinements of this diffraction data are presented in table 5.2, with each data set agreeing strongly with positions presented in the literature [107].

A total of 8 pressures were measured using the I19 beamline at Diamond Light Source. These are 0.2, 4.14, 7.95, 8.9, 10.01, 11, 14.8 and 4.58 (pressure release) GPa. Of these pressures, only the first 4 refine to the $P2_13$ structure, with the rest no longer satisfying the required symmetry. This transition coincides very well with the apparent discontinuities observed in both Raman and IR measurements. It should be noted that the observation of diffraction patterns beyond 8.9 GPa suggest a new structural phase rather than simply the destruction of the crystal, with the symmetry of the system reducing significantly.

Those patterns that were able to be refined to the $P2_13$ space group, produce the atomic positions presented in table 5.2. Each of these pressures was able to be refined to a very high level of accuracy, indicated by the very low $R_{int}$ and $R_1$

**Table 5.2:** Atomic position refinements obtained through single crystal X-ray diffraction measurements of $Cu_2OSeO_3$.

| | | **Literature** [107] | | | | **0 GPa** | | | | **0.2 GPa** | | | |
|---|---|---|---|---|---|---|---|---|---|---|---|---|---|
| | | | | | | | | | | $R_{int} = 0.0686$ - $R_1 = 0.0327$ | | | |
| Atom | $W_{pos}$ | $x/a$ | $y/b$ | $z/c$ | $U_{sio}$ | $x/a$ | $y/b$ | $z/c$ | $U_{iso}$ | $x/a$ | $y/b$ | $z/c$ | $U_{iso}$ |
| Cu(1) | 4$a$ | 0.886 | $x/a$ | $x/a$ | 0.01 | 0.8663 | 0.8663 | -0.8663 | | 0.8863 | $x/a$ | $x/a$ | 0.009 |
| Cu(2) | 12$b$ | 0.1335 | 0.1211 | -0.1281 | 0.0084 | 0.1337 | 0.1337 | 0.1337 | | 0.1338 | 0.1213 | -0.1279 | 0.008 |
| Se(1) | 4$a$ | 0.4590 | $x/a$ | $x/a$ | 0.0089 | 0.2114 | 0.2114 | 0.2114 | | 0.4592 | $x/a$ | $x/a$ | 0.008 |
| Se(2) | 4$a$ | 0.2113 | $x/a$ | $x/a$ | 0.0078 | 0.4592 | 0.4592 | 0.4592 | | 0.2115 | $x/a$ | $x/a$ | 0.007 |
| O(1) | 12$b$ | 0.0105 | $x/a$ | $x/a$ | 0.008 | 0.7297 | 0.7297 | 0.7297 | | 0.0108 | $x/a$ | $x/a$ | 0.01 |
| O(2) | 4$a$ | 0.7621 | $x/a$ | $x/a$ | 0.008 | 0.0133 | 0.0133 | 0.0133 | | 0.7622 | $x/a$ | $x/a$ | 0.006 |
| O(11) | 12$b$ | 0.2699 | 0.4834 | 0.4706 | 0.006 | 0.2684 | 0.4844 | 0.4713 | | 0.2698 | 0.4831 | 0.4700 | 0.017 |
| O(12) | 12$b$ | 0.2710 | 0.1892 | 0.0313 | 0.006 | 0.2698 | 0.1894 | 0.0312 | | 0.2698 | 0.1868 | 0.0316 | 0.011 |
| | | **4.14 GPa** | | | | **7.95 GPa** | | | | **8.9 GPa** | | | |
| | | $R_{int} = 0.0511$ - $R_1 = 0.0338$ | | | | $R_{int} = 0.0399$ - $R_1 = 0.0230$ | | | | $R_{int} = 0.0414$ - $R_1 = 0.0296$ | | | |
| Atom | $W_{pos}$ | $x/a$ | $y/b$ | $z/c$ | $U_{sio}$ | $x/a$ | $y/b$ | $z/c$ | $U_{iso}$ | $x/a$ | $y/b$ | $z/c$ | $U_{iso}$ |
| Cu(1) | 4$a$ | 0.8869 | $x/a$ | $x/a$ | 0.023 | 0.8878 | $x/a$ | $x/a$ | 0.011 | 0.8885 | $x/a$ | $x/a$ | 0.01 |
| Cu(2) | 12$b$ | 0.1356 | 0.1232 | -0.1255 | 0.022 | 0.1365 | 0.1258 | -0.1239 | 0.009 | 0.1367 | 0.1265 | -0.1231 | 0.008 |
| Se(1) | 4$a$ | 0.4628 | $x/a$ | $x/a$ | 0.022 | 0.4649 | $x/a$ | $x/a$ | 0.008 | 0.4653 | $x/a$ | $x/a$ | 0.007 |
| Se(2) | 4$a$ | 0.2169 | $x/a$ | $x/a$ | 0.021 | 0.2212 | $x/a$ | $x/a$ | 0.008 | 0.2222 | $x/a$ | $x/a$ | 0.007 |
| O(1) | 12$b$ | 0.0134 | $x/a$ | $x/a$ | 0.021 | 0.0151 | $x/a$ | $x/a$ | 0.01 | 0.0145 | $x/a$ | $x/a$ | 0.008 |
| O(2) | 4$a$ | 0.7632 | $x/a$ | $x/a$ | 0.022 | 0.7635 | $x/a$ | $x/a$ | 0.011 | 0.7645 | $x/a$ | $x/a$ | 0.008 |
| O(11) | 12$b$ | 0.2721 | 0.4859 | 0.4719 | 0.032 | 0.2718 | 0.4895 | 0.4708 | 0.019 | 0.2693 | 0.4888 | 0.4715 | 0.016 |
| O(12) | 12$b$ | 0.2789 | 0.1862 | 0.0364 | 0.024 | 0.2853 | 0.1865 | 0.0396 | 0.012 | 0.2866 | 0.1868 | 0.0397 | 0.010 |

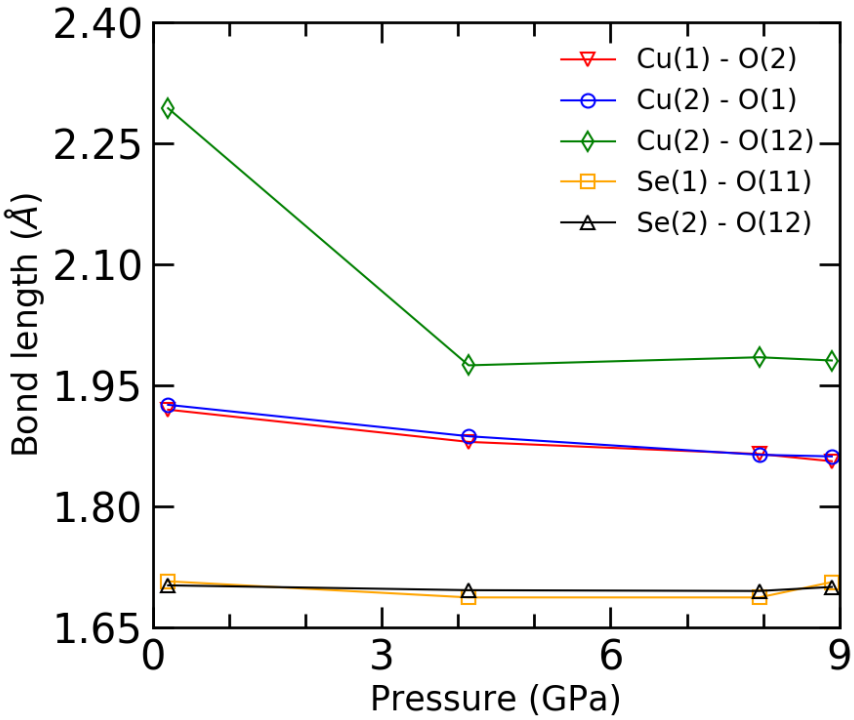


**Figure 5.12:** Atomic bond lengths as calculated from single crystal x-ray diffraction measurements.

values.

These refinements allow for the inspection of a number of key inter-atomic bond lengths, highlighted in [107] as Cu(1)-O(2), Cu(2)-O(1), Cu(2)-O(12), Se(1)-O(11) and Se(2)-O(12), their relative distances plotted in 5.12. Here it is immediately visible that there is a significant reduction in the Cu(2)-O(12) bond length, with a reduction of $\sim$ 0.319 Å between 0.2 GPa and 4.14 GPa, compared to an average reduction of $\sim$0.02 Å as seen in the other bonds. This fairly drastic change suggests an initial significant shift in the internal geometry over the first few GPa as some bonds compress faster than others, this possibly explains the appearance or splitting of peaks in the Raman data. Beyond 4.14 GPa we then observe a slight increase in this same bond length, before again continuing to decrease beyond 7.95 GPa. Another point of note is the slight increase in bond length seen in the Se(1)-O(11) bond between 7.95 GPa and 8.9 GPa. This is possibly indicative of the up coming structural transition.

With this data, it is now clear that there are several previously unknown structural transitions occurring within $Cu_2OSeO_3$ under high pressure. There are clearly a number of more minor shifts below ∼9 GPa shown by the differing rates of bond length reduction, as well as a major structural transition above ∼9 GPa, indicated by the data no longer refining to the $P2_13$ space group. Moving next to X-ray powder diffraction will provide a clearer look at the evolution of the $P2_13$ structure with increasing pressure, as well as enable the identification of any symmetry breaking shifts in the atomic arrangement. Powder diffraction measurements will also facilitate a closer inspection of the newly emergent high pressure phases and provide vital information required to solve these structures.

### 5.5.2 X-ray Powder Diffraction

From the results of the single crystal diffraction, as well as the Raman and IR data, there is clear evidence that $Cu_2OSeO_3$ undergoes a number of structural transitions as pressure is increased. This section presents a series of high pressure X-ray powder diffraction (XRPD) measurements, performed with the aim of determining any significant structural changes.

Figure 5.13 shows a complete Le Bail refinement of two $Cu_2OSeO_3$ diffraction patterns, taken at 0.22 GPa and 9.47 GPa, see section 3.3.4. Here the quality of the refinements are clearly visible, the black line indicating the measured diffraction pattern and the red the calculated refinement. The Topas suite is able to identify the appropriate Miller indices, relating each peak to the appropriate diffraction plane, as well as distinguish those peaks that belong to material surrounding the sample, such as the Re gasket.

A total of 23 pressures were measured, 21 being taken below the suspected structural transition at $\sim$ 9.5 GPa and refining to the $P2_13$ structure with a high level of agreement, $R_{Bragg} < 4$. These are found in figures 5.14 and 5.15. Each data set has had the background removed and been normalised with respect to the (311) peak. In some cases, the use of a polynomial fit in the removal of the background has left some small amount of "waviness" in the data. This was not

present during the refinement of the data and is simply an artefact present in this method of presentation.

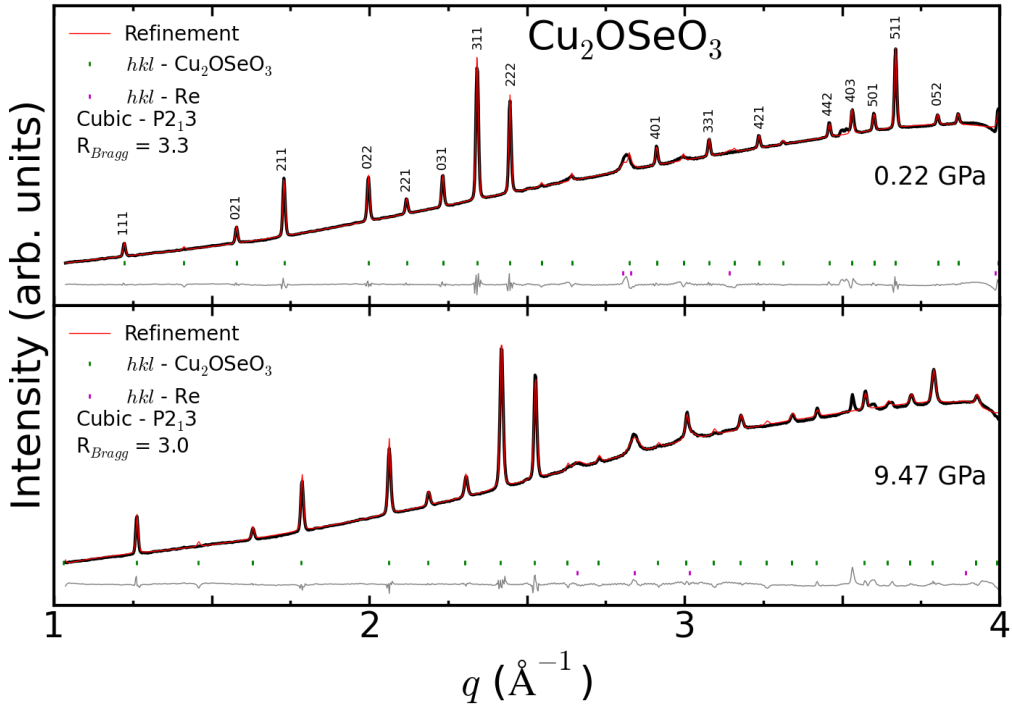


**Figure 5.13:** Le Bail refinements of x-ray powder diffraction patterns at (*top*) 5.905 GPa and (*bottom*) 9.469 GPa. Beam energy is 29.17 keV ($\lambda = 0.424$ Å). This demonstrates the stability of the $P2_13$ structure up to the point of structural transition. In the low pressure refinement (*top*) peaks have been labelled with their appropriate Miller indices.

Figure 5.14 displays powder diffraction patterns of $Cu_2OSeO_3$ below 5 GPa. As is expected, the peaks are seen to shift to higher **q** values with increasing pressure, indicating a shortening of bond lengths and an overall reduction in lattice parameters. Below $\mathbf{q} \approx 3.3$ Å$^{-1}$ the majority of the pattern remains the same, however, in the higher **q** region ($\mathbf{q} > 3.3$ Å$^{-1}$) a number of small changes can be seen. The peak at $\sim 3.5$ Å$^{-1}$ appears to split in to 3 separate peaks at 1.4 GPa, this is accompanied by the emergence of a peak at $\sim 3.6$ Å$^{-1}$ between 0.79 GPa and 1.03 GPa. These new peaks all remain present up to 4.21 GPa, each shifting slightly with increasing pressure.

The emergence of these new peaks in indicative of a reduction in the symmetry

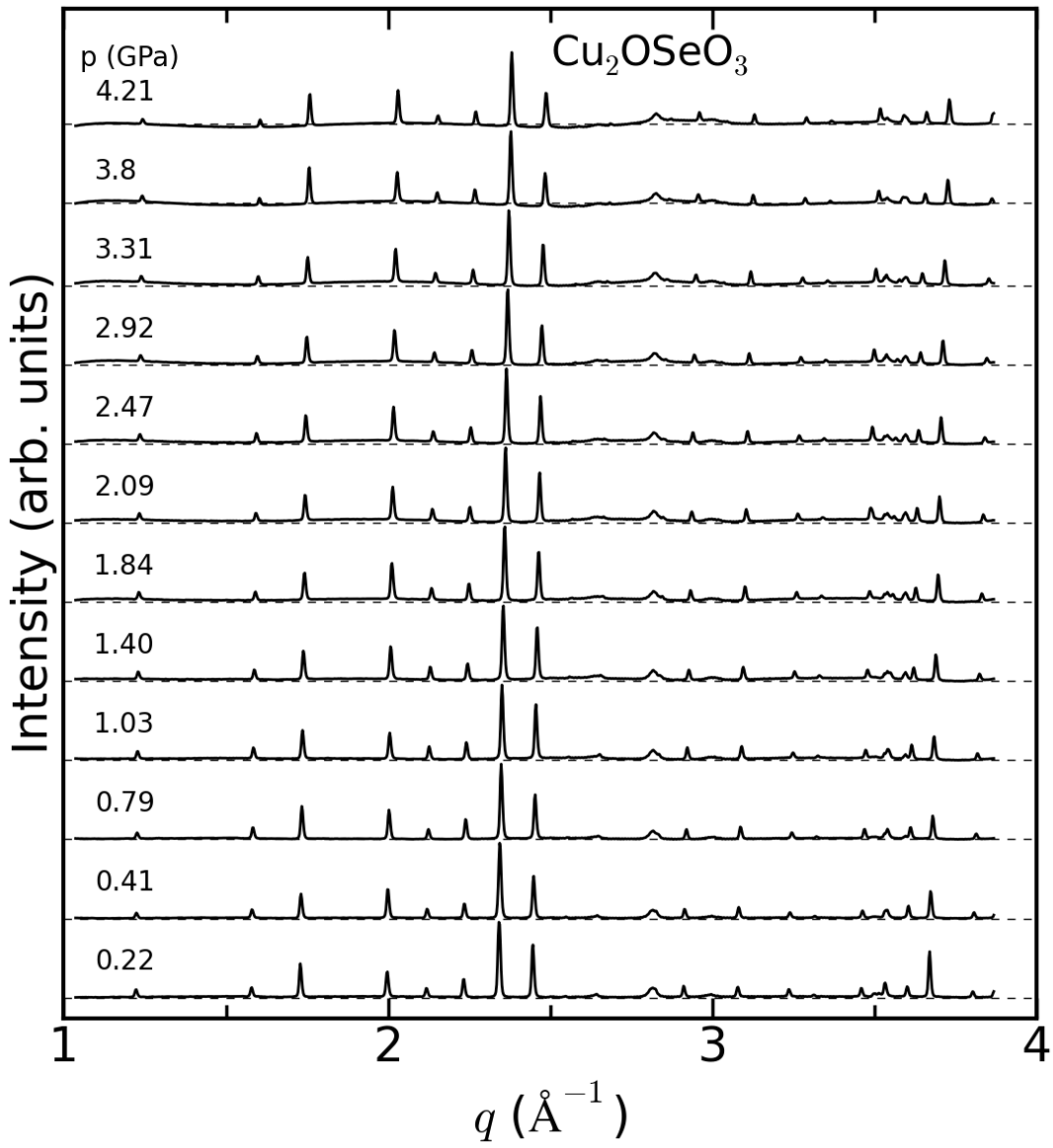


**Figure 5.14:** X-ray powder diffraction of $Cu_2OSeO_3$ with increasing pressure. Beam energy of 29.17 keV ($\lambda = 0.424$ Å). Patterns are normalised to the (311) peak, see figure 5.13, and shifted with respect to the bottom pattern. Dashed lines indicate intensity baselines.

of the system and shows that the $P2_13$ structure does not fully describe the crystallographic structure at higher pressures. This theme is continued in figure 5.15 where again these higher **q** peaks continue to evolve with pressure. At 5.1 GPa there is a sharp spike in intensity of the $\mathbf{q} = 3.5$ Å$^{-1}$ peak. It then remains at a higher intensity up to 7.15 GPa, at which point it splits once again into two

distinct peaks, again lowering the symmetry of the system.

The evolution of these higher **q** diffraction peaks is shown in detail in figure 5.16. Here, it is clear that the $P2_13$ refinement (denoted by the red line) does not account for the newly emerging peaks and various splitting. The low intensity of these peaks, relative to the background, accompanied by the well fitting lower angle diffraction peaks, means Topas is still able to fit the system with the initial structure, with the algorithm giving more weight to the higher symmetry, higher intensity diffractions.

Between 9.47 GPa and 9.91 GPa the system is observed to undergo a significant structural transition, with the resulting diffraction patterns no longer able to refine to the original structure. This transition is again accompanied by the shift in appearance of the sample itself, from a green powder to opaque black. The emergence of this new structural phase between 9.47 GPa and 9.91 GPa fits perfectly with the previously observed transitions in Raman, IR and single crystal diffraction results, confirming the idea of major changes taking place in the internal workings of the $Cu_2OSeO_3$ system. Unfortunately, before pressures could be increased beyond 10.45 GPa, an instability developed in the sample chamber wall, resulting in the loss of the sample as the chamber closed with an increase in pressure. It is clear from these initial findings however that further investigation of the high pressure structural phase of $Cu_2OSeO_3$ is required. Hence the experiment was repeated with this goal in mind. A new powder sample was prepared and loaded as described in section 5.3.5.

Figure 5.17 shows a full pattern Le Bail refinement of the diffraction data to the $P2_13$ space group at 2.1 GPa. The $R_{Bragg}$ value of 2.6 again demonstrates the high quality of the sample and the strong agreement with the $P2_13$ space group that the system possesses. The large, broad peaks observed about $\mathbf{q} \approx 2.6$, $\mathbf{q} \approx 2.8$ and $\mathbf{q} \approx 2.9$ are diffraction from the Re gasket, as indicated. Where appropriate, Bragg peaks are labelled with their appropriate Millar indices. A number of peaks are not visible in the pattern, these are likely lying below the background intensity. This refinement process has been carried out for all pres-

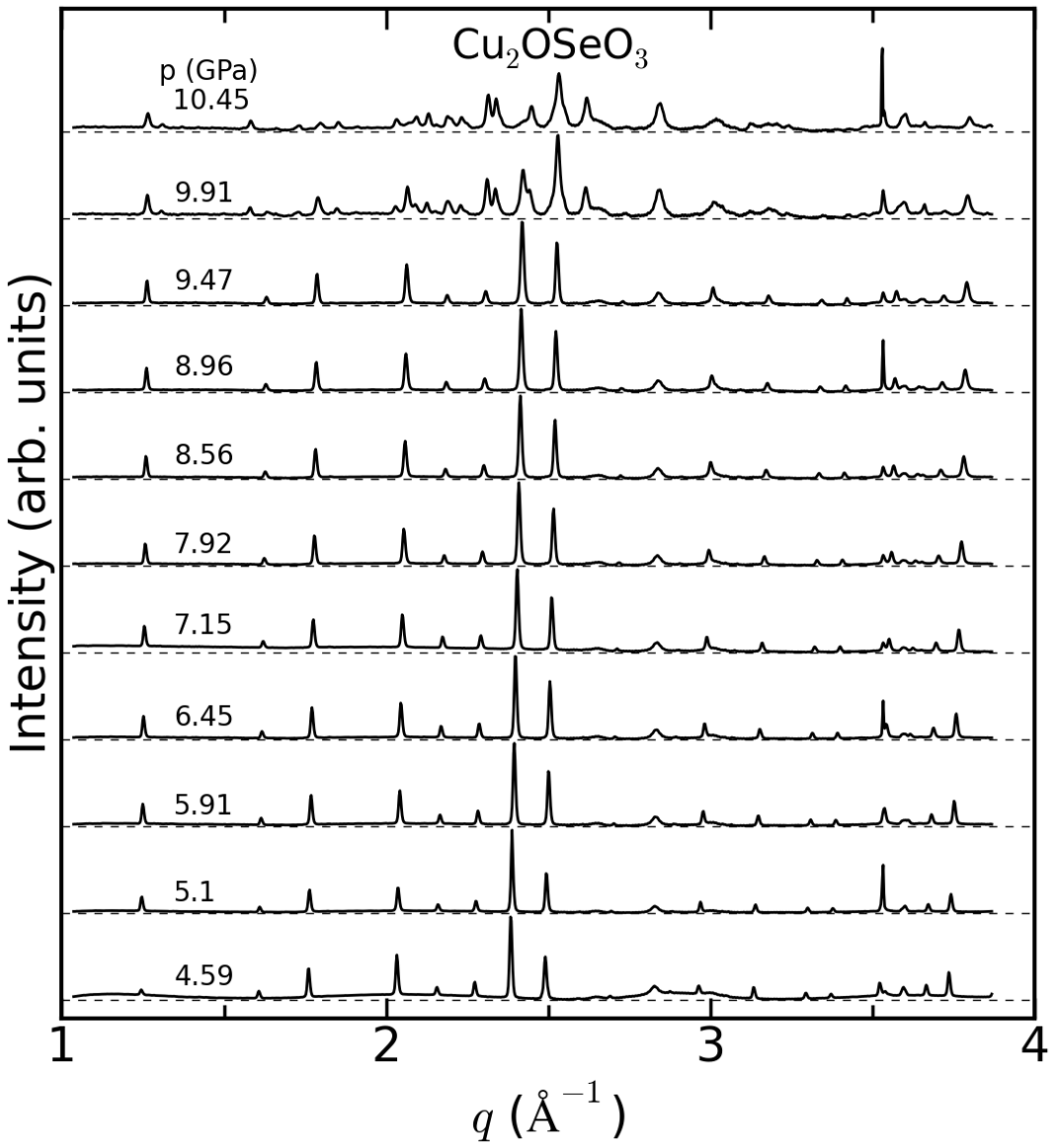


**Figure 5.15:** X-ray powder diffraction of $Cu_2OSeO_3$ with increasing pressure. Beam energy of 29.17 keV ($\lambda$ = 0.424 Å). Pressures between 4.585 GPa and 10.454 GPa. Structure is found to remain stable up to 9.469 GPa. At this point, the system undergoes a structural transition to a new high pressure phase.

sures below 9.65 GPa, all yielding acceptable $R_{Bragg}$ values below 5, indicating the system remains in relative agreement with the $P2_13$ structure. Figures 5.18 and 5.19 display all diffraction data collected, with backgrounds removed. Where possible, the pattern has been normalised to the (311) peak, above 9.04 GPa the data is normalised to the strongest peak present in the data. When appropriate,

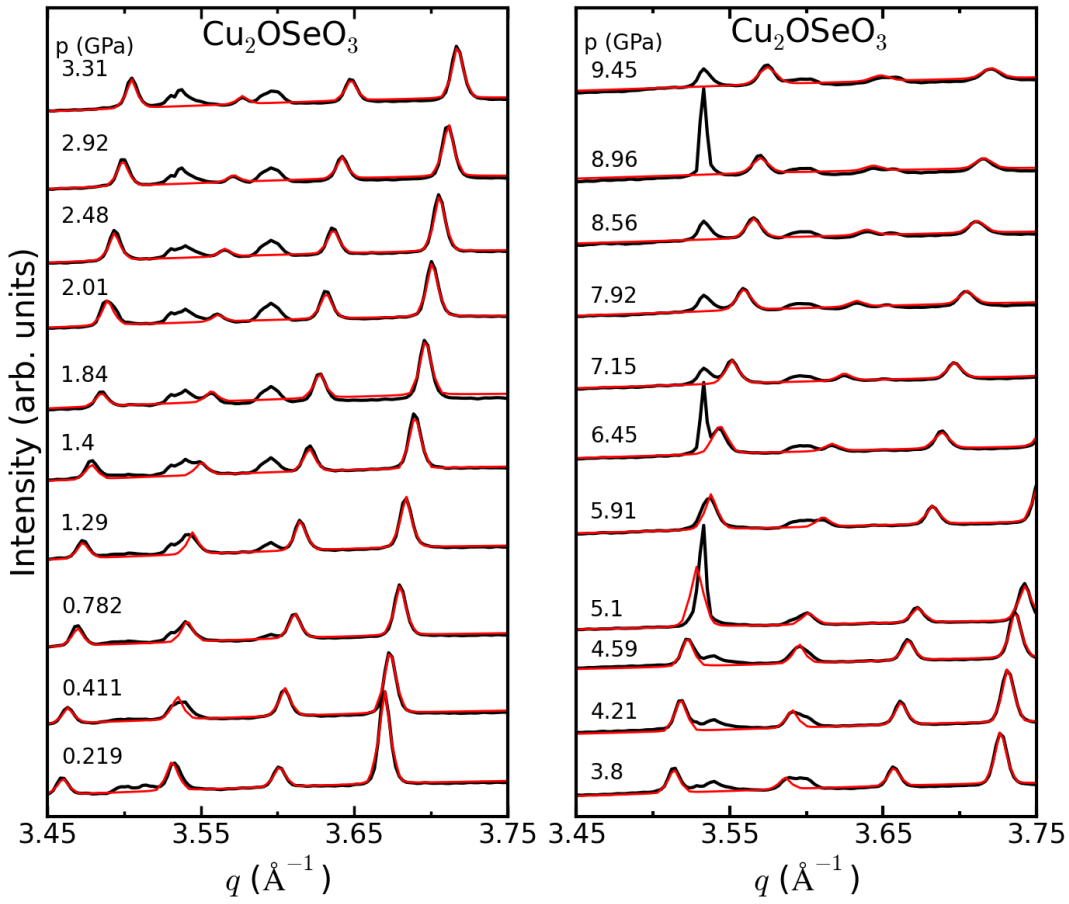


**Figure 5.16:** Inspection of the high $q$ diffraction pattern of $Cu_2OSeO_3$ , with increasing pressure. Red line represents Le Bail refinements. Around 1.4 GPa we see the emergence of a number of new peaks.

Re peaks are marked.

Inspecting closely the patterns displayed in figure 5.18 there are already some interesting points of note. There is a clear split in a number of peaks at 5.19 GPa, located ∼2.25 $Å^{-1}$ as well as around the $\mathbf{q} = 3.5$ $Å^{-1}$ position. The split at the $\mathbf{q} = 2.25$ $Å^{-1}$ position does not appear in any of the higher pressure patterns, likely concealed by the background. The splitting at $\mathbf{q} = 3.5$ $Å^{-1}$ becomes two single low intensity peaks, before returning back to a single peak at 6.13 GPa. At 6.69 GPa we see the emergence of another new peak at $\mathbf{q} \approx 3.6$, this then remains up to 9.04 GPa (see fig.5.19). The addition of these new higher $\mathbf{q}$ peaks again indicate a lowering of the systems symmetry and confirms that the the $P2_13$

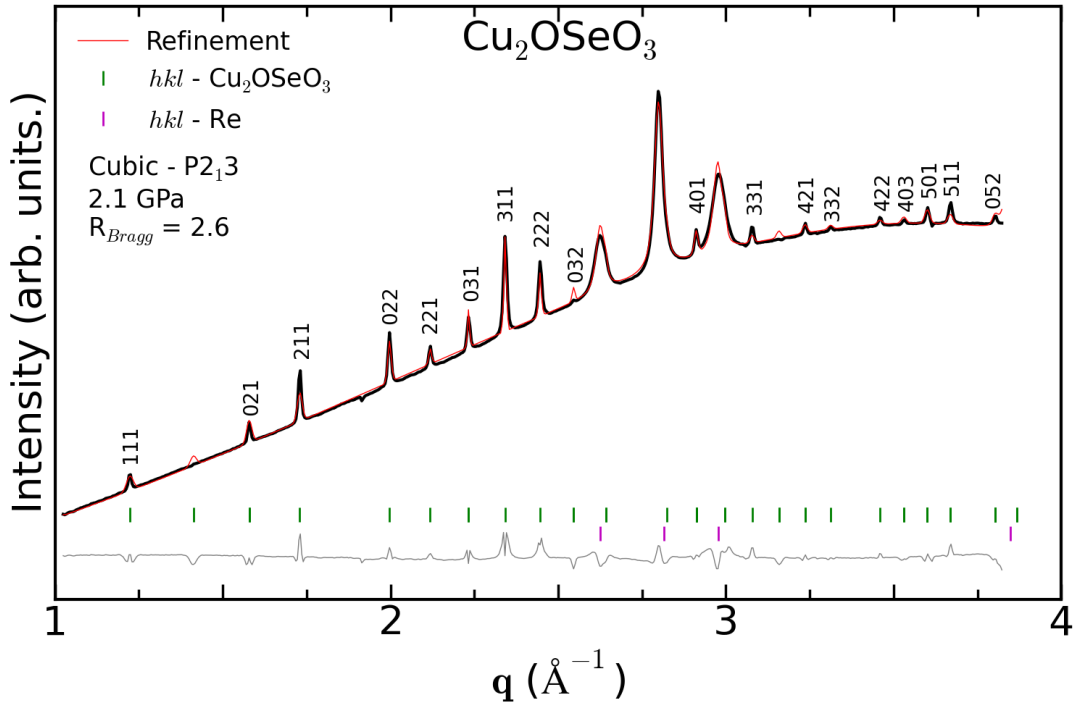


**Figure 5.17:** Le Bail refinement of the low pressure powder diffraction pattern of $Cu_2OSeO_3$ with a beam energy of 29.197 keV ($\lambda = 0.429$ Å). Refinement confirms the $P2_13$ structure.

structure does not fully describe the crystal at higher pressures. The observation of peak splitting at 5.19 GPa coincides with findings in both section 5.4.1 and 5.4.2, in which clear changes in the relative spectra are observed.

Figure 5.19 presents diffraction patterns taken above $\sim$ 9 GPa, along with measurements taken as pressure is released. Looking at these patterns, it is immediately clear that $Cu_2OSeO_3$ undergoes a massive structural transition between 9.04 GPa and 9.65 GPa, with distinct differences visible in the Bragg peaks present in the data. The splitting of the low $\mathbf{q}$, $< 1.75$ Å$^{-1}$, peaks, coupled with the appearance of a number of higher $\mathbf{q}$ peaks, $>3.5$ Å$^{-1}$, indicates a severe reduction in the symmetry of the structure and means the patterns are no longer described by the symmetries of the $P2_13$ space group. This transition, again, perfectly corresponds with the pressures highlighted by the Raman, IR and single crystal data.

This new high pressure structure remains stable between $\sim$ 9.5 GPa and $\sim$

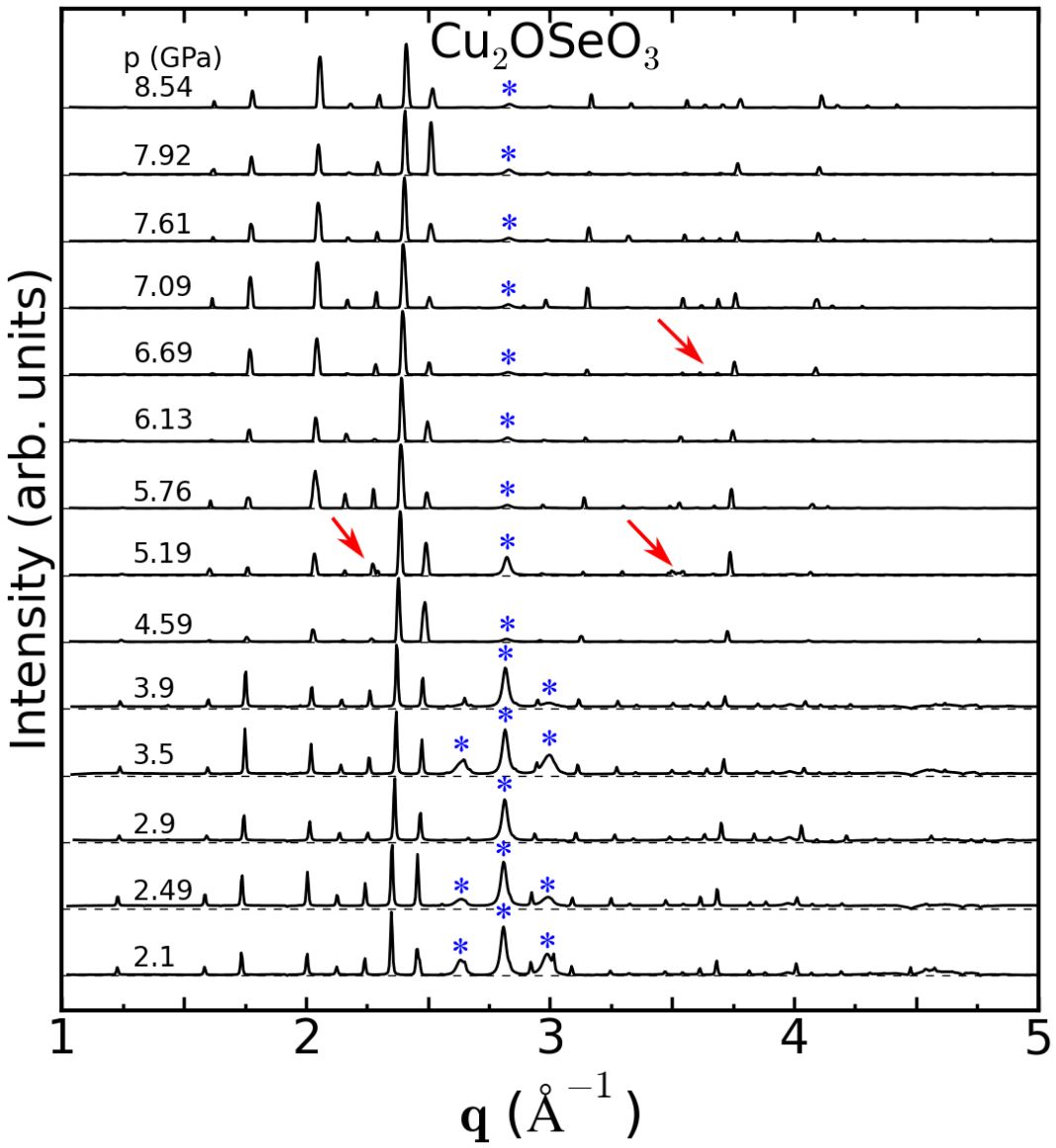


**Figure 5.18:** X-ray powder diffraction of $Cu_2OSeO_3$ with increasing pressure. Pressures 2.1 GPa to 3.9 GPa were measured using the P.E. detector with a beam energy of 29.197 keV ($\lambda = 0.429$ Å). Pressures 4.59 GPa to 8.54 GPa were measured using the Mar345 detector with a beam energy of 29.2 keV ($\lambda = 0.4248$ Å). Re gasket peaks are marked with a blue asterisk'. Patterns are normalised to the (311) peak and shifted with respect the the lowest pattern. Dashed lines indicate intensity baselines for each pressure, while red arrows indicate points highlighted in the text.

11 GPa, with diffraction peaks hardening slightly as is expected. Then, at 11.29 GPa, there is a significant reduction in their intensities, suggesting a breakdown in the long range order and hence the start of the destruction of the crystals. This

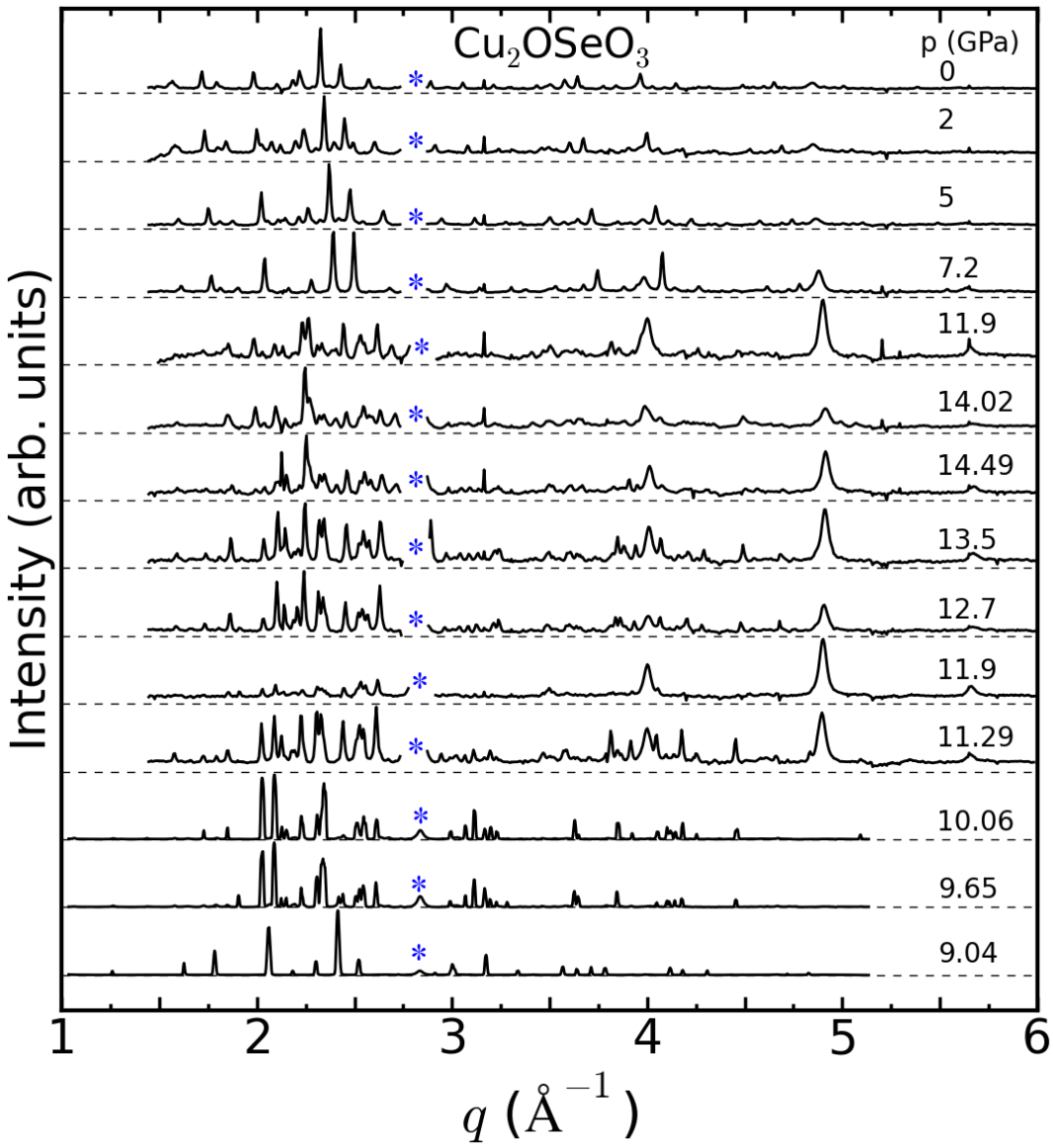


**Figure 5.19:** X-ray powder diffraction of $Cu_2OSeO_3$ . Pressures 9.04 GPa to 10.06 GPa were measured using the Mar345 detector with a beam energy of 29.2 keV ($\lambda$ = 0.4248 Å). Beyond this, patters were taken using the P.E. detector with a beam energy of 40.996 keV ($\lambda$ = 0.30358 Å). Patterns are normalised and shifted with respect the the lowest pattern. Blue asterisk' mark Re peaks, in some instances Re peaks are removed to improve normalisation. Dashed lines indicate intensity baselines for each pressure.

reduction was tracked up to 14.9 GPa, however at this point a crack developed in the culet of one of the diamonds, prohibiting the pressure from increasing any further.

As pressure was released, measurements were performed to see if the system would revert to its original structure. Shown in figure 5.19, the new high pressure phase appears stable between 14.9 GPa and $\sim$ 11.9 GPa. Then, between 11.9 GPa and 7.2 GPa the system undergoes yet another structural transition, with an entirely new regime of Bragg peaks forming. This diffraction pattern show approximately 8 peaks below $\mathbf{q} = 2.5$ Å$^{-1}$, as well as a number above 3 Å$^{-1}$ although there are lower in intensity. There seems to be no correlation between these peaks and those of the original diffraction pattern, confirmed by the fact these new patterns do not refine to the initial $P2_13$ space group. By 0 GPa there is still a clear structure visible in the diffraction pattern which remains distinct from those of the initial structure. This leads to the conclusion that the $Cu_2OSeO_3$ system is now in a third, hitherto unknown, metastable structural phase.

## 5.6 Conclusions

This chapter presents a series of pressure dependent measurement, performed on the $Cu_2OSeO_3$ system and motivated by the existence of novel topological spin textures similar to those found in metallic binary helimagnets (MnSi and FeGe). Pressure studies performed on these binary compounds find the suppression of the magnetic order is not accompanied by a structural transition up to 30 GPa [20]. Previous pressure studies performed on $Cu_2OSeO_3$ find no structural instabilities, however only reach 6 GPa [21, 22]. The use of diamond anvil cells grants this investigation the ability to achieve far higher pressures, the aim being to track the evolution of structure and eventually the magnetic phase of the system.

An initial investigation was performed using Raman spectroscopy, the results hinting towards a number of electronic or structural transition taking place at low pressures, with a significant event around 10 GPa and then possibly around 8 GPa as pressure is decreased. These observations were accompanied by the crystal changing colour, from dark green to red then to black, raising the possibility of an insulator to metallic transition. These results prompted the use of Infrared

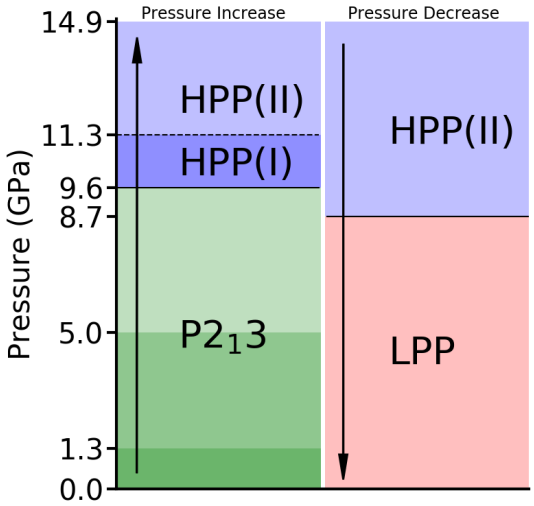


**Figure 5.20:** A tentative sequence of the pressure-induced structural phase transitions in $Cu_2OSeO_3$ The system refines to the initial $P2_13$ phase up to 9.7 GPa, at which point a clear structural transition to an as yet unresolved high-pressure phase (HPP I) is found. Increasing pressure further, a possible second transition is observed around 11.3 GPa, to another high pressure phase (HPP II). With pressure release, the system enters a new meta stable low pressure phase (LPP) at 8.7 GPa, which then remains stable down to ambient pressure. Dashed lines represent possible phase boundaries, while solid lines represent clear structural transitions. The colour gradient in the $P2_13$ phase indicates points of interest present in various results.

spectroscopy to probe the electronic structure of the system, and single crystal X-ray diffraction to ascertain the movement of constituent atoms and check for any changes in the structure. While no band gap closure was observed in the IR data, the single crystal diffraction data reviled a number of surprising shifts in atomic positions, along with a significant departure from the $P2_13$ structure around 9 GPa. In order to further explore the evolution of the structure with pressure, powder X-Ray diffraction measurement were performed. The resulting diffraction patterns presenting a number of minor departures from the original structure at lower pressures, before relieving two significant structural transitions, one at $\sim$ 9.3 GPa as pressure is increased and then one at $\sim$ 8.7 GPa as pressure is released.

Drawing together the results presented in this chapter, it is possible to build a coherent picture describing the affect of pressure on the crystallographic structure

and optical properties of $Cu_2OSeO_3$ . Each set of measurement yields a number of anomalies and discontinuities in their pressure response which correlate with changes observed at the same pressure in other measurements.

As is previously reported in literature, at ambient pressure $Cu_2OSeO_3$ crystallises in the $P2_13$ structure. Single crystal X-ray diffraction measurements were first used in order to confirm this, as well as demonstrate the high quality of the sample and the lack of any twinning.

The introduction of pressure quickly induces a response from the system. Apparent from around 1.29 GPa new high **q** peaks in the powder diffraction patterns, around 3.5 $Å^{-1}$, are seen to emerge, see fig 5.16. Immediately indicating a departure from the $P2_13$ space group and a reduction in the symmetry of the system. Despite the emergence of these new peaks, the diffraction patterns still be refine to the $P2_13$ structure with a very high level of acceptance. Comparing this to Raman spectra taken at similar pressures, the splitting of a single broad mode is observed at 2.3 GPa. This splitting is likely the result of several composite smaller modes shifting at different rates. These different rates of hardening then become apparent in the single crystal diffraction data, in which the Cu(2)-O(12) bond is found to reduced in length far quicker than other bonds.

Further increasing the pressure to $\sim$5 GPa, a discontinuity is found in Raman, IR and single crystal results. In the Raman, a distinct kink is observed in mode positions, figure 5.7, where nearly all modes are seen to soften very slightly at $\sim$5 GPa. This is coupled with further splitting of modes at 5.4 GPa and mode suppression between 5.4 GPa and 7.7 GPa. The IR data presents a slight step increase in the slop of the absorption edge of the NIR spectrum. While the single crystal diffraction data sees the Cu(2)-O(12) bond length to stop decreasing and instead slowly increase. Throughout this pressure increase the high **q** powder diffraction peaks continue to evolve, moving slowly towards lower **q** values. The combination of these results suggest that around 5 GPa there is a slight release in tension, within the $P2_13$ structure, as atoms begin to dislocate from their original positions, in turn allowing for the emergence of new lattice vibrations.

A key result of this thesis is then the major structural transition found at ∼9.7 GPa. At or about this pressure each data set displays significant discontinuities in their results; Raman spectroscopy sees the near complete suppression of all previously visible modes, followed by the emergence several new ones. Infrared data shows a pronounced softening in the absorption edge position, as well as a significant decrease in the edge gradient of the NIR spectra. Single crystal data finds diffraction patterns no longer refine to the $P2_13$ space group above 8.9 GPa. And finally, powder diffractions clearly reviles the emergence of an entirely new set of diffraction peaks, corresponding to an as yet unknown higher symmetry crystallographic structure, here called high pressure phase one (HPP I). This transition is also accompanied by a change in appearance of the sample, from a transparent green to black.

The existence of this structural transition in $Cu_2OSeO_3$ contrasts the structural stability found in the B20 metallic binary systems. In order to develop the understanding of the roll the $P2_13$ space group plays in the formation of the skyrmion phase, this new high pressure structure must be solved and the high pressure magnetic phase diagram mapped out. From this, a deeper understanding of the forces governing the formation of exotic topological spin textures can hope to be established. Unfortunately, this investigation has been unsuccessful in find the identity of this new high pressure phase, and as such this should be made a priority for future work.

As pressure is increased still further the system continues to evolve. In the Raman data, the emergence of several new modes beyond ∼12 GPa is observed, coinciding with the appearance of yet more peaks in powder diffraction data. This may be the the formation of a second high pressure crystal phase (HPP II), or simply the new HPP I phase increasing in quality, revealing more diffraction peaks as long range is order increased. Looking at the IR data, between 10 and 15 GPa the NIR absorption edge remains stationary, after softening slightly following the transition at ∼9.7 GPa. This new HPP II remains up to 15 GPa, the highest pressure achieved in the structural investigation.

Upon pressure release, both powder diffraction and Raman spectroscopy data show the new high pressure phase to remain stable down to ∼8.7 GPa. At this point there is yet another massive structural transition, indicated by the emergence of new Raman modes, as well as a completely new set of powder diffraction peaks. Neither the modes nor diffraction peaks appear to correspond to those present in the initial $P2_13$ phase, indicating yet another previously unknown structural phase, labelled the low pressure phase (LPP). This new structure remains stable down to ambient pressure, indicating a meta stable phase. The crystal remains a far darker, almost opaque appearance. Again, this body of work has been unable to determine the nature of this structure, making classification a priority for any future investigations into the system.

Below ∼9.7 GPa, the $Cu_2OSeO_3$ system could still be refined, with a high level of accuracy, to the $P2_13$ structure. Using these refinements, lattice parameters were established, allowing a $pV$ equation of state to be drawn, figure 5.21. When fit using the Murnaghan EoS (eqn.2.47), combined lattice parameters show a bulk modulus $B_0 = 73.9 \pm 2.5$ GPa. This value is considerably lower than the value of $B_0 = 197 \pm 2$ GPa, published in [21]. The discrepancy in results is likely due to the methods used to calculate lattice volumes, with the previously published value relying on macroscopic changes in sample size, rather than structural data determined through numerous diffraction measurements. Because of this, our value of $B_0 = 73.9 \pm 2.5$ GPa is far more reliable.

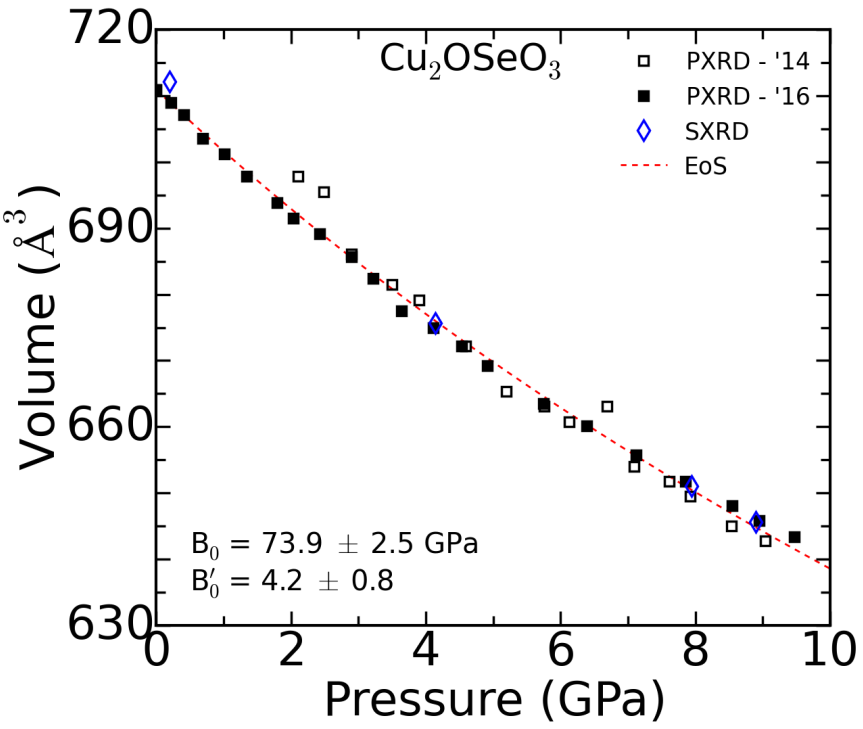


**Figure 5.21:** Volume vs. pressure dependence of $Cu_2OSeO_3$ obtained from powder (PXRD) and single-crystal (SXRD) X-ray diffraction. A fit of a Murnaghan equation of state to the data reveals $B_0$ = 73.9 GPa and $B_0$' = 4.2 for the bulk modulus and its pressure derivative, respectively.

# Chapter 6

# Summary

Magnetic order exists in a vast number of configurations, ranging from simple ferromagnetism to more complex formations such as helimagnetism and topological structures such as the Skyrmion lattice. Magnetic quantum phase transitions play a prominent role in the formation of unconventional and high temperature superconductivity as well as non Fermi liquid behaviour, with compounds displaying these novel states drawing particular attention in recent years. This thesis investigates two such systems, currently of interest for their unconventional magnetic behaviour; the itinerant ferromagnet $Nb_{1-x}Fe_{2+x}$, found to contain a spin density wave domain covering a ferromagnetic QCP, and the insulating helimagnet $Cu_2OSeO_3$, in which a Skyrmion lattice domain forms with the application of small external magnetic fields. These systems have been tuned using temperature, field and pressure, with the aim to develop a better understanding of the conditions that bring about this behaviour.

Neutron scattering was used to investigate the borders of ferromagnetism in the Fe-rich $Nb_{0.981}Fe_{2.019}$ system, confirming transition temperatures of $T_N = 36$ K and $T_C = 30$ K. Magnetic neutron diffraction the established a critical field for suppression of the spin density wave order at $H_C \approx 0.2$ T at $T = 33$ K.

Inelastic neutron scattering was then used to probe the low energy excitation spectra of $Nb_{0.981}Fe_{2.019}$. An overview of $\Gamma(\mathbf{q}, T)$ is shown in Figure 6.1. It was found that the PM phase is characterised by quasielastic scattering, with a

minimum at $\mathbf{Q}_{FM}$ even in the vicinity of $T_N$. In the SDW region quasielastic scattering was observed with a relaxation rate, $\Gamma$, less than the energy resolution of 0.1 meV, suggesting a region of critical spin fluctuations. Finally, in the FM phase, $Nb_{0.981}Fe_{2.019}$ presents damped excitations with a minimal excitation energy of $E_0 \approx 0.6$ meV. As the minimum is located away from $\mathbf{Q}_{FM}$ this suggests that the proximity to the SDW phase influences the excitations in the FM phase. At $T_N$, the relaxation of the systems, $\Gamma$, fits neatly with the basic model of ferro-

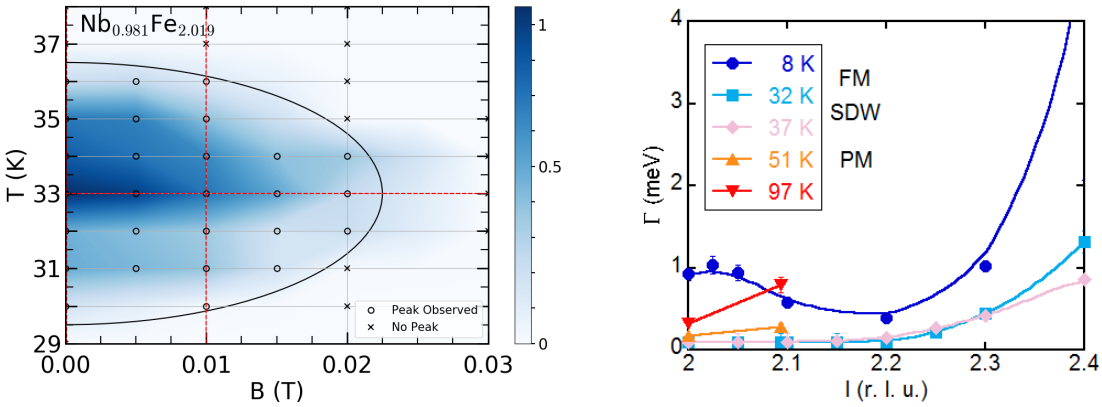


**Figure 6.1:** (*left*) Field-temperature phase diagram of the SDW order found in $Nb_{0.981}Fe_{2.019}$. The position of the diffraction measurements shown in figures 4.7, 4.8 and 4.9 are marked by the red dashed lines. A rough phase boundary, serving purely as a guide to the eye, is shown by the solid black line. (*right*) The $\mathbf{q}$ dependence of $\Gamma$ over a range of temperatures.

magnetic spin fluctuations, as outlined in section 2.3, agreeing with the predicted Landau damping, damped harmonic oscillator model.

Furthering this investigation requires the use of high resolution neutron spectroscopy measurements, e.g. spin-echo experiments, in order to study the detailed $\mathbf{q}$ dependence of soft quasielastic scattering at $T_N$. This ought be accompanied by a detailed characterisation of the spin structures, present in the SDW and FM phases, through polarised neutron scattering. Combined with existing data, this would present an even more complete picture, against which new theories of emerging modulated order at the border of ferromagnetism could then be tested.

In order to understand the rise in magnetic transition temperature, found with increasing pressure in the $Cu_2OSeO_3$ system, the effects of pressure on the

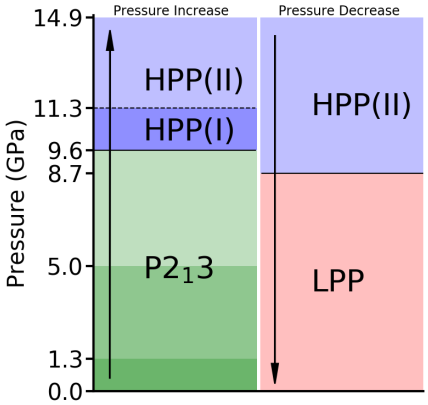


**Figure 6.2:** A tentative sequence of the pressure-induced structural phase transitions in $Cu_2OSeO_3$ . The system refines to the ambient pressure $P2_13$ phase up to 9.7 GPa, at which point we observe a clear structural transition to a still unresolved high-pressure phase (HPP I). increasing pressure further, we observe a possible second transition at 11.3 GPa to another high pressure phase (HPP II). Upon pressure release the system enters a new meta stable low pressure phase (LPP) at 8.7 GPa. This phase then remains stable down to ambient pressure. Dashed lines represent possible phase boundaries, while solid lines represent clear structural transitions. The colour gradient in the $P2_13$ phase indicates points of interest present in various results.

its structural properties have been characterised. This has been achieved through a series of X-ray diffraction, Raman and Infrared spectroscopy measurements.

Data produced by Raman, IR and X-ray studies all yielded various anomalies and discontinuities in their pressure response, indicating several structural phase transitions, figure 6.2. The initial, $p = 0$, structure ($P2_13$) is seen to undergo subtle changes around 5 GPa, before the system enters a new, high-pressure, structural phase around 10 GPa (see figure 5.20). It quickly become clear that the $P2_13$ space group dose not fully describe the structure beyond 1.2 GPa, following the emergence of several new high $\mathbf{q}$ peaks in the PXRD diffraction data and discontinuities in both Raman and IR spectroscopy results. Single crystal diffraction suggests this may be due to irregular shifting of the Cu2, O2 and O4 atoms (fig 5.12). Despite this, the system remains similar enough to the initial structure that reliable atomic positions may still be extracted.

Both powder and single crystal X-ray diffraction results clearly show $Cu_2OSeO_3$ undergoes a significant structural transition at $\sim$9.7 GPa. This transition is again

accompanied by discontinuities in both Raman and IR spectroscopy results, as well as a change in the crystals appearance, from dark translucent green to a deep red then to opaque black. Beyond 11.3 GPa this new high pressure structure appears to break down, the diffraction peaks losing intensity. With the release of pressure, this new high-pressure phase transitions to yet another a new structure between 11.9 and 7.2 GPa. This is most clear in the powder diffraction data, however indications of this transition are also seen in the Raman spectra, characterised by the emergence of new phonon modes.

To continue this work, it is now vital that the new structural phases are identified and assigned to symmetry groups. Once this task is complete, magnetic and electronic measurements are needed in order to characterise the electromagnetic state of the system. This will establish the relation between structural and magnetic composition of the system, hopefully shedding light on the mechanisms that allow for the existence of a Skyrmion lattice domain within this insulating helimagnet in the first place.

# Bibliography


[1] N. D. Mathur *et al.*, Nature **394**, 39 (1998).

[2] S. Lefebvre *et al.*, Phys. Rev. Lett. **85**, 5420 (2000).

[3] Y. Takabayashi *et al.*, Science **323**, 1585 (2009), http://science.sciencemag.org/content/323/5921/1585.full.pdf.

[4] T.-M. Chuang *et al.*, Science **327**, 181 (2010), http://science.sciencemag.org/content/327/5962/181.full.pdf.

[5] R. Daou *et al.*, Nature **463**, 519 EP (2010).

[6] M. Brando, D. Belitz, F. M. Grosche, and T. R. Kirkpatrick, Rev. Mod. Phys. **88**, 025006 (2016).

[7] M. Uhlarz, C. Pfleiderer, and S. M. Hayden, Phys. Rev. Lett. **93**, 256404 (2004).

[8] C. Pfleiderer and A. D. Huxley, Phys. Rev. Lett. **89**, 147005 (2002).

[9] P. G. Niklowitz *et al.*, Phys. Rev. B **72**, 024424 (2005).

[10] D. Aoki *et al.*, Nature **413**, 613 (2001).

[11] A. P. Pikul, Journal of Physics: Condensed Matter **24**, 276003 (2101).

[12] T. D. Haynes *et al.*, Phys. Rev. B **85**, 115137 (2012).

[13] G. Abdul-Jabbar *et al.*, Nat Phys **11**, 321 (2015).

[14] W. Wu *et al.*, Phys. Rev. B **83**, 045106 (2011).

[15] A. Neubauer *et al.*, Phys. Rev. Lett. **102**, 186602 (2009).

[16] F. Qian *et al.*, Phys. Rev. B **94**, 064418 (2016).

[17] W. Münzer *et al.*, Phys. Rev. B **81**, 041203 (2010).

[18] E. Moskvin *et al.*, Phys. Rev. Lett. **110**, 077207 (2013).

[19] C. Pfleiderer, G. J. McMullan, S. R. Julian, and G. G. Lonzarich, Phys. Rev. B **55**, 8330 (1997).

[20] P. Pedrazzini *et al.*, Phys. Rev. Lett. **98**, 047204 (2007).

[21] V. A. Sidorov, A. E. Petrova, P. S. Berdonosov, V. A. Dolgikh, and S. M. Stishov, Phys. Rev. B **89**, 100403 (2014).

[22] C. L. Huang *et al.*, Phys. Rev. B **83**, 052402 (2011).

[23] J. R. Hook and H. E. Hall, *Solid State Physics* (John Wiley & Sons, Ltd, 1991).

[24] C. Giacovazzo *et al.*, *Fundamentals of Crystallography* (Oxford University Press, 2011).

[25] C. Kittel, *Introduction to solid state physics* (John Wiley & Sons, Ltd, 1953).

[26] J. H. Hubbell *et al.*, Journal of Physical and Chemical Reference Data **4**, 471 (1975).

[27] G. Squires, *Thermal Neutron Scattering* (Cambridge University Press, 1978).

[28] S. W. Lovesey *Theory of Neutron Scattering from Condensed Matter* Vol. 2 (Oxford University Press, 1984).

[29] B. Cowan *Topics in Statistical Mechanics* Vol. 3 (Imperial Collage Press, 2005).

[30] J. M. Yeomans, *Statistical Mechanics of Phase Transitions* (Oxford University Press, 1992).

[31] P. Weiss, J. Phys. Theor. Appl. **6**, 661 (1907).

[32] E. C. Stoner, Proceedings of the Royal Society A: Mathematical, Physical and Engineering Science **165** (1938).

[33] K. G. Wilson and J. Kogut, Physics Reports **12**, 75 (1974).

[34] H. E. Stanley, *Introduction to Phase Transitions and Critical Phenomena* (Oxford University Press, 1971).

[35] J. A. Hertz, Phys. Rev. B **14**, 1165 (1976).

[36] S. L. Sondhi, S. M. Girvin, J. P. Carini, and D. Shahar, Rev. Mod. Phys. **69**, 315 (1997).

[37] A. J. Millis, Phys. Rev. B **48**, 7183 (1993).

[38] Q. Si, S. Rabello, K. Ingersent, and J. L. Smith, Nature **413**, 804 EP (2001).

[39] P. G. Niklowitz *et al.*, arXiv (2017).

[40] M. Springford, *Electron: a centenary volume* (Cambridge University Press, 1997).

[41] Y. Takahashi, *Spin Fluctuation Theory of Itinerant Electon Magnetism*, Springer Tracts in Moder Physics Vol. 253 (Springer Heidelberg New Your Dordrecht London, 2013).

[42] D. L. Anderson, *Theory of the Earth* (Blackwell Scientific Publications, 1989).

[43] F. D. Murnaghan, American Journal of Mathematics **59**, 235 (1937).

[44] R. J. Angel*High-pressure structural phase transitions.* Vol. 39 (Reviews in Mineralogy and Geophysics, 2000).

[45] F. D. Murnaghan, Proceedings of the National Academy of Sciences **30**, 244 (1944).

[46] N. Vocadlo and G. D. Price, Physics of the Earth and Planetary Interiors **82**, 261 (1994).

[47] P. W. Bridgman, *The Physics of High Pressure* (G. Bell & Sons, 1958).

[48] J. C. Jamieson, A. W. Lawson, and N. D. Nachtrieb, Review of Scientific Instruments **30**, 1016 (1959).

[49] C. Weir, E. Lippincott, A. Van Valkenburg, and E. Bunting, J. Res. Natl. Bur. Stand. A **63**, 55 (1959).

[50] H. Pierson, *Handbook of Carbon, Graphite, Diamond and Fullerenes* (William Andrew, 1994).

[51] D. J. Dunstan and I. L. Spain, Journal of Physics E: Scientific Instruments **22**, 913 (1989).

[52] R. J. Hemley *et al.*, Phys. Rev. B **39**, 11820 (1989).

[53] G. J. Piermarini, S. Block, J. D. Barnett, and R. A. Forman, Journal of Applied Physics **46**, 2774 (1975).

[54] H. K. Mao, P. M. Bell, J. W. Shaner, and D. J. Steinberg, Journal of Geophysical Research **91**, 673 (1986).

[55] A. D. Chijioke, W. J. Nellis, A. Soldatov, and I. F. Silvera, Journal of Applied Physics **98**, 114905 (2005).

[56] E. Soignard and P. F. McMillan, *An Introduction to Diamond Anvil Cells and Loading Techniques* (Springer Netherlands, Dordrecht, 2004).

[57] Almax easylab, `http://www.almax-easylab.com/index.aspx`, 2017.

[58] H. Wilhelm, The diamond light source - i15, `http://www.diamond.ac.uk/Beamlines/Engineering-and-Environment/I15-Extreme.html`, 2017.

[59] J. L. D. F.R.S., Philosophical Magazine **44**, 503 (1897).

[60] H. E. Winick, Proceedings of the Particle Accelerator Conference (1997).

[61] Schematic of diamond light source, `http://www.lightsources.org`, 2017.

[62] C. Klein, *mar345s Image Plate Detector System: Owner's Guide V1.0* (marXperts GmbH, 2016).

[63] Optoelectronics, *XRD 1621 AN/CN Reference Manual* (Optoelectronics).

[64] G. C. Tyrrell, Nuclear Instruments and Methods in Physics Research Section A: Accelerators, Spectrometers, Detectors and Associated Equipment **546**, 180 (2005), Proceedings of the 6th International Workshop on Radiation Imaging Detectors.

[65] National institute of standards and technology, `https://www.nist.gov/calibrations`, 2017.

[66] A. P. Hammersley, S. O. Svensson, M. Hanfland, A. N. Fitch, and D. Hausermann, High Pressure Research **14**, 235 (1996).

[67] M. Basham *et al.*, Journal of Synchrotron Radiation **22**, 853 (2015).

[68] H. Nowell, S. A. Barnett, K. E. Christensen, S. J. Teat, and D. R. Allan, Journal of Synchrotron Radiation **19**, 435 (2012).

[69] Rigaku, Crysalis$^{Pro}$ website, 24th Jan 2017.

[70] P. Václav, D. Michal, and P. Lukáš, **229**, 345 (2014).

[71] A. A. Coelho, *TOPAS-Academic, Version 6* (, 2016).

[72] T. Ida, M. Ando, and H. Toraya, Journal of Applied Crystallography **33**, 1311 (2000).

[73] P. Vandenabeele, *Practical Raman Spectroscopy: An Introduction* (John Wiley & Sons, 2013).

[74] G. Cinque, The diamond light source - b22, http://www.diamond.ac.uk/Beamlines/Soft-Condensed-Matter/B22.html, 2017.

[75] G. Shirane, S. M. Shapiro, and J. M. Tranquada, *Neutron Scattering with a Triple-Axis Spectrometer* (Cambridge University Press, 2002).

[76] Forschungs-neutronenquelle heinz maier-leibnitz (frmii), https://www.frm2.tum.de/en/home/, 2017.

[77] The reactor orphee, http://www-llb.cea.fr/en/Web/hpr_web/HPRWEB1.php, 2017.

[78] D. Petitgrand, *Experimental Facilities - LLB* (, 2003).

[79] W. J. Duncan *et al.*, physica status solidi (b) **247**, 544 (2010).

[80] M. Brando *et al.*, Phys. Rev. Lett. **101**, 026401 (2008).

[81] S. S. Saxena *et al.*, Nature **406**, 587 EP (2000).

[82] P. L. Alireza *et al.*, Journal of Physics: Condensed Matter **22**, 052202 (2010).

[83] C. Pfleiderer, Rev. Mod. Phys. **81**, 1551 (2009).

[84] A. V. Chubukov, C. Pépin, and J. Rech, Phys. Rev. Lett. **92**, 147003 (2004).

[85] A. G. Green, G. Conduit, and F. Krüger, Annual Review of Condensed Matter Physics **9**, 59 (2018).

[86] G. Abdul-Jabbar *et al.*, Nature Physics **11**, 321 EP (2015).

[87] C. Lester *et al.*, Nature Materials **14**, 373 EP (2015).

[88] D. A. Tompsett, R. J. Needs, F. M. Grosche, and G. G. Lonzarich, Phys. Rev. B **82**, 155137 (2010).

[89] A. Subedi and D. J. Singh, Phys. Rev. B **81**, 024422 (2010).

[90] N. Takayama and M. Shimizu, Journal of Physics F: Metal Physics **18**, L83 (1988).

[91] D. Moroni-Klementowicz *et al.*, Phys. Rev. B **79**, 224410 (2009).

[92] M. Shiga and Y. Nakamura, Journal of the Physical Society of Japan **56**, 4040 (1987).

[93] Y. Yamada and A. Sakata, Journal of the Physical Society of Japan **57**, 46 (1988).

[94] W. J. Duncan *et al.*, physica status solidi (b) **247**, 544 (2009).

[95] W. J. Duncan, *Quantum Phase Transitions in* $NbFe_2$ *and* $BaFe_2As_2$, PhD thesis, Royal Holloway University of London, 2010.

[96] D. Rauch *et al.*, Phys. Rev. B **91**, 174404 (2015).

[97] M. Brando, D. Moroni-Klementowicz, C. Albrecht, and F. Grosche, Physica B **378-380**, 111 (2006).

[98] C. Pfleiderer *et al.*, Journal of Low Temperature Physics **161**, 167 (2010).

[99] S. Friedemann *et al.*, Nat Phys **advance online publication**, (2017).

[100] T. Adams *et al.*, Phys. Rev. Lett. **108**, 237204 (2012).

[101] W. Eerenstein, N. D. Mathur, and J. F. Scott, Nature **442**, 759 EP (2006).

[102] S.-W. Cheong and M. Mostovoy, Nature Materials **6**, 13 EP (2007).

[103] S. Seki, X. Z. Yu, S. Ishiwata, and Y. Tokura, Science **336**, 198 (2012).

[104] G. Meunier and M. Bertaud, Journal of Applied Crystallography **9**, 364 (1976).

[105] M. Belesi *et al.*, Physical Review B - Condensed Matter and Materials Physics **82**, 1 (2010), 1008.2010.

[106] J.-W. G. Bos, C. V. Colin, and T. T. M. Palstra, Phys. Rev. B **78**, 094416 (2008).

[107] H. Effenberger and F. Pertlik, Monatshefte für Chemie / Chemical Monthly **117**, 887 (1986).

[108] O. Janson *et al.*, Nature Communications **5**, 5376 (2014), 1403.2921.

[109] S. A. Hayward, S. A. T. Redfern, and E. K. H. Salje, Journal of Physics: Condensed Matter **14**, 10131 (2002).

[110] I. D. Brown and D. Altermatt, Acta Crystallographica Section B **41**, 244 (1985).

[111] V. P. Gnezdilov *et al.*, Low Temperature Physics **36**, 550 (2010).

[112] K. H. Miller *et al.*, Phys. Rev. B **82**, 144107 (2010).

[113] D. M. Evans, J. A. Schiemer, M. Schmidt, H. Wilhelm, and M. A. Carpenter, Phys. Rev. B **95**, 094426 (2017).

[114] J. H. Yang *et al.*, Phys. Rev. Lett. **109**, 107203 (2012).